Laser Structuring of Organic Optoelectronic Devices

To obtain the academic degree of

Doctor Engineer (Dr.-Ing.)

From the Department of

Electrical Engineering and Information Technology

Karlsruhe Institute of Technology (KIT)

approved

Dissertation

from

M.Sc. Joshua Alejandro Fragoso García

Born in Mexico City, Mexico

First Referee:	Priv.-Doz. Dr.-Ing. Alexander Colsmann
Second Referee:	Prof. Dr. Bernhard Holzapfel
Date of the oral exam:	14.02.2018

Laser Structuring of Organic Optoelectronic Devices

Zur Erlangung des akademischen Grades

DOKTOR-INGENIEURS

Von der Fakultät für Elektrotechnik und Informationstechnik

des Karlsruher Instituts für Technologie (KIT)

genehmigte **Dissertation**

von

M.Sc. Joshua Alejandro Fragoso García

geb. in Mexiko Stadt, Mexiko

Hauptreferent:	Priv.-Doz. Dr.-Ing. Alexander Colsmann
Korreferent:	Prof. Dr. Bernhard Holzapfel
Tag der mündlichen Prüfung:	14.02.2018

Eidesstattliche Erklärung

Die vorliegende Arbeit wurde in der Zeit vom 01. Oktober 2013 bis zum 14. Februar 2018 am Lichttechnischen Institut (LTI) des Karlsruher Instituts für Technologie (KIT) durchgeführt unter der Leitung von Herrn Priv.-Doz. Dr. Alexander Colsmann, LTI, KIT.

Ich versichere hiermit, dass ich die vorliegende Arbeit selbständig und unter Beachtung der Regeln zur Sicherung guter wissenschaftlicher Praxis im Karlsruher Institut für Technologie (KIT) in der aktuellen Fassung angefertigt habe. Ich habe keine anderen als die angegebenen Quellen und Hilfsmittel benutzt und wörtlich oder inhaltlich übernommene Stellen als solche kenntlich gemacht.

Karlsruhe, 15. 01. 2018

(Joshua A. Fragoso García)

Publication List

Articles in peer reviewed journals

J. Fragoso, S.Höfle, M. Zhang, J. Dlugosch, T. Friedrich, S. Wager and A. Colsmann. OLED Luminaires: device arrays with 99.6% geometric fill factor structured by femtosecond laser ablation, *ACS Applied Materials & Interfaces*. doi: 10.1021/acsami.7b12356

Articles in preparation

J. Fragoso, J. Dlugosch and A. Colsmann. Femtosecond multiwavelength ablation ITO on PET, *Organic Electronics*, in preparation

Glaser & **J. Fragoso**, D. Bahro and A. Colsmann. A simple and fast experimental method to find optimum design parameters for organic solar modules, *Solar Energy Materials and Solar Cells*, in preparation

J. Fragoso, T. Friedrich, D. Landerer, M. Koppitz and A. Colsmann. Invisible monolithic connections in semitransparent all-solution organic solar modules, *Energy Technology*, in preparation

Presentations at international conferences

J. Fragoso, T. Friedrich, F. Nickel, D. Bahro, K. Glaser, J. Czolk, D. Landerer, M. Koppitz and A. Colsmann. Selective structuring of multilayers systems for organic solar cells, *International Symposium on flexible Organic Electronics*, Thessaloniki, Greece, 2016

J. Fragoso, K. Glaser, J. Czolk, D. Landerer and A. Colsmann. Selective structuring of polymer multi-layers by femtosecond laser ablation, *International laser & Coating Symposium*, Dresden, Germany, 2015

J. Fragoso, D. Bahro, K. Glaser, F. Nickel and A. Colsmann. Laser structuring of tandem OPV modules, *MatHero Summer School on Organic Photovoltaics*, Freudenstadt, Germany, 2015

Posters at international conferences

J. Fragoso, F. Nickel and A. Colsmann. Femtosecond laser structuring of electrodes for organic solar cells, *MatHero Summer School on Organic Photovoltaics*, Freudenstadt, Germany, 2015

J. Fragoso, F. Nickel and A. Colsmann. Femtosecond laser structuring of electrodes for organic solar cells, *Large-area, Organic and Printed Electronics Convention (LOPEC)*, Munich, Germany, 2014

J.Fragoso, F. Nickel and A. Colsmann. Femtosecond laser structuring of metal electrodes for organic solar cells, *2nd International Next Generation Solar Energy (NGSE)*, Erlangen, Germany, 2013

Supervised student works

M. Mertens. *Laserinduzierte Herstellung von Nickeloxidschichten aus einem flüssigprozessierten Präkursor*, Master Thesis, Fakultät für Elektrotechnik und Informationstechnik, 2018 (in preparation)

F. Haberstroh. *Near-Infrared Femtosecond Laser Ablation of Thin-Films for Organic Photovoltaic Devices*, Master Thesis, Karlsruhe School of Optics and Photonics, 2018

J. Dlugosch. *Laser processing of Nickel Oxide Precursor Films for Organic Photovoltaics*, Master Thesis, Karlsruhe School of Optics and Photonics, 2017

T. Friedrich. *Selektive Laserstrukturierung von Polymerschichten für die organische Photovoltaik*, Masterarbeit, Fakultät für Elektrotechnik und Informationstechnik, 2016

P. Böhler. *Solution processed Nickel Oxide Hole Transport Layers for Organic Solar Cells*, Bachelor Thesis, Department of Physics, Laboratory of Electron Microscopy, 2016

T. Wünnemann *Selektive Laserstrukturierung von organische Photovoltaik*, Master Thesis

Summary

The future promise of organic electronics for a cheap production from solution has led to large investments in research and development. To take the research devices from lab scale to the market, the structuring of them is necessary to connect the devices monolithically to decrease the resistance losses on the devices. Ultrashort pulsed lasers have been used for this purpose in organic photovoltaic. They have also been used to structure the indium tin oxide (ITO) layer in different geometries for its application in other type of devices like organic light emitting diodes (OLEDs).

In this work the use of ultrashort pulsed lasers is investigated. Initially, the structuring of ITO on a mechanically flexible polyethylene substrate is studied. The ablation with different wavelengths is explored. The ablation was then optimized to structure lines with low bulges and selective ablation with negligible damage to the PET layer below. The structured lines were optimized with different wavelengths in the visible regime.

The ablation to monolithically connect OLEDs is then investigated. Devices with small inactive areas that can be concealed by the illumination were manufactured. The power and current efficiencies of these devices were improved by the decrease of the current and power losses on the devices. The structuring was optimized with two different wavelengths.

In the next chapter, the structuring of OPV modules on ITO/glass substrates is explored. Different materials forming the active layer are investigated, demonstrating the feasibility of using the ultrashort pulsed lasers to structure modules with different active layers. The structuring of tandem devices was also explored successfully fabricating working solar modules. Finally, a method to experimentally optimized the solar cell width was investigated.

In the last two chapter two different all-solution OPV architectures (semitransparent and opaque) are explored. The structuring was explored for different wavelengths in the visible regime. Solar modules were then successfully manufactured. In both cases the structuring of the bottom electrode (PEDOT:PSS or silver) is essential as high bulges might lead to shortened devices.

All the processes investigated in this work are an important step for the future fabrication of OPV and OLEDs.

Contents

1 Introduction

Organic Electronics is one of the most promising industrial sectors. It provides an alternative to the mainstream silicon technologies and have several intrinsic advantages, such as thin-film devices, light weight, mechanical flexibility and the possibility of being produced at low cost in roll-to-roll processes. Among the different technologies developed in the organic electronics spectrum we can find organic light emitting devices (OLEDs) for both lighting and display applications, organic photovoltaic devices (OPV), printed devices like temperature and humidity sensors, batteries or memories. All these products have several applications for numerous industries like packaging (sensors), automotive (lighting and energy production), building and architecture (lighting and energy production) among others. Together these applications represent a future market worth in excess of $ 70 billion by 2027, with a large part of it being OLED displays.[1]

OLEDs are the most established technology within the context of organic electronics. The first product to use an active-matrix OLED (AMOLED) was introduced by Kodak and Sanyo in 2003 (Figure 1.1).[2] Currently, AMOLEDs are used in displays in a whole variety of products, like flat screen TVs, mobile phones, tablets etc. OLED lighting applications are already being tested. Audi's swarm tail lights is one example of the use of OLEDs for lighting.[3] The OLED backlighting technology used by AUDI resembles a screen, showing the

Figure 1.1: Camera by Kodak-Sanyo. First device with an OLED display introduced in 2003.[2]

Figure 1.2: OPV integrated into sun glasses. The OPV device supplies energy for thermal and radiation intensity sensors.[6]

actions of the car´s driver. OLEDs have the advantage that they can also be processed from solution through roll-to-roll processes, avoiding costly high vacuum evaporation. However, this needs further exploration as the efficiency of the solution processed devices is not as high as the vacuum processed OLEDs.

OPV are a promising energy technology that open new paths for novel applications. Its intrinsic characteristics like light weight, semitransparency, color tunability, mechanical flexibility, roll-to-roll compatibility and low-light generation offer several advantages over the mainstream silicon technology. Among all of these the most important one may be the low-light generation that enables indoor usage. The internet of things has led to an increasing amount of devices connected to the internet; not only mobile phones or tablets, also smart led bulbs, cameras, sensors, etc. It is estimated that by 2020 there will be more than 50 billion devices connected to the internet, more than 6 per person.[4] All of these devices will increase power consumption as they are supposed to be reachable at all times, therefore operating for long periods of time on standby. The electricity demand of these devices is expected to grow up to 1,140 TWh by 2025, accounting for 6% of the global electricity consumption.[5] Just recently OPV have been integrated into sun glasses.[6] (Figure 1.2) The glasses have an output of 400 µW, supplying energy, without batteries, for one temperature and irradiation sensors. The sensors work even under indoor lighting conditions, demonstrating a power conversion efficiency of 6.2% at 500 lux.

A not so mentioned advantage that OPV have over common crystalline silicon technologies is the lower temperature coefficient. The temperature coefficient quantifies the temperature sensitivity of the photovoltaic device.[7] Common silicon solar modules have an average temperature coefficient between -0.37% and -0.52% C[8]. Therefore, when installed in hot weathers, where the solar resource is plenty, the performance is strongly hampered by the temperature. OPV do not have this disadvantage as the temperature coefficient is slightly positive 0.007% C.[9] This improves the performance of the amount of kWh/kWp produced by OPV in hot temperature places where high irradiance is present.

Both OPV and OLED technologies help mitigate one of the largest problems humanity is facing, Global Warming. As described above, the internet of things will require a total of 1,140 TWh. These whole electricity consumption will generate more than 600 Mtons of CO_2 to the atmosphere. This is a low estimate as a CO_2 emission factor of 560 g kWh^{-1} is considered. This is the emission factor reported for Germany over 2016.[10] The capabilities of OPV will expand the reach of renewable energies to produce energy inside our own houses. OLEDs are one highly energy efficient light source, hence the replacement of current luminaries with OLED luminaires will help to decrease the necessary electricity used in houses.

OPV and OLED technologies require high precision structuring steps that allow the right application of the technology. Ultrashort pulsed lasers are a unique tool that allows for high precision and selective structuring of the thin film layers. Due to the cold ablation characteristics, the heat affected zone is minimized further increasing the precision. Currently, devices with a repetition rate of 200 kHz with a pulse energy of 1 mW are available in the market.[11] The high repetition rate allows the integration of the laser into a roll-to-roll device without a significant decrease in the coating speed.

In this work, a femtosecond laser source is used to selectively structure different organic electronic devices (OLEDs and OPV).

2 Fundamentals of organic semiconductors

This chapter covers the fundamental knowledge necessary to understand the function of OPV and OLEDs. Organic electronics exhibit semiconductor properties that enable the construction of devices that are analogous to the ones used with inorganic semiconductors. Important differences are present as the organic semiconductors do not have a valence band and conduction band, instead they have a highest occupied orbital (HOMO) and lowest unoccupied orbital (LUMO). Due to the solution formation of some or all the layers, the upscaling of organic electronics is different to the one of inorganic semiconductors. In section 2.1 the working principles of organic semiconductors is explained. Section 2.2 covers the working principle of OPV, its characterization and the upscaling processes. Similarly, section 2.3 describes the working principle of an OLED, its characterization and the upscaling processes.

2.1 Organic semiconductors

Organic semiconductors are carbon based materials that exhibit semiconducting properties. Carbon is a chemical element with symbol C and atomic number 6. It has four valence electrons in its ground state. The electron distribution of carbon in its ground state is the following: two electrons in the 1s orbital, two in the 2s orbital and the remaining two in two of the three 2p orbitals. The ground state electronic configuration can be written as $1s^2 2s^2 2p_x^1 2p_y^1$. The s orbitals are associated with a spherical charge distribution (Figure 2.1a) around the center of the atom, while the p orbitals have an 8 figure distribution (Figure 2.1b). In the proximity of other carbon or hydrogen atoms that act as binding partners, the exerted external forces compensate the energy difference between the 2s and the 2p orbitals.

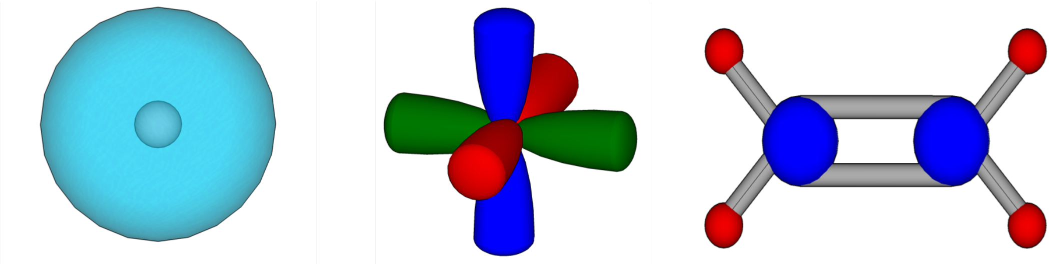
(a) (b) (c)

Figure 2.1: (a) s orbitals in the carbon atom. (b) p orbitals in the carbon atom. (c) Ethene molecule with the sp orbitals forming σ bonds and the p orbitals forming π bonds.

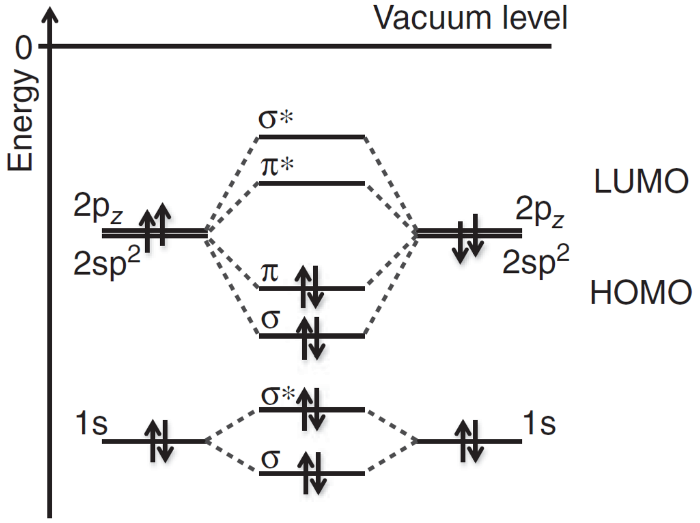

Figure 2.2: Energy level diagram for the molecule ethene. It shows the formation of π and σ bonds from atomic orbitals. The two $2sp^2$ orbitals are not depicted.[12]

This results in the formation of mixed orbitals known as *hybrid orbitals*. The mixing may occur between one s and one, two or all three p orbitals. When the 2s orbital mixes with two 2p orbitals, three sp^2 orbitals are created. The three orbitals are distributed in the same plane. The remaining 2p orbital is normal to that plane as in the ethene molecule (Figure 2.1c). If the spatial probability goes around the axis joining the two atoms it is called σ orbital. When the electron´s spacial probability is above and below the line connecting the two atoms it is known as π orbital.

The π and σ orbitals play an important role in organic semiconductors. The ethene molecule is a good example of this. The interaction occurs among the two 1s orbitals, two $2sp^2$ hybrid orbitals and two 2p orbitals from the carbon atoms. The 1s orbitals form a σ and a σ^* with little splitting between them as there is negligible resonance interaction. One of the three $2sp^2$ orbitals connects the carbon atoms, therefore there is a large resonance between σ and the σ^* orbitals separating them far apart. Similarly the $2sp^2$ orbitals between the carbon and the hydrogen led to large separation between the orbitals. A different case occurs with the π orbitals formed by the 2p orbitals. Due to its separation from the nuclei, the distance between the π and π^* is not as large as between the σ orbitals (Figure 2.2).

Figure 2.2 depicts the electron distribution in the ethene molecule. Each 1s orbital has two electrons, that will accommodate in both σ and a σ^* orbitals. The three $2sp^2$ hybrid orbitals contain three single electrons. These electrons combined with the electron from the other carbon $2sp^2$ or the hydrogen´s 1s orbital will fill the σ orbital leaving the σ^* empty. The two carbon 2p orbitals have one electron to be allocated. These are allocated in the π orbitals leaving the π^* empty. The gap between the orbital energy levels of the π and π^* is smaller than the gap of the σ and σ^*. This results in a lower energy requirement to excite the electrons from the π to the π^* than the energy requirement to excite electrons in the σ and σ^* levels. The highest occupied molecular orbital (HOMO) is a π orbital and the lowest unoccupied molecular orbital (LUMO) is a π^* orbital for the ethene molecule. The HOMO

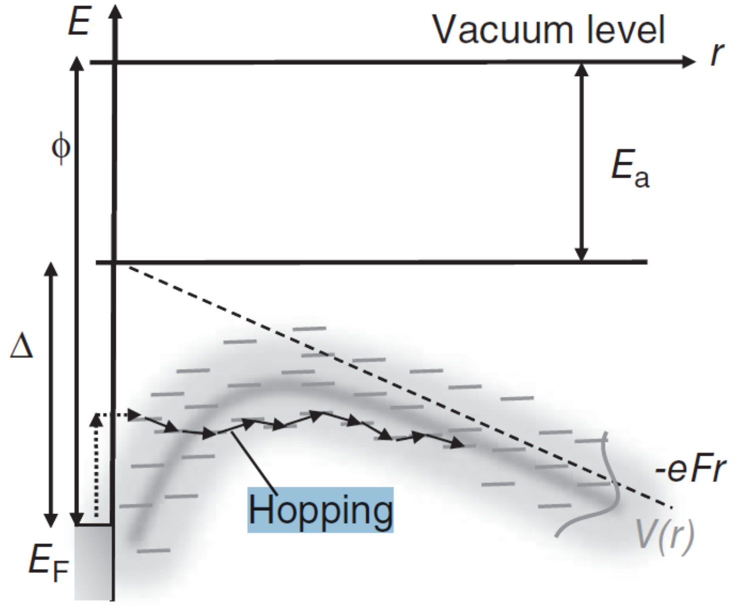

Figure 2.3: Hopping process in a disordered organic solid. r depicts the distance from the electrode. The dashed line indicates the potential energy due to the electric field F.[12]

and the LUMO are called frontier orbitals. The energy difference between the HOMO and the LUMO is analogous to the energy difference between the valence band and conduction band in the inorganic semiconductors and is responsible for the semiconductor properties of organic materials.

In order to use the semiconducting properties of organic materials, the charge carriers (holes and electrons) need to be extracted/injected. Due to the high and low energy levels of the σ and σ^* it is difficult to achieve charge injection from the electrodes into these levels in the molecule. On the contrary, the π and π^* have moderate energy levels that facilitate charge injection.

Different to inorganic semiconductors, the orbitals do not form a regular uniform energy band, it is rather a collection of states where the charges move. Therefore, a so called hopping process is the way the charge carriers propagate inside the organic semiconductor (Figure 2.3). This is one of the reasons why organic semiconductors have lower mobilities, in the range of 10^{-5} - 10^{-2} $cm^2\,V^{-1}\,s^{-1}$, than inorganic semiconductors with mobilities in the range of 10^3 - 10^4 $cm^2\,V^{-1}\,s^{-1}$.

2.2 Organic photovoltaics

2.2.1 Working principle

Organic solar cells have attracted large interest since they were discovered by Tang in 1986, who developed single heterojunction devices with an efficiency of about 1%.[13] There are substantial differences between the common pn-junction solar cells made from crystalline silicon and the ones made from organic semiconductors.[14][15]

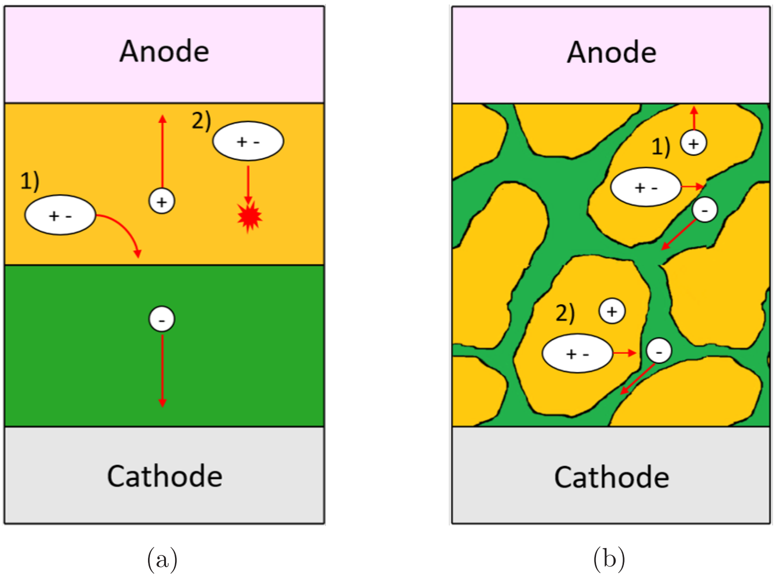

Figure 2.4: (a) Bilayer heterojunction solar cell. 1) Light is absorbed close to the interface generating an exciton. The exciton is dissociated at the interface. The electron and hole are collected in the cathode and anode respectively. 2) The light is absorbed far from the interface generating an exciton that recombines afterward. (b) Bulk-heterojunction solar cell. The donor and acceptor domains are intermixed increasing the interface surface area. 1) The light is absorbed producing an exciton that is dissociated at the interface. The electron and hole are collected in the cathode and anode respectively. 2) The light is absorbed producing an exciton that is dissociated. The hole is trapped as it is located on an island with no contact to the anode. The hole will recombine afterwards.

- The absorption of a photon in an organic solar cell produces an excited state called exciton (bound electron-hole pair). This exciton has a high binding energy of at least 300 meV whereas excitons in inorganic semiconductors exhibit binding energies of a only a few meV. To generate a current the excitons need to be dissociated. A second material, commonly called acceptor, is necessary for this dissociation. This material will provide an energy difference that is enough to separate the exciton.

- The diffusion length of the exciton is between 10 - 20 nm. If an exciton does not reach the acceptor/donor interface, it would recombine and the energy would be lost as heat.

- Organic semiconductors have large extinction coefficients compared to crystalline silicon. This leads to an efficient light harvesting in thin-films of 100 - 300 nm thickness.

- Organic solar cells are sandwiched between two electrodes with different work functions. A built-in potential appears, resulting in an electric field that helps the transport of charges. An organic solar cell is a drift device, whereas crystalline silicon solar cells depends mainly on diffusion processes.

An organic solar cell with an architecture similar to the one used by Tang is depicted in Figure 2.4a. The charges are usually absorbed on the donor material (Yellow). An exciton is created and it moves to the interfaces where it is dissociated (1). The hole is then collected at the anode and the electrode at the cathode. If the exciton does not reach the interface, it recombines (2). This type of architecture does not achieve high efficiencies. The

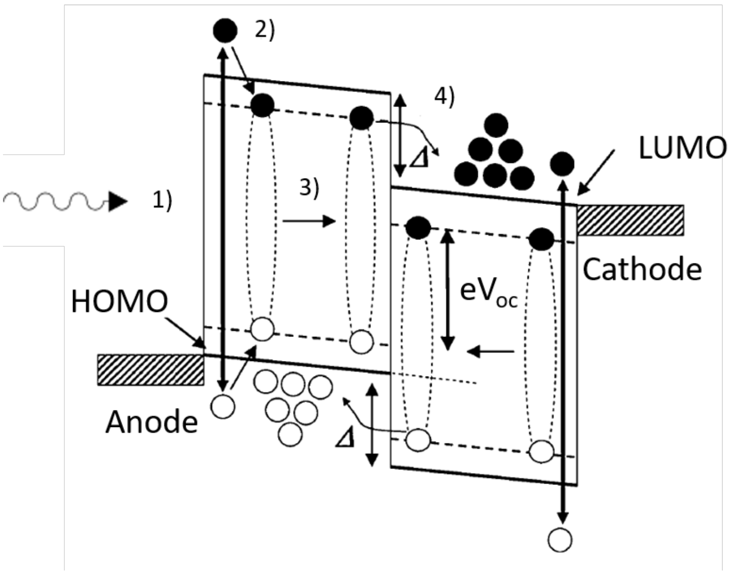

Figure 2.5: Energy levels of an organic solar cell. 1) Photons with higher energy than the bandgap are absorbed. 2) Thermalization occurs and the exciton is formed. 3) Exciton diffusion to the material interface where it is dissociated. 4) Electron or holes are transferred to the acceptor or donor respectively. The open circuit voltage is also indicated.[14]

layer thickness need to be ultrathin, approximately 20 nm to achieve appropriate exciton dissociation due to the limited exciton diffusion length. Even with the large extinction coefficients of organic solar cells, this thickness will not be sufficient to absorb a significant amount of light. A solution to increase the interface, while keeping the distance the exciton needs to travel within the exciton diffusion length, is a bulk heterojunction (BHJ) (Figure 2.4b). The materials are mixed together creating a morphology that allows to increase the interface between the donor and acceptor. Similar to the bilayer-heterojunction, the light is absorbed in the donor. The created exciton travels to the interface and the charges are collected in the electrodes (1). However, some of the free charge carriers may not be able to reach their respective electrode as they are located in an island with no contact to the electrode. The charge carriers then recombine leading to higher losses on the device. Therefore, optimization of the BHJ morphology is necessary to decrease the recombination losses.

Figure 2.5 shows the energy level diagrams of an organic solar cell.[14] Photons with higher energy than the bandgap are absorbed (1). The absorption may occur on both sides of the interface. If the photon energy is higher than the bandgap, thermalization occurs and an exciton is formed (2). The exciton diffuses to the interface where it dissociates (3). The electrons are then transported to the cathode and the holes to the anode (4).

One of the most important parameters for solar cells, the open-circuit voltage (V_{oc}), is depicted in Figure 2.5 for organic solar cells. The V_{oc} is proportional to the energy gap between the HOMO level of the donor and the LUMO level of the acceptor. The V_{oc} can be calculated using the following empirical formula[16]:

$$V_{\mathrm{oc}} = \frac{1}{e}(|E_{\mathrm{HOMO,donor}}| - |E_{\mathrm{LUMO,acceptor}}|) - 0.3\,V \tag{2.1}$$

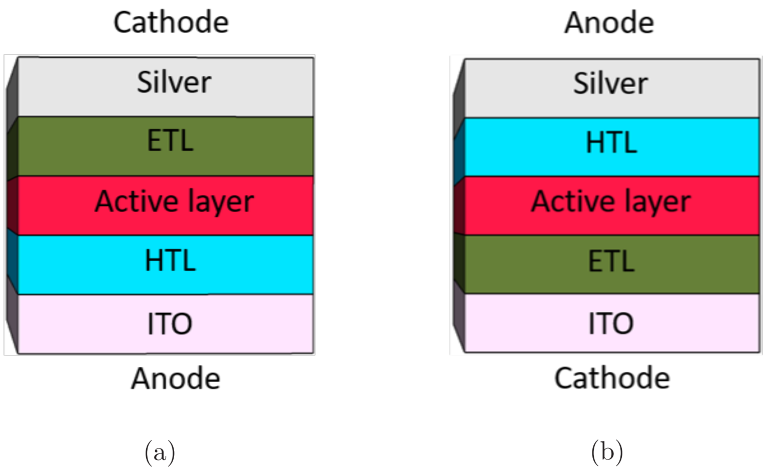

(a) (b)

Figure 2.6: Regular and inverted architectures with ITO and silver as top and bottom electrode. (a) Organic solar cell with regular architecture: the position of the hole transport layer (HTL) on top of the ITO defines it as the anode. (b) Organic solar cell with inverted architecture organic: the position of the electron transport layer (ETL) on top of the ITO defines it as the cathode.

Where V_{oc} is the open-circuit voltage, e is the elementary charge, $E_{\text{HOMO,donor}}$ is the HOMO level of the donor and $E_{\text{LUMO,acceptor}}$ is the LUMO level of the acceptor in eV. The 0.3 V is the empirically calculated necessary energy to dissociate the electron.[17]

2.2.2 Interface materials in organic solar cells

Interface materials have proved to help increasing the performance of organic solar cells. The functions of interface materials are:[18 19]

- Determines the device polarity. Regular and inverted architectures are used in organic solar cells (Figure 2.6). Indium tin oxide (ITO) is commonly used as the bottom transparent electrode while silver or aluminum are commonly used as the top electrode. Figure 2.6a shows the hole transport layer (HTL) on top of the ITO defining it as the anode for the regular architecture. On the contrary, figure 2.6b shows the electron transport layer on top of the ITO defining it as the cathode for the inverted architecture.

- The interface materials should provide an ohmic electrode with the organic material. An ohmic electrode is capable to inject/extract more charges than can be transported/produced in the device. This condition is defined as sustained space charge limited current (SCL). Whether an electrode is able to sustain SCL conditions depends both on the extraction barrier and the charge carrier mobility of the organic semiconductor. For ideal interfaces, the extraction barrier is defined by the energy difference between the work function of the electrodes and the HOMO of the donor and the LUMO of the acceptor (Figure 2.7). An estimate of an acceptable barrier is 0.3 eV for a conjugated polymer with an average mobility of $10^{-4}\,\text{cm}^2\,\text{V}^{-1}\,\text{s}^{-1}$.[12]

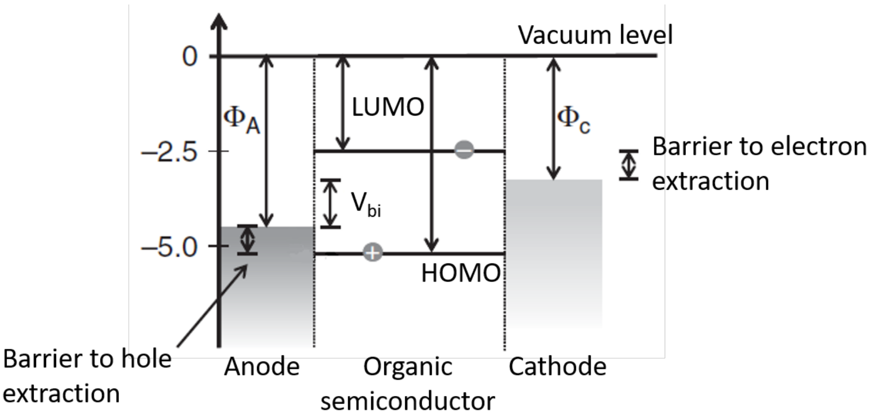

Figure 2.7: Energy level alignment in an organic solar cell. The electrodes work functions are denoted as Φ_A and Φ_C. The energy barriers between the HOMO and LUMO and the work functions are depicted. To guarantee an Ohmic contact the energy barrier should be as small as possible.[12]

- Due to the internal reflections in organic solar cells, interference effects play an important role on the performance. The amount of light absorbed in the active layer of an organic solar cell depends on the electrical field strength. The use of a thin-film layer, of some tens of nanometers, may be enough to shift the maximum absorption point to the active layer and therefore to improve the photo current of the device and its performance.

- The materials used in organic solar cells are not physically and chemically stable, especially when exposed to oxygen or water.[20] Similarly, metal atoms from the electrodes may diffuse into the organic materials causing shunting of the organic devices. Interface materials can protect the organic layer against these agents enhancing the device lifetime.

A material commonly used as HTL is the conducting polymer polyethylenedioxythio - phene:polystyrene sulfonate (PEDOT:PSS). This material offers several advantages, it can be easily coated on top of the electrode or the active layer in both regular and inverted architectures. The material can be purchased in different formulations that offer different properties like tunable conductivities in the range of 10^{-6} to 10^{3} S cm^{-1}. PEDOT:PSS is also highly transparent, reducing the optical losses. It has a work function around 5.0 eV that matches well with the HOMO levels of many polymers. However, PEDOT:PSS also has several disadvantages. It is a hygroscopic material that has proven to limit the lifetime of the devices.[21] Similarly, it is highly acidic causing etching problems on the electrodes.[22] The PEDOT:PSS work function, does not match the HOMO levels of some recent developed materials that are designed to provide a high V_{oc} which exhibit a deeper HOMO than the PEDOT:PSS work function.

In a similar fashion, the combination of calcium and aluminum has been used as cathode in organic solar cells. Although calcium offers an appropriate match with the energy levels of the LUMO of common acceptor materials. It is well known to oxidize and therefore decrease the lifetime of organic solar cells.

Metal oxides offer an alternative to both PEDOT:PSS and the combination of calcium/aluminum. Most metal oxides are robust and stable, eliminating the problem of the stability that comes with the use of PEDOT:PSS or calcium. They can be processed from solution using different chemical precursors or can be evaporated in vacuum. There are several metal oxides with different work functions to choose in order to match the energy levels of the semiconducting polymer materials.

2.2.3 Tandem solar cells

Similar to other photovoltaic devices, organic solar cells do not absorb light in the whole solar spectrum. This leads to absorption losses, due to photons that have less energy than the bandgap, and thermalization losses of high energy photons, caused by the electron relaxation after the photon is absorbed. Therefore, an efficient way to absorb light along the whole solar spectrum is necessary.[23]

A promising concept, that has been widely used in other photovoltaic technologies, is to have two serially connected solar cells on top of each other. This is known as tandem or multijunction solar cells (TSC). The absorption materials used in the TSC usually have complimentary absorption spectra, hence absorbing a larger part of the solar spectrum. Due to the thin film nature of organic solar cells there is also a benefit from designing a TSC using twice the same absorption material. This compensates for the low optical density or moderate charge carrier transport properties of the material.[24] The concept of homo-TSC and hetero-TSC is illustrated below (Figure 2.8).

Due to the serial connection of TSC, they exhibit larger voltage and lower currents, resulting in the reduction of of resistive losses in the electrodes. The higher voltage also enables the use of TSC to split water photochemically.[26]

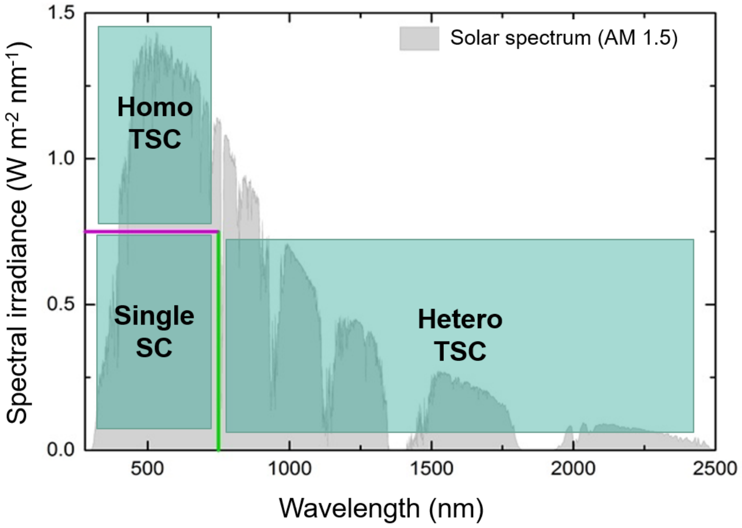

Figure 2.8: Absorption spectrum coverage for homo and hetero tandem solar cells.[25] The single junction solar cell efficiency is limited to the bottom left. The hetero-TSC complements the absorption spectrum of the single solar cell (Right part), while the homo-TSC compensates for low optical density (top part).

Tandem architectures have a theoretical maximum power conversion efficiency (PCE) limit of 15%.[27] TSC with 13.2%[28] have already been built, successfully demonstrating the application of this concept in organic solar cells.

2.2.4 Electrical characterization of organic solar cells

A solar cell can be approximated to a diode in the dark. A diode is a device that allows a much larger current under forward bias (V>0) than under reverse bias (V<0), hence having a rectifying behavior.[29] For an ideal diode the dark current density J_{dark} is given by:

$$J_{\mathrm{dark}}(V) = J_{\mathrm{o}}(e^{\frac{qV}{k_{\mathrm{B}}T}} - 1) \tag{2.2}$$

Where J_{o} is a constant, K_{B} is the Boltzmann constant and T is the temperature in Kelvin. When light shines on the device, a net photocurrent is produced that results from the subtraction of the short circuit current J_{sc} and the dark current, resulting in:

$$J = J_{\mathrm{sc}} - J_{\mathrm{o}}(e^{\frac{qV}{k_{\mathrm{B}}T}} - 1) \tag{2.3}$$

When the contacts are isolated, the potential difference is maximized and the solar cell produces the open circuit voltage (V_{oc}). For the ideal diode this is given by:

$$V_{\mathrm{oc}} = \frac{kT}{q}\ln(\frac{J_{\mathrm{sc}}}{J_{\mathrm{o}}} + 1) \tag{2.4}$$

However, in real solar cells, the power is dissipated through the resistance of the contacts and through leakage currents. These effects can be electrically approximated to a series (R_{s}) and parallel (R_{sh}) resistance. The equivalent electrical circuit showing both R_{s} and R_{sh}, together with the J_{sc} and J_{dark} is shown in figure 2.9.

If the parasitic resistances are considered the equation for the current of a solar cell becomes:

$$J = J_{\mathrm{sc}} - J_{\mathrm{o}}(e^{\frac{q(V+JAR_{\mathrm{S}})}{k_{\mathrm{B}}T}} - 1) - \frac{V + JAR_{\mathrm{S}}}{R_{\mathrm{sh}}} \tag{2.5}$$

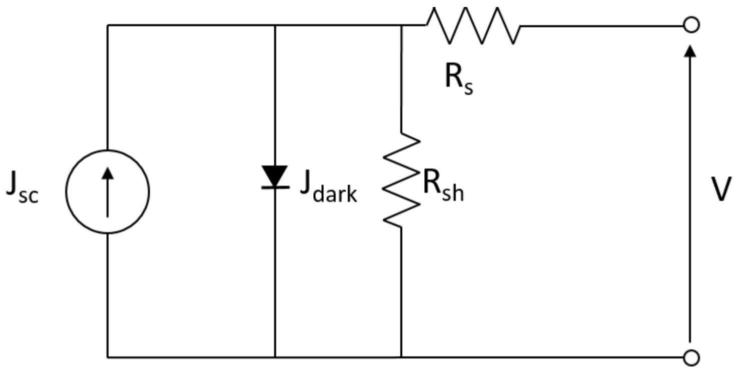

Figure 2.9: Equivalent circuit of a solar cell. The series resistance of the electrodes is depicted as (R_{s}) and the shunt resistance as (R_{sh}).

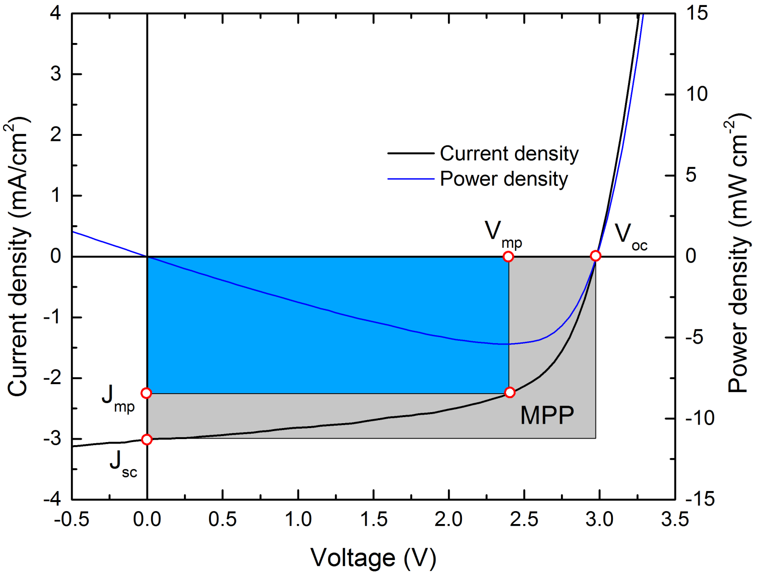

Figure 2.10: Current density (black line) and power density (blue line) of a solar cell. The fill factor is the ratio between the blue and the gray rectangles.

The power provided by a solar cell is $P = JV$. A solar cell has an optimum operating point where it operates with the maximum efficiency. This point is know as the maximum power point (MPP) at the voltage V_{mp} and the current I_{mp}. The ratio between the V_{mp} the current I_{mp} and the V_{oc} and current I_{sc} is defined as fill factor (FF). The FF is then given by:

$$FF = \frac{V_{\text{mp}} J_{\text{mp}}}{V_{\text{oc}} J_{\text{sc}}} \tag{2.6}$$

Figure 2.10 depicts the fill factor as the ratio between the gray rectangle and the blue rectangle. J-V curves are used in this work instead of I-V curves to ease the comparison of different size devices.

The power conversion efficiency (PCE) is the ratio of the extracted power over the incident light (P_{in}):

$$PCE = \frac{V_{\text{mp}} J_{\text{mp}}}{P_{\text{in}}} \tag{2.7}$$

The FF and the power conversion efficiency are then related by:

$$PCE = \frac{J_{\text{sc}} V_{\text{oc}} FF}{P_{\text{in}}} \tag{2.8}$$

These four parameters J_{sc}, V_{oc}, FF and PCE are the key performance parameters. It is important to consider that the PCE is reported using standard test conditions (STC). The STC are defined as $1000\,\mathrm{W\,m^{-2}}$, air mass (AM) of 1.5 and 25°C. The air mass depends on the path length that the light has to travel through the atmosphere to reach the position of the solar cells.

2.2.5 Organic solar modules

Most of the solar cells that are built on laboratory scale are in the square millimeter scale, making the electrical losses due to the resistance of the semi-transparent electrode irrelevant. When an organic solar cell is upscaled, the resistance losses increase as the path that the charges need to travel, is longer. In addition the photocurrent grows with the area, increasing the power losses $P_{\text{loss}} = VI^2$. A common solution is to limit the size of the solar cells, therefore limiting the current and the power losses. The solar cells are then serially connected in a solar module through a monolithic connection (Figure 2.11). The monolithic connection is achieved in three manufacturing steps. The first structuring step (P1) takes place on the bottom electrode, electrically isolating the subsequent solar cells. The second step (P2) divides the photoactive area, allowing the electrical connection between the devices. The third step (P3) separates the top electrode.

It is important to consider that the area between the P1 and P3 cuts is not photoactive and does not produce energy. The ratio between the active area and the total area of device is the geometric fill factor (GFF). Structuring can be accomplished through lithography or mechanical processes. The lithography process has the disadvantage that is not suitable for large scale fabrication while the mechanical processes generate a large inactive area leading to a reduction in the GFF. Reported GFF using mechanical methods are between 50 % and 75 %.[30 31] Hence, it is necessary to find alternative structuring processes to reduce the inactive area. One option is the use of ultrashort pulsed lasers. This concept has been proven before for CIGS[32 33], amorphous silicon[34] and organic solar cells[35 36 37] and it is further discussed in this thesis.

Besides the construction of the monolithic connection, it is necessary to upscale the coating procedures for larger devices. Although the frequently used spin coater produces high quality layers, it has a substrate size limitation and it is not possible to adapt it to a roll-to-roll process. Hence, doctor blading was used in this work due to its similarities to the slot-die coating that can be used on an industrial scale.

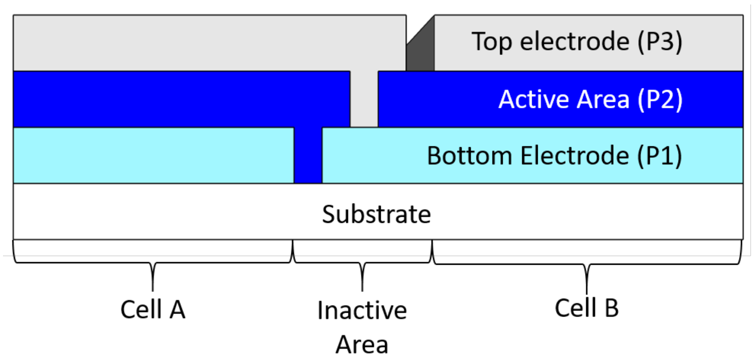

Figure 2.11: Two solar cells connected through a monolithic connection. The monolithic connection is achieved in three different structuring steps. Bottom electrode (P1) to isolate the individual solar cells electrically. Active area (P2) to permit the electrical connection between the electrodes. Top electrode (P3) to isolate the solar cells. The area defined between P1 and P3 is inactive.

2.3 Organic light emitting diodes

2.3.1 Working principle

Organic light emitting diodes (OLEDs) employ the inverse working principle of organic solar cells. A voltage is applied to the device, positive and negative charges are injected through the electrodes. Electrons and holes form excitons, and then they recombine emitting light (Figure 2.12).
One of the first OLEDs was reported by Tang in 1987 with an external quantum efficiency of 1% luminous efficiency of 1.5 lm W^{-1} and brightness larger than 1000 cd m^{-2}. OLEDs have attracted the attention of both research institutes and industry due to its several advantages over liquid crystal displays.

- Faster response.
- Higher image contrast.
- Optional mechanical flexibility.
- Light weight.
- Possibility of roll-to-roll production for future fast and low cost production.

2.3.2 Light emission and the role of the spin

The spin plays an important role in the emission mechanism of OLEDs. The spin of a state is given by the total spin of the electrons in all the orbitals. However, the completely filled orbitals have no contribution to the total spin. Hence, the spin of the molecule can be calculated only considering the unpaired electrons of an excited state. Usually, this means

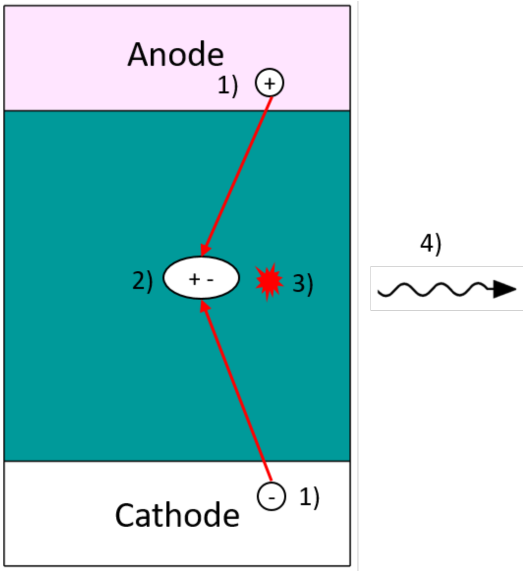

Figure 2.12: OLED working principle. 1) The charges are injected through the electrodes, 2) the charges form an exciton, 3) the exciton recombines and 4) light is emitted.

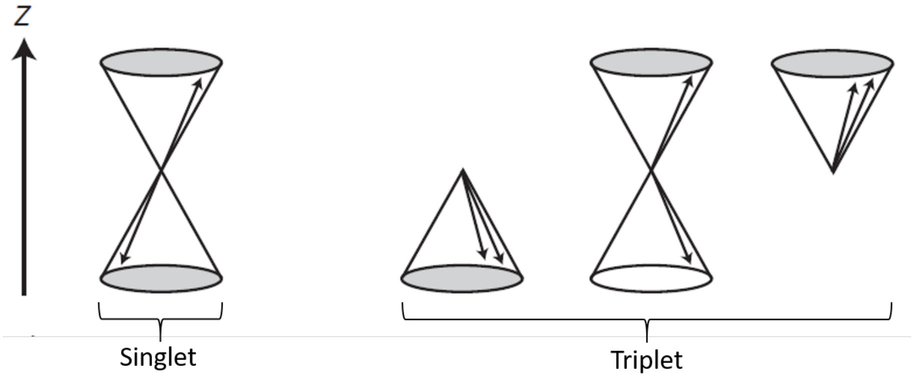

Figure 2.13: Vectorial representation of the four different spin configurations of a two-particle-system (two electrons). The first is the singlet state, while the last three represent the triplet state.[38]

the spin of one electron in the π orbital and the excited electron in the π^* orbital. When the spin of the electrons are antiparallel, the addition to the total spin is zero. When the spin of the electrons are parallel, the addition to the total spin is one. The unpaired electrons in the π and the π^* orbital form a two particle states. The two-particle-system that can be described with the eigenvalues S and M_s. The spin wavefunction (Ψ_spin) of one electron states α and β with eigenvalues $s = 1/2$, $m_\mathrm{s} = 1/2$ and $s =$ -1/2 and $\mathrm{m_s} =$ -1/2 result on four different spin wavefunctions.[38]

$$
\begin{aligned}
\Psi_{\mathrm{spin,T+}} &= \alpha_1\alpha_2 \\
\Psi_{\mathrm{spin,T0}} &= \frac{1}{\sqrt{2}}(\alpha_1\beta_2 + \beta_1\alpha_2) \\
\Psi_{\mathrm{spin,T-}} &= \beta_1\beta_2 \\
\Psi_{\mathrm{spin,S}} &= \frac{1}{\sqrt{2}}(\alpha_1\beta_2 - \beta_1\alpha_2)
\end{aligned}
\tag{2.9}
$$

The indices 1 and 2 on α and β differentiate between the two electrons. The first three functions in equation 2.9 have an eigenvalue $S = 1$ and just differ on the z-component of the spin, that takes the eigenvalues $M_\mathrm{s} = 1$,0,-1. The states where the eigenvalue of $S = 1$ is the triplet due to the three different values of the z-component. The state where $S = 0$ has just one possible value for the $M_\mathrm{s} = 0$ and it is the so called singlet. The vector diagram representation of the singlet and triplet states is shown in figure 2.13.

The radiative decay mechanism of a singlet state is fluorescence, while the radiative mechanism for the triplet states is phosphorescence. Due to the three different possibilities for the triplet states 75% of the electrons are in these states. This limits the efficiency of the OLEDs as the phosphorescence transition is forbidden. Hence, just 25% of the excited electrons in the molecule will contribute to the fluorescence emission.[39] Spin-orbit coupling enables the use of phosphorescence through the use of heavy metals.

2.3.3 OLED characterization

The electromagnetic radiation emitted by an OLED can be characterized in terms of physical quantities (i.e. number of photons, photon energy, optical power commonly known as “radiant flux”). However, these units do not consider the human eye’s perception of light. For example, if an OLED has a high emission of photons in the infrared, the emitted optical energy could be high. This would not matter to the human eyes as they cannot detect light in the infrared regime. Therefore, different units that consider the perception of the human eye are needed. These units are called photometric units.[40]

- The luminous intensity (I_v), represents the intensity of an optical source, as perceived by the human eye. Its units are candela (cd), which is a base unit of the International System of Units. A candela is defined as: *the luminous intensity, in any given direction of a source that emits monochromatic radiation of frequency 540 x 10*^{12} *hertz and that has a radiant intensity in that direction of 1/683 watt steradian*$^{-1}$.[41]

- The luminous flux (Φ), represents the light power of a source as perceived by the human eye. The unit of luminous flux is the lumen (lm) and it is defined as:*the luminous intensity, in any given direction of a source that emits monochromatic radiation of frequency 540 x 10*^{12} *hertz and that has a radiant intensity in that direction of 1/683 watt.* The lumen is an SI unit derived from the candela. One candela is equivalent to one lumen steradian^{-1} or cd = lm sr^{-1}. OLEDs are considered lambertian sources. A lambertian source emits light uniformly in all directions. Hence the luminance of an OLED can be calculated by:

$$L = \frac{\Phi}{A\pi} \tag{2.10}$$

- The illuminance is the luminous flux incident per unit area. The unit of illuminance is the lux = lm m^{-2}. It is used to characterize the necessary illuminance in different environments, i.e. office desk lighting should have a minimum of 500 lux.

- The luminance (L) of a surface source is the ratio of the luminous intensity emitted in a certain direction (measured in cd) and the projected surface area(measured in m^2).

- The current efficiency (η_c) is also an important performance parameter. It is calculated by dividing the luminance (L) by the current density (J).

$$\eta_\mathrm{c} = \frac{L}{J} \tag{2.11}$$

- The power efficiency (η) is given by the ration between the luminous flux and the electrical power (P).

$$\eta = \frac{\Phi}{P} \tag{2.12}$$

2.3.4 Upscaling of OLEDs

Similar to the case of organic solar cells, the resistance of the transparent electrode has a significant impact on the device performance when it is upscaled. In OLEDs it is even more relevant as the high sheet resistance can lead to a voltage loss in the device that is translated into inhomogeneous luminance.[42] This high sheet resistance leads also to lower efficiency as the current necessary to light the devices increases with the area. Initial efforts to integrate highly conductive metal grids or bus bars have been explored to solve this problem.[43–45] Slawinsky et al. tested different grid configurations and increased the homogeneity of a 12 x 12 cm^2 device.[44] However, the bus bars and grids remain visible hence affecting the homogeneity of the device.

Another approach to reduce the current on the device, and consequently the resistive losses, is the use of tandem architectures. The tandem architectures allows the production of more than one photon per electron-hole pair.[46–51] This reduces the current and doubles the voltage, hence reducing the power losses when the device is upscaled.

The concept of monolithic connections (Figure 2.11) has also been explored for OLEDs. The individual OLED size is limited and therefore the current is reduced. As in the case of the tandem option, the driving voltage increases with the number of individual units that are connected. Duggal et al. demonstrated the feasibility of this approach in OLEDs, enhancing the lifetime of the devices as the number of faulty devices decreased.[52] Analogous to the case of organic solar cells, the area between P1 and P3 does not emit light and therefore, should be reduced as much as possible. This concept is further explored in this thesis.

3 Fabrication and characterization

This chapter covers the different coating and characterization techniques used in this work. Section 3.1 describes the preparation process of the samples, from the cleaning of the substrates to the layer application processes. The cleanroom environment where the experiments took place is also described in this section. Section 3.2 describes the different characterization methods used in this work. Finally, section 3.3 describes the laser setup used for the ablation experiments elaborated under the scope of this work.

3.1 Sample preparation

3.1.1 Substrate preparation

Both rigid glass and flexible Polyethylene terephthalate (PET) substrates were used in the scope of this work. Indium tin oxide (ITO) was used as semitransparent electrode in both glass and PET substrates. The ITO was structured by etching for 10 minutes in a bath of hydrochloric acid (37% concentration). The substrates were subsequently cleaned with acetone and isopropanol in an ultrasonic bath (10 min each) and dried using nitrogen. The substrates were then exposed to oxygen plasma for 2 minutes to remove any organic residues.

3.1.2 Layer application from solution

Two main solution coating methods were used to manufacture the devices investigated in this work: spincoating and doctor blading.

- Spincoating is one of the most reliable techniques to apply layers from solution on laboratory scale. It allows the formation of highly reproducible films and it can coat substrates up to 30 cm^2. The typical spincoating process involves the application of a liquid to a substrate followed by acceleration of the substrate to a chosen rotational speed. The process can involve different steps, each with its own speed, time lapse and acceleration. The angular velocity of the substrate results in ejection of most of the solution, leaving just a thin-film on the substrate. The thickness depends on the rotational speed, viscosity, volatility, molecular weight and concentration of the solutions. The film thickness d can be empirically estimated from the relationship.[53]

$$d = k\omega^{\alpha} \tag{3.1}$$

Where ω is the angular velocity and k and α are constants related to the physical properties of the solution. Spincoating has the disadvantage that most of the solution is wasted and it is not compatible to roll-to-roll production as the substrates need to be handled individually. All spincoating was performed in a glovebox under nitrogen atmosphere. The spincoater used for this work was located at the Light Technology Institute (LTI).

- Doctor blading is a coating technique that has the advantage of producing less waste (less than 5%). The technique works by placing a blade at a fixed distance from the substrate surface that has to be coated. Typically, the gap is between 10 and 500 µm. The solution is then deposited in front of the blade (Figure 3.1). The blade is moved at a constant or variable speed pushing the solution over the substrate. The variable speed helps to compensate for the lack of material at the end of the substrate, hence producing more uniform layers. Some doctor blading systems also have a temperature controlled plate that helps to regulate the drying process of the film.[53]

  The final wet thickness should be around half of the blade height. The final dry thickness depends on the concentration of the solution. The speed of the blade also plays an important role. The final dry thickness can be calculated from the the empirical relationship:[55]

  $$d = cv^{\frac{2}{3}} \tag{3.2}$$

  Where c is an empirical factor and v is the speed of the blade. The main advantages of doctor blading over spincoating is that almost no material is lost, reducing the material use. Another advantage is that doctor blading is easily transferable to roll-to-roll process as it is similar to the knife-over-edge coating. It also has similarities to slot-die coating.

  The main drawback of the doctor blading technique is the possible inhomogeneity of the film. This homogeneity is largest in the beginning and in the end. This can be partially compensated with the use of an accelerated process. Another disadvantage

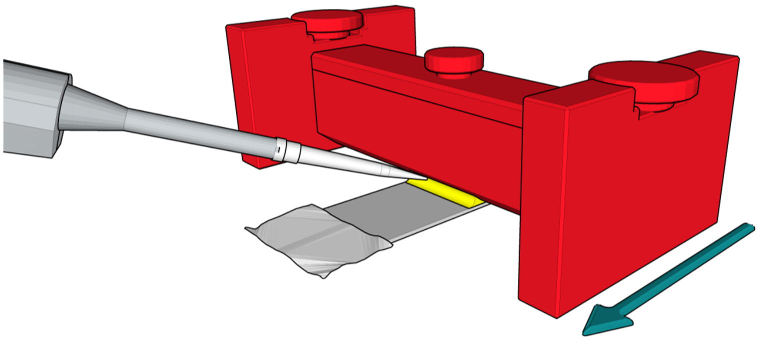

Figure 3.1: Doctor blading system. The solution is placed in front of the blade. The blade then forms the layer by pushing the solution through its gap.[54]

compared with spincoating is that the layer has a slower drying process that can lead to a different morphology of the film.

The doctor blading system (ZA A 2300, Zehntner GmbH Testing Instruments) used during this work was located at the Light Technology Institute. It was used both under nitrogen and ambient atmosphere. Two different applicators were used, the Universal-applicator (ZUA 2000 Universal-Applicator, Zehntner GmbH Testing Instruments) and a cylindrical applicator with different gap heights.

3.1.3 Thermal evaporation layer application

The hole transport layer and silver electrode were deposited using an evaporation machine (Spectros, Kurt J. Lesker Company LTD.) located at the LTI. The evaporation takes place under high vacuum of 10^{-6} bar. The evaporation machine has a three state pump system to reach this low pressure in approximately 15 minutes. The sample is then placed in a rotatory stage to guarantee a homogeneous deposition of the material. The layer thickness is measured through a quartz crystal. The crystal detects the change of frequency due to the change of mass. Two different crystals are used, one for dielectrics and one for metals. The materials are evaporated from two different sources, were they are heated using an electric current.

3.1.4 Cleanroom environment

Due the thin-film nature of OPV and OLEDs, particles on the atmosphere can greatly damaged them, creating shunts and shorts on the devices. Therefore, the devices were manufactured in the cleanroom in the LTI. The cleanroom is divided in three different rooms each with a different cleanroom class. The substrates were cut and etched in the first room with a cleanroom class of 100,000. Both spincoating and doctor blading systems were located in a room with yellow lighting and a cleanroom class of 1000 for the process under ambient atmosphere. For the processing of oxygen and water sensitive materials, the layers were deposited and characterized inside gloveboxes under nitrogen atmosphere.

3.2 Characterization methods

This section describes the different characterization methods required to measure the electrical and optical properties of OPV and OLEDs. The methods to characterize the laser and the laser structured lines are also described.

3.2.1 Topography characterization

One of the main needs for this work was to characterize the laser structured lines processes. A 3D confocal profiler was the main tool used for this purpose. An atomic force microscope and scanning electron microscope were also used.

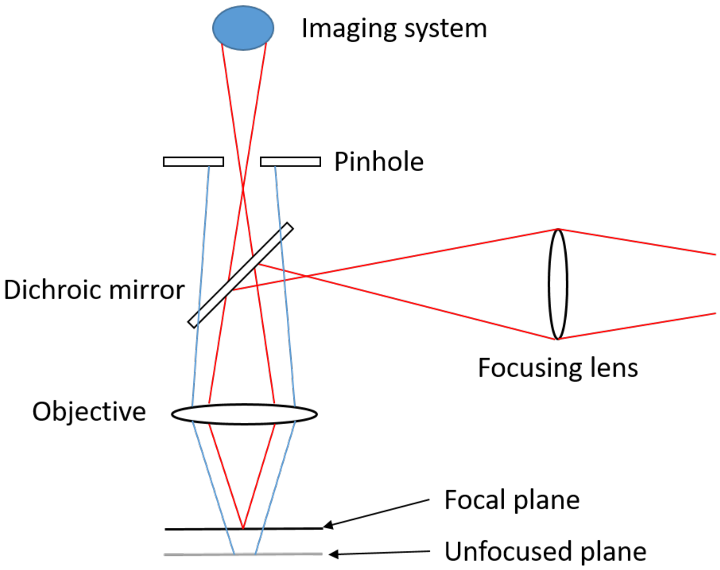

Figure 3.2: Confocal microscope working principle. The light coming from a light source is reflected using a dichroic mirror. The light that is reflected from the focal plane reaches the imaging system (red line) while the light that is reflected from other surfaces that are not in focus is blocked by the pinhole (blue line).

- A 3D profiler with confocal and white light interferometry functions (Sensofar Neox) was mainly used for the characterization of the structured layers. The confocal option was mostly used in this work. The profiler has two different objectives for confocal microscopy with two different amplifications 20x (NA=0.45) and 150x (NA=0.95), both from Nikon. It has two different light sources, blue and white. Confocal microscopy is a non contact 3D profiling method. Figure 3.2 shows the working principle. Light comes from a light source and it is focused. The focused light is reflected using a dichroic mirror. The light then is focused on the sample through an objective. The light that comes from the focal plane will be detected by the imaging system. The unfocused light (blue line) is blocked by a pinhole. This way the illumination and the observation are focused. In order to perform a 3D scanning, several pictures of this focused images are taken by changing the position in the Z-axis.[56] The Sensofar Neox can move with small steps of 100 nm. The system was also used to measure the size of the active areas of the solar modules and the width of the inactive areas. The confocal microscope is located at the Material Research center for Energy Systems (MZE).

- An atomic force microscope (AFM, Dimension Icon, Bruker) was used for in-depth measurements of the laser structured layers. The atomic force microscope works using a sharp tip that is attached to a cantilever (Figure 3.3). A laser beam is reflected on this cantilever to a photo diode. The forces due to the surface variations will deflect the cantilever by attracting the sharp tip. The photodiode detects the deflection of the cantilever by measuring the movement of the laser. All measurements done in this work were done in tapping mode. In this measurement mode, a piezo excites the cantilever to vibrate near its resonance frequency above the surface. A change in the

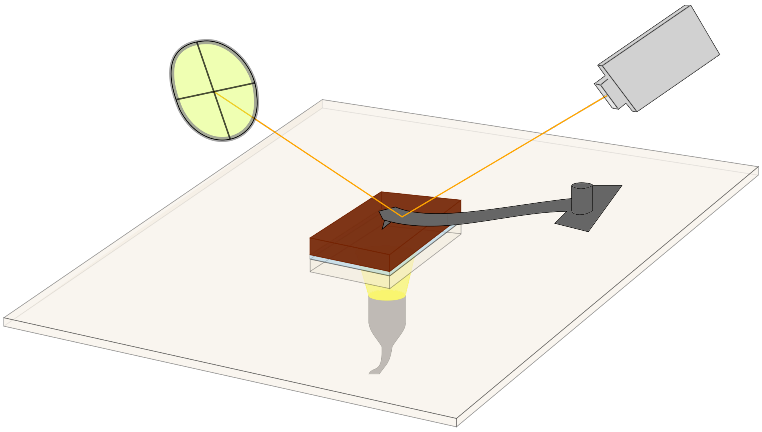

Figure 3.3: AFM tapping mode working principle. The cantilever scans the surface and detects the height variations. A laser is reflected on the cantilever. The height variations are measured by detecting the laser position variations.[58]

external potential, will alter the phase difference between the driving force and the cantilever oscillation amplitude. Both quantities can then be used as feedback signal. This method has the advantage that the tip barely touches the surfaces decreasing the tip wear.[57]

- A scanning electron microscope (FE-SEM, FEI Nova NANOSEM) was used for further analysis of the laser structured lines. The device was used in low vacuum with a gaseous analytical detector (GAD) and a low-vacuum detector (LVD). An electron beam scans the surface of the sample, releasing secondary electrons from the surface of the sample. The secondary electrons are then detected by a sensor, registering different levels of brightness. To analyze the edge of the laser structured samples, they were broken using liquid nitrogen. The samples were then measured using a tilt angle of 70°.

3.2.2 Optoelectrical characterization

To evaluate the performance of the devices and the absorption characteristics of the layers, different measurement techniques were used.

- A UV-VIS-NIR spectrometer (Cary5000 Agilent Technologies) was used to determine the spectral linear absorption of the different layers. Transmission (T) and reflexion (R) were measured using an integrating sphere. For the transmission measurements, the substrates were placed in front of an integrating sphere while for the reflexion measurements, they were placed behind. Absorption (A) was then calculated using the following relation:

$$A = 1 - R - T \tag{3.3}$$

- An integrated, home built OLED characterization system (OCS) was used to measure the electrical and optical characteristics of the OLEDs. The system is in a nitrogen atmosphere inside a glovebox in the LTI. The sample is placed on a XY stage. There are in total eight pins that were used to connect the different devices. A voltage is then applied to the device and the current density J of the device is recorded. The emitted light is measured through a fiber that is connected to a spectrometer (EEP 2000, StellarNet). The measuring position is calibrated using a laser. The calibrated spectrum ($\phi_e(\lambda)$) is recorded by the spectrometer. The luminous flux (ϕ) is then calculated using the following relation:

$$\phi = K_\mathrm{m} \int_{\lambda_1}^{\lambda_2} \phi_\mathrm{e}(\lambda) V_\lambda(\lambda) d\lambda \tag{3.4}$$

For the OLED modules, the measuring position was set next to the monolithic connection to measure the whole OLED module. The OCS is located in the cleanroom at the LTI.

- A solar simulator was used to evaluate the performance of the solar cells and modules. The solar simulator has a Xenon lamp that simulates the ASTM AM 1.5 solar spectrum. Different sample holders were used depending of the kind of substrate. For the 16 x 16 mm^2 a holder with 8 pins was used, allowing the subsequent measure of four solar cells on one substrate. For the larger modules, crocodile clamps were used. The voltage was applied using a Keithley Source Measure Unit (SMU). The current is measured, recorded and divided by the photoactive area of the device to calculate the current density. The software automatically determines the key performance parameters, V_oc, J_sc, PCE and FF. Before the measurements, the system is calibrated using a reference cell from Newport.

3.3 Laser ablation setup

The femtosecond laser ablation setup is composed of three main parts and it is located at the LTI:

- Ultrashort pulse amplifier (Libra, Coherent)
- Ultrafast optical parametric amplifier (OPerA Solo, Coherent)
- Workstation (µFAB, Newport)

The three parts are installed on top of an optical table (Newport) at the LTI. The beam is routed from the laser source to the workstation using different routing mirrors that are changed depending on the selected wavelength. Depending on the laser source, the position of the routing mirrors is modified. The main characteristics of each part are described below.

3.3.1 Ultrashort pulse amplifier (Libra)

The Libra is a chirp amplified laser that comprises:

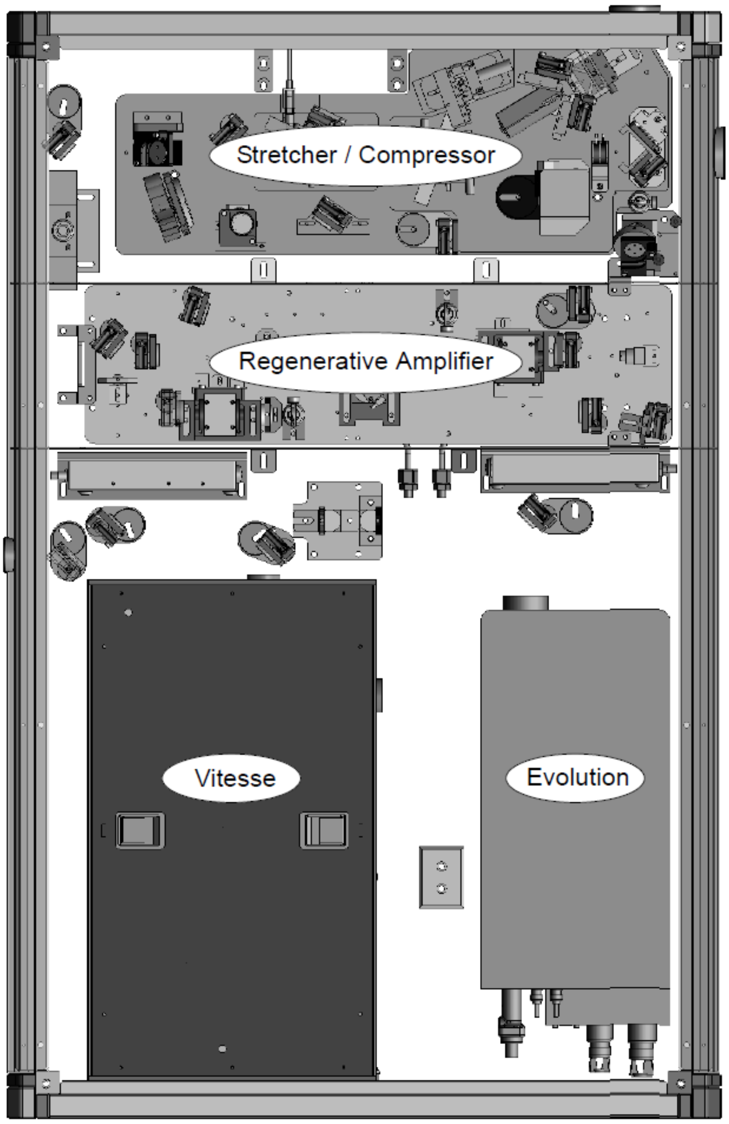

Figure 3.4: Libra optical bench assembly.The four main components of the Lbra are depicted.[59]

- Vitesse modelocked femtosecond laser (seed laser)
- Evolution Q-switch laser (pump laser)
- Synchronization and delay generator (SDG)
- Beam compressor/stretcher
- Regenerative amplifier
- Closed loop cooling chiller

The seed laser, the pump laser, the beam compressor/stretcher are all enclosed in the Libra optical bench assembly (Figure 3.4).

- The Vitesse laser works as the seed laser for the regenerative amplifier. It is composed of a modelocked Ti:Sapphire laser that is pumped by a continuous-wave diode-pumped green laser (Verdi Coherent).

Table 3.1: Libra output beam specifications.

Parameter	Value
Central wavelength (nm)	800
Average power (W)	3.6
Pulse energy (mJ)	0.72
Spatial mode	$\mathrm{TEM_{oo}}$, $M^2 < 1.3$
Polarization	Linear horizontal
Repetition rate (Hz)	5000
Pulse length (fs)	90

- The Evolution is a diode-pumped second harmonic Q-switched laser that provides the pump power for the regenerative amplifier. It operates at $\lambda = 527\,\mathrm{nm}$ and has a repetition rate of 5000 Hz.

- The regenerative amplifier amplifies one of the pulses of the seed laser using the pump power. The regenerative amplifier employs two Pockels cells. The first Pockels cell lets the pulse in the cavity after a certain number of amplification round (approximately 8-10), the second Pockels cell is activated letting the pulse out of the amplifier. The pulse is then send to the compressor. The amplification takes process in a Ti:Sapphire crystal where both seed and pump beam meet. The Pockels cells are regulated by the SDG. The whole regenerative amplifier is actively cooled by a chiller.

- The stretcher and compressor work with gratings. The compressor has a fine adjustment tool that helps to optimize the compression level of the output pulses. The beam takes several passes on the gratings to achieve the adequate stretching/compression level.

The output beam of the Libra has the characteristics depicted in table 3.1.

3.3.2 Ultrafast Optical parametric amplifier (OPerA Solo)

The ultrafast optical parametric amplifier (OPerA Solo) is a two-stage parametric amplifier of white-light continuum. The OPerA Solo is composed of the following subunits:

- Pump delivery and splitting optics (PO)
- White-light continuum generator (WLG)
- Pre-amplifier (PA1)
- Signal beam expander collimator
- Amplifier

Table 3.2: OPerA Solo wavelength regimes.

Regime	Wavelength Range (nm)
Idler	1650-2600
Signal	1175-1600
Second harmonic idler (SHI)	825-1150
Second harmonic signal (SHS)	580-800
Sum frequency idler (SFI)	540-600
Sum frequency signal (SFS)	480-530
Fourth harmonic idler (FHI)	400-480
Fourth harmonic signal (FHS)	290-400

The OPerA Solo installed in the LTI includes the optics necessary to work with the different wavelengths (table 3.2).

The output beam of the Libra is used as input beam. The beam is directed through routing mirrors to a beam splitter (BS1). Approximately, 4 % of the power is directed to the pre-amplifier stage (PAS). The bulk of the beam is directed to the power amplification stage. The small part of the beam is again split (BS2), one part will be used for the white-light continuum generation (WLC, approximately 1-3 µW) and the second part is used as the pump beam (30-70 µW) for the pre-amplification stage. The WLC is generated in a sapphire crystal plate (SC). The WLC and the pump beam are overlaped non-collinearly in the first non linear crystal (NC1) where, parametric amplification takes place. The residual pump and idler are blocked using a beam blocker (BB) while the signal is directed to the power amplification stage. In the power amplification stage the signal and the remaining of the pump are overlapped collinearly and non-collinearly in the second non-linear crystal (NC2). This results in collimated signal and idler beams. A dichroic mirror (DM) is used to separate the signal and the idler. If the signal is to be used, it is directed to the output of the OPerA Solo using a routing mirror (SM). In case the idler has to be used, the idler mirrors (IM1 and IM2) are installed. This mirrors are magnetic and have a fixed position. When installed they also block the signal beam. The optics for the generation of the second harmonic, sum frequency and fourth harmonic are installed after the position of the idler mirrors. A simplified schematic of the process is shown in figure 3.5.

The wavelength adjustments are done by changing the delay of the beams in the pre-amplifer and amplifier stages, and the crystal angles. This is controlled by a computer software. The computer software also controls the output wavelength. Besides the installation of the IM1 and IM2, different beam splitters need to be installed, depending on the operation regime that is chosen.

The pulse energy varies depending on the chosen wavelength. Figure 3.6 shows the different pulse energies at the output of the OPerA Solo for the different wavelengths. The highest efficiency of the system is 22.8% at $\lambda_{\text{signal}} = 1300\,\text{nm}$ and $\lambda_{\text{idler}} = 2066\,\text{nm}$. The beam will come out through one of the four different outputs of the OPerA Solo depending on the regime that is used.

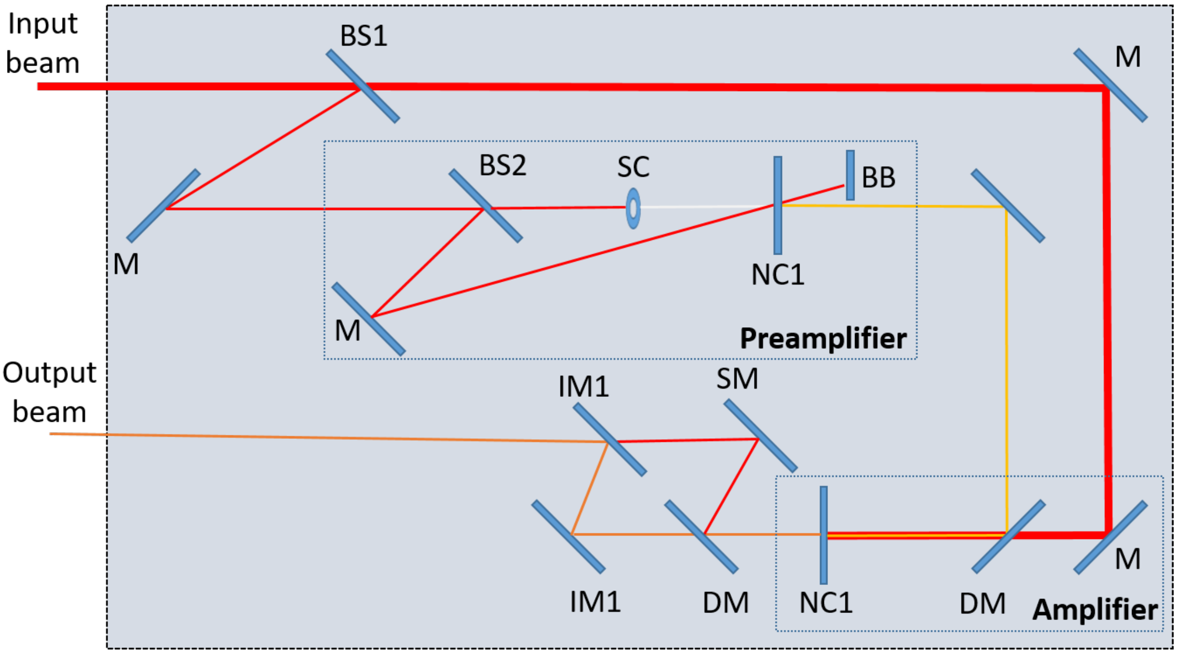

Figure 3.5: Simplified schematic OPerA Solo. The input beam is split (BS1). Around 4% is directed to the pre-amplifier while the bulk is directed to the amplifier. In the pre-amplifier the beam is split again (BS2). The smaller part is used to a generate white-light continuum (WLC) depicted as a white line. The larger part is used as the preamplifier pump. Both beams meet non-collinearly at the first non-linear crystal (NC1). Parametric amplification takes place. The signal beam is then directed to the amplifier while the idler and the rest of the pump are blocked with a beam blocker (BB). The signal meets the bulk of the input beam in the second non-linear crystal (NC2). Signal and idler beams are produced by the parametric amplification. A dichroic mirror separates the signal and the idler. In case of use of the idler, magnetic mirrors (IM1 and IM2) are installed. The mirrors block the signal beam. In case of using the signal the mirror SM directs the beam to the output.

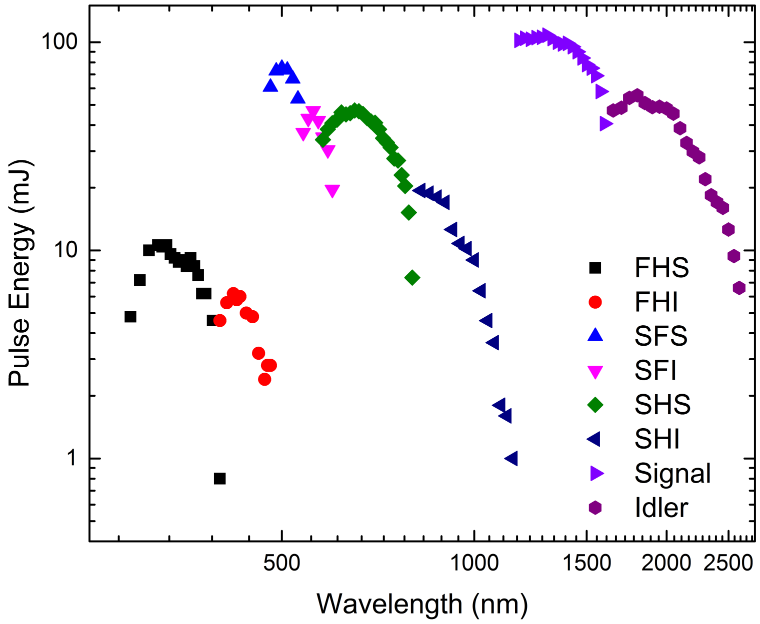

Figure 3.6: OPerA Solo pulse energies for different wavelengths and different regimes.

To monitor the output power of the OPerA Solo, a power meter (PS19, Coherent) with a resolution of 10 µW was used. During the scope of this work the wavelength range from $\lambda = 360\,\text{nm}$ to $\lambda = 750\,\text{nm}$ was used.

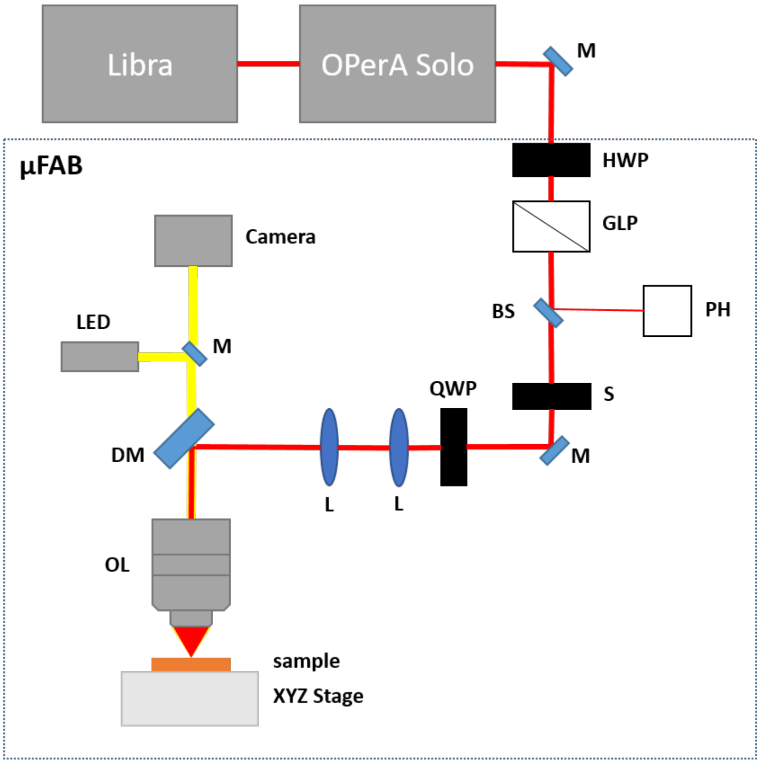

Figure 3.7: µFAB schematic showing the laser beam path from the entrance of the µFAB to the final focusing objective.

3.3.3 Workstation (µFAB, Newport)

The final part of the laser setup is the worktstation (µFAB, Newport). After the beam enters the workstation, the beam is attenuated using a 1/2 waveplate (HWP) combined with a Glan-laser polarizer (P). The HWP is attached to a software controlled rotatory stage. The polarizer lets a certain amount of light pass depending on the rotation angle of the HWP. Then the beams goes to a beam splitter (BS). A fraction of the beam is redirected to a power head (PH, Newport 918 DUV 0D3R). This fraction is used as reference to monitor the power on the sample. The beam goes to a mechanical shutter (S). After the shutter, the beam goes to a quarter waveplate (QWP) where the polarization is changed to circular. The beam then goes to a telescope for final collimation before being directed to the objective (OL). The sample is placed on an XYZ motorized stage. A CMOS camera is used as a positioning reference on the sample (Figure 3.7). The relationship between the power on the sample and the reference power changes with different wavelengths. Therefore a power relationship is measured on the sample position using a different power meter (USB UV/VIS, Coherent) in combination with the one on the workstation.

Two different objectives were used during this work, one for the visible and one for the UV regime, mainly at $\lambda = 360\,\text{nm}$. The specifications are given in table 3.3.

Table 3.3: Objectives specifications.

Parameter	Olympus RSM10x	Thorlab LM-5X-NUV
Working distance (mm)	10.5	35
Numerical aperture	0.25	0.13
Wavelength range (nm)	Visible	235-500

4 Laser principles

This chapter explains the basic working principles of a laser. Section 4.1 covers the theory behind the different laser sources used in this work such as modelocked, q-switching and chirp amplifiers. Section 4.2 covers the parametric amplification and non linear processes used in the OPerA Solo.

4.1 Working principle of a laser

Laser is an acronym for *light amplification by stimulated emission of radiation.* A laser is a device that produces and amplifies an intense beam of highly coherent and directional light. In 1960, Maiman extended the idea of the maser (microwave amplification by stimulated emission of radiation) to the infrared or visible region of the electromagnetic spectrum. A laser is basically composed of three main parts (Figure 4.1):[60]

- A gain medium to amplify the light through stimulated emission.
- A pump source, that provides the energy (current) to create the population inversion.
- A resonator or optical cavity, where the light is trapped. In its most simple form, the resonator is composed of two plane-parallel mirrors. This is known as Fabry-Perot resonator.

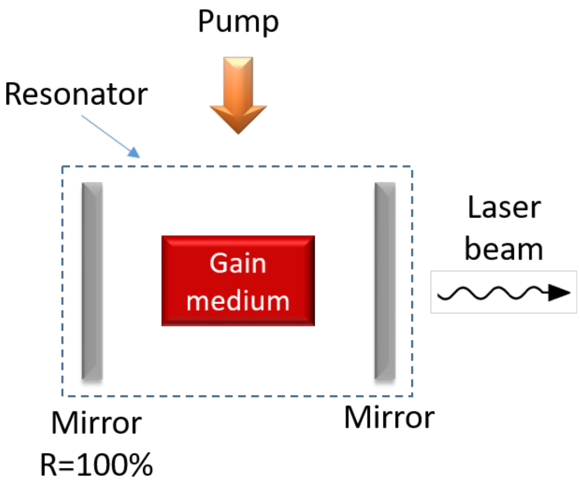

Figure 4.1: Schematic of a laser oscillator based on the Fabry-Perot resonator. The system is composed of a gain medium, the resonator and the pump source.

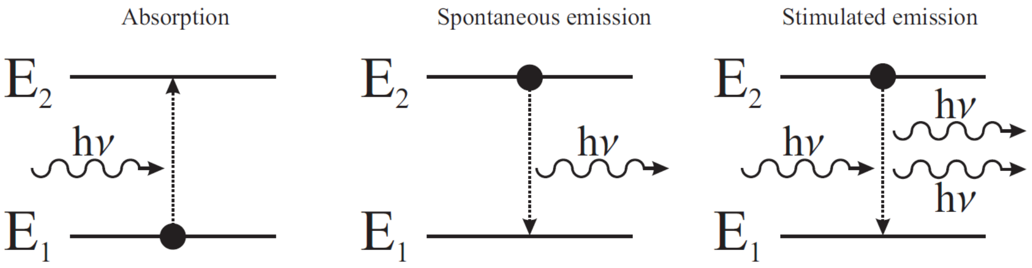

Figure 4.2: Absorption, spontaneous emission and stimulated emission in a two-level system with energies E_2 and E_1 .[61]

4.1.1 Light matter interaction

As discussed in chapter 2, light can be absorbed and emitted by matter with the excitation/decay of an electron. These two processes are called absorption and spontaneous emission. A third process is the so called stimulated emission of light. This process will be discussed in more detail below (figure 4.2)[61]:

- Absorption of a photon with energy hv=E_2-E_1. E_2 and E_1 are the energy of two different levels in the system where the light interaction occurs. The absorption causes the excitation of a particle from E_1 to E_2.

- Spontaneous emission of an emitted photon with an energy hv. This is caused by the decay of a particle from E_2 to E_1. The name spontaneous emission originates from the moment of emission, when the polarization and the direction of the light is random. This process is responsible for the fluorescence of excited media.

- When an incoming photon induces a resonant transition from E_2 to E_1, stimulated emission of a second photon of energy hv occurs. As it is resonant process both photons are identical. This effect allows the amplification of light which is fundamental for a laser.

4.1.2 Population inversion

Laser amplification occurs, if less light is absorbed than emitted. This is commonly referred to as effective gain. The equation for the effective gain is related to the effect of the light absorption described by the Lambert-Beer law:[61]

$$I(z,\lambda) = \ I(0,\lambda)e^{-\alpha(\lambda)z} \tag{4.1}$$

The absorption coefficient (λ) is proportional to the number density N_1 that describes the number of entities in state E_1.

$$\alpha(\lambda) = \sigma_{\mathrm{a}}(\lambda)N_1 \tag{4.2}$$

The proportionality constant $\sigma_{\mathrm{a}}(\lambda)$ is the absorption cross section. The stimulated emission (amplification) of light is:

$$I(z,\lambda) = \ I(0,\lambda)e^{\gamma(\lambda)z} \tag{4.3}$$

Similar to the previous case the emission coefficient $\gamma(\lambda)$ is proportional to the number density N_2 that describes the number of entities in state E_2.

$$\gamma(\lambda) = \sigma_\mathrm{e}(\lambda)N_2 \tag{4.4}$$

The proportionality constant $\sigma_\mathrm{e}(\lambda)$ is the emission cross section. When combining both processes, the total evolution of the spectral density is:

$$I(z,\lambda) = \ I(0,\lambda)e^{(\sigma_\mathrm{e}(\lambda)N_2-\sigma_\mathrm{a}(\lambda)N_1)z} \tag{4.5}$$

And the total gain of the system is:

$$G(z,\lambda) = \frac{I(0,\lambda)}{I(0,\lambda)}e^{(\sigma_\mathrm{e}(\lambda)N_2-\sigma_\mathrm{a}(\lambda)N_1)z} \tag{4.6}$$

To obtain a net amplification of light, G>1 is needed, hence N_2 needs to be larger than N_1. This is the so called population inversion, meaning that more entities populate the upper energy level E_2 than the lower energy level E_1. In thermal equilibrium, the population density relation between the two levels is directly given by the Boltzmann distribution:

$$\frac{N_2}{N_1} = e^{-\frac{h\upsilon_{21}}{k_\mathrm{B}T}} \tag{4.7}$$

It is not possible to achieve population inversion in thermal equilibrium, ergo an excitation source is required to excite the two level system (Figure 4.2). The ratio of N_2 and N_1 can be described using the Einstein coefficients B_{12} and A_{21} in steady state:

$$\frac{N_2}{N_1} = \frac{B_{12}u(\upsilon)}{B_{12}u(\upsilon)+A_{21}} < 1 \tag{4.8}$$

Where $u(\upsilon)$ is the radiation density of the excitation source. As seen in equation 4.8, an effective gain is not feasible, hence preventing the laser process in a two-level steady state system. An attainable way to achieve the population inversion is to add a third level to the system. The third level causes that absorption and emission occur at different wavelengths. When a three-level system is pumped, the population changes from level E_1 to level E_3 with a rate W_p. This brings an entity to the top level E_3. A fast decay from the level E_3 to the level E_2 occurs, keeping the population of level E_3 close to zero. When the absorption, the emission, and the spontaneous emission, plus the decay from level E_3 to level E_2 are considered, the change of N_2 in time is:

$$\frac{dN_2}{dt} = W_\mathrm{p}N_1 + W_{12}N_1 - W_{21}N_2 - A_{21}N_2 \tag{4.9}$$

Considering steady state. The ratio between N_2/N_1 is given by:

$$\frac{N_2}{N_1} = \frac{W_\mathrm{p} + W_{21}}{A_{21} W_{21}} \tag{4.10}$$

Therefore, it is possible to have a positive gain and population inversion in a three level system. However, this system has low efficiency as it has to compensate for the spontaneous emission rate. This leads to a high threshold to initiate the laser process.

To increase the efficiency, a four-level system is used. This principle follows the same idea that allowed the population inversion from the two-level system to the three-level system. It increases the efficiency by reducing the need of a high upper level population in N_2. The four-level system is represented in figure 4.3:

In the four-level system a pump is used to create an excitation to the level E_4. Similar to the three-level system a fast decay is necessary from the level E_4 to the level E_3 keeping the population of level E_4 close to zero. Also there is a fast decay from level E_2 to level E_1. The energy separation between E_2 and E_1 needs to be sufficient to prevent thermal population of E_2. This keeps the population of level E_2 close to zero. The population of N_3 considering the aforementioned processes is then given by:

$$N_3 = \frac{W_\mathrm{p}}{W_\mathrm{p} + W_{32} + A_{32} + A_{31}} \tag{4.11}$$

This leads to a population inversion of N_3 with respect to N_2, that has a population close to zero. The population inversion is present even with a low population accumulation in level three, hence decreasing the necessary pumping power and increasing the efficiency of the system.

Although the Ti:Sapphire laser that is mainly used in this work has a vibronic state configuration, its working principle can be approximated as a four-level system as shown in figure 4.4.

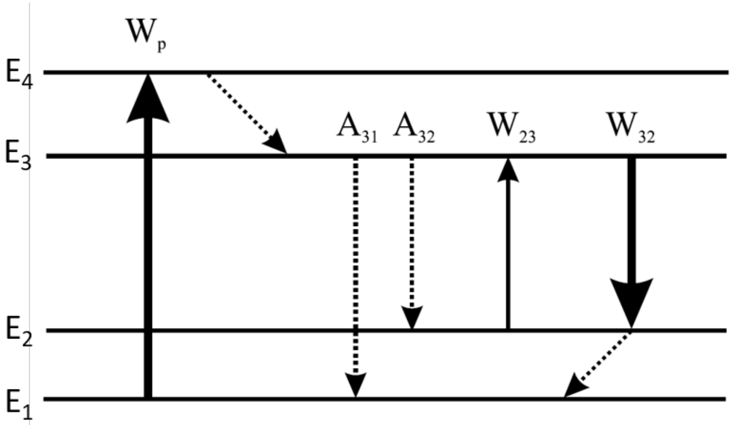

Figure 4.3: Four-level laser system and the light interactions within.[61]

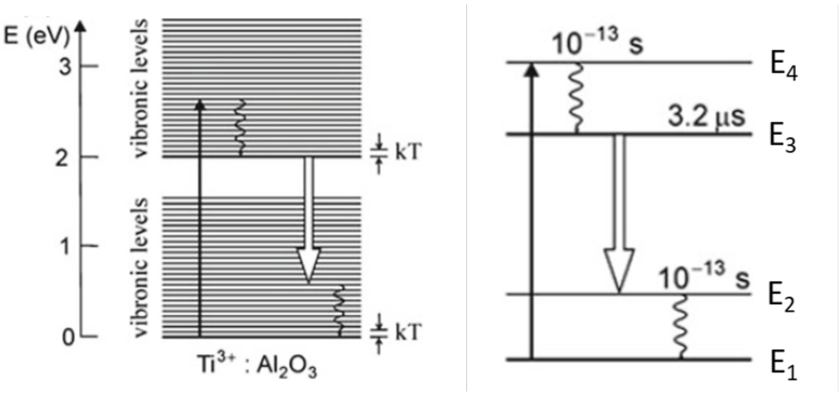

(a) (b)

Figure 4.4: (a) Vibronic states in a Ti:Sapphire laser. (b) Four-level energy approximation of a Ti:Sapphire laser.[62]

4.1.3 Feedback system

In the previous section, the necessary conditions to create population inversion are studied. As it is shown in figure 4.1 one of the main components of a laser is the resonator. This resonator is also known as laser cavity. One simple example of a resonator is the Fabry-Perot resonator that is composed of two different mirrors with different reflections. This allow us to reflect the amplified radiation back and forth in the gain medium. As seen in figure 4.1, one of the reflective mirrors has 100% reflection while the other mirror has less than 100%. This one is known as output coupler (OC mirror) as it allows the beam to leave the resonator.[61]

4.1.4 Types of lasers

Lasers can be classified in two main groups:[60]

- Continuous wave lasers (CW): this type of lasers has a continuous flow of output energy, with small or no time variations. Some examples are: HeNe and Ar-ion lasers.
- Pulsed lasers: this type of lasers has a variation in the flow of energy output, as the energy is emitted in pulses with an specific time range that can vary from µs to fs. Pulsed lasers are used in this work. Typical example are the Nd:YAG and the Ti:Sapphire.

Two of the most common methods to generate pulsed beams are Q-switching and modelocking, both are described below.

4.1.5 Q-Switching

Q-switching is a technique that uses the gain medium as an energy container. The energy is accumulated by not letting the beam escape through the outcoupling mirror. This creates a high level of population inversion that is far above the threshold for a CW operation of the laser. When the outcoupling mirror is activated, the stored energy is released in the form of

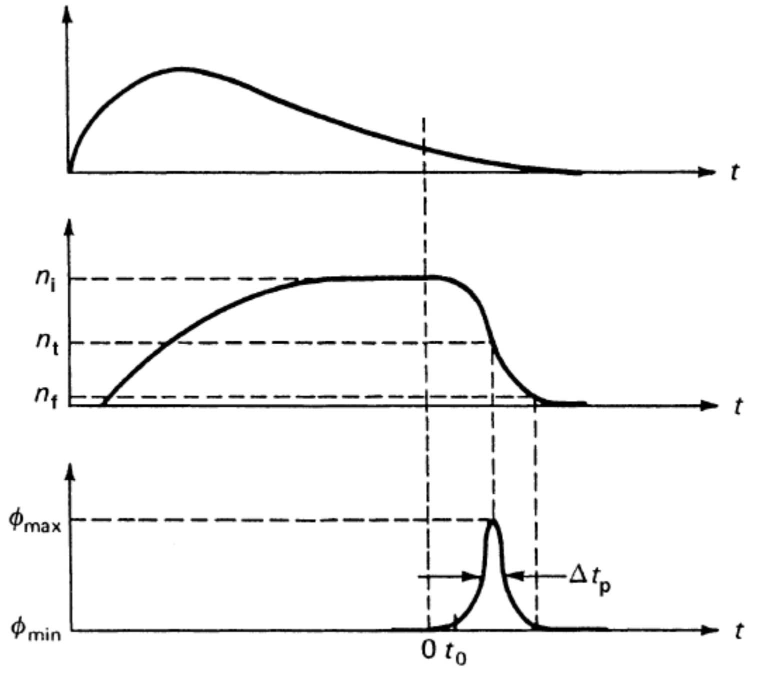

Figure 4.5: Q-Switching process description. The energy of the pump is accumulated in the gain medium. The outcoupling mirror is opened, and with a certain delay a pulse with duration t_p is released.[63]

a pulse of light after some delay. The pulse duration t_p is usually short in the range of ns. The peak power of this pulse is far greater than the normal peak power of a CW laser.[63] This process is depicted in figure 4.5. The Evolution is a Q-switching laser used in this work.

4.1.6 Modelocking

The short pulses generated using the Q-Switching process are limited to 20 ns. The limitation is due to the size of the resonator. To produce even shorter pulses in the ps and fs regime, mode-locking is used. The technique uses the fact that even lasers emit light in a certain bandwidth Δ_v. Therefore, the laser oscillates in the gain medium with a large number of longitudinal modes. The process induces the locking of the different modes that are inside the gain medium into one fixed phase. This is possible because all the frequencies are multiples of the same fundamental frequency. This allows the production of ultrashort pulses in the range of tens of fs.[64 65 61] The pulse width is inversely related to the bandwidth of the laser source by:

$$T_p \approx \frac{1}{\Delta_v} \tag{4.12}$$

Hence, a prime gain medium for mode-locking is Ti:Sapphire that has a $\Delta_v = 1.1 \text{ x } 10^{14}$ Hz. This is the type of gain medium inside the Vitesse, that is the laser used as seed inside the Libra.

4.1.7 Chirp Amplification

The chirp amplification technique is used to generate high-powered fs pulses. Different configurations for chirp amplifiers are used with one or two Pockels-cells. In a two Pockels-cell system (Figure 4.6), first, a standard fs mode-locking beam (seed pulse with low pulse energy in range of some nJ) enters the stretcher. The pulse is stretched, with the use of gratings, a factor of approximately 3000 for example from 200 fs to 600 ps. This helps to decrease the peak power of the pulse. The stretched pulse is then amplified using a regenerative amplifier. The cavity has a Ti:Sapphire crystal where amplification occurs. The pulse enters through a Pockels cell (PC1) where its polarization is changed. It is then amplified in the cavity with the energy of the pump laser. The amplification process requires several passes of the pulse through the crystal.

Once the pulse has achieved its peak pulse energy, the Pockels cell (PC2) changes the polarization of the light and sends it to the compressor by reflecting it on a polarizer (P). In the compressor, the pulse is again compressed into the fs regime using gratings. It is of high importance stretch the pulses. If the pulses in the fs regime are amplified directly, the power

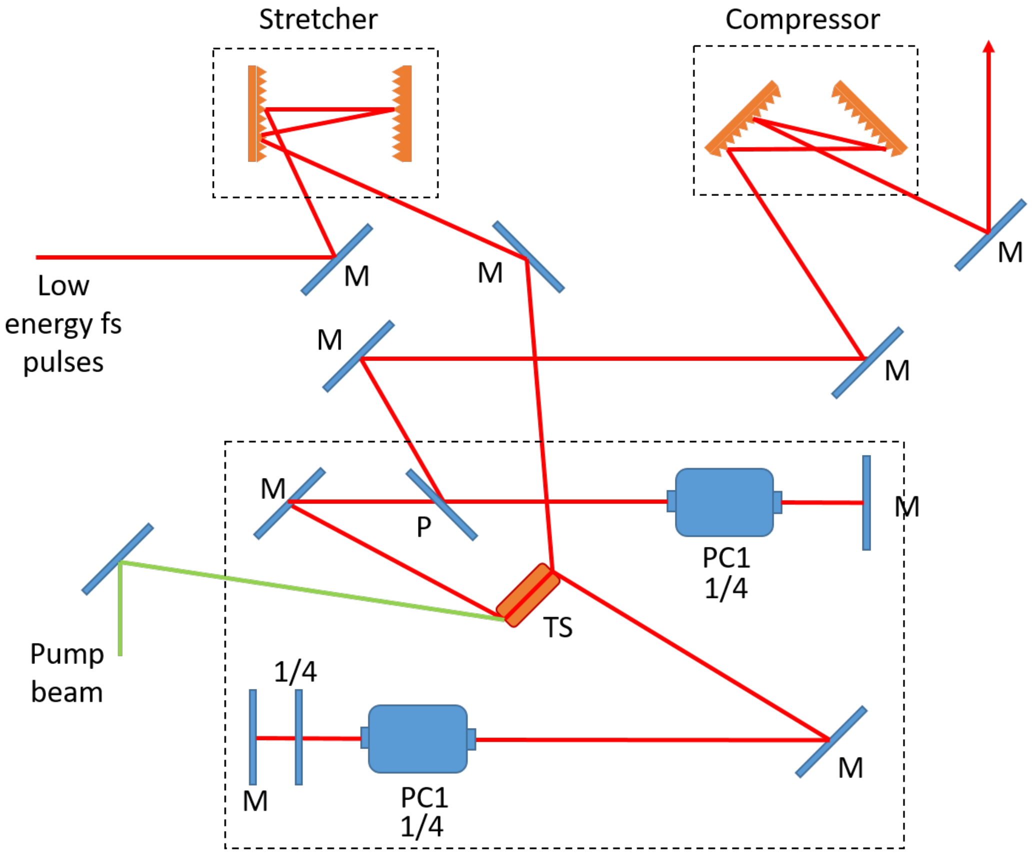

Figure 4.6: Chirp amplification process using two Pockels cells. The low energy fs pulses enter the stretcher. The gratings stretch the beam, lowering the peak power of the pulses. The beam is then sent to the regenerative amplifier where amplification takes place inside a Ti:Sapphire crystal. The polarization of the beam is changed by PC1 and the beam passes several times (8-10) in the Ti:Sapphire crystal where it is amplified using a pump beam. Once the beam has reached its maximum pulse energy, PC2 is activated, changing the polarization of the light by 90° with a double pass. This causes the polarizer (P) to reflect the light, routing it to the compressor. The pulse is then compressed to the fs regime using gratings.

would be too high for the crystal damaging it. This is the amplification process used inside the Libra, the fs laser system used in this work.

4.2 Wavelength tuning

4.2.1 Optical parametric amplification

The heart of the system used in this thesis is an optical parametric amplifier. This section will briefly explain the theory behind its working principle.

In an optical parametric amplification the input includes two beams, the signal beam and the pump beam. In the output, a new beam that is called the idler is obtained.[66] The following equations gives the energy conservation in a parametric amplification process:

$$\omega_\mathrm{p} = \omega_\mathrm{s} + \omega_\mathrm{i} \tag{4.13}$$

The pump beam frequency (ω_p) equals the addition of the signal (ω_s) and the idler (ω_i) beams' frequencies. This is depicted in figure 4.7.

The difference between the second harmonic conversion and the parametric amplification is that the signal beam is indeed amplified using this process and not only converted to the idler. This amplification comes from the conversion of some of the pump beam photons into signal and idler photons.

The energy condition mentioned in equation 4.13 allows the generation of any frequency smaller than ω_p. The frequency ω_s is controlled by the phase matching condition $\Delta\mathrm{k} = 0$. The phase matching can be modified either by changing the angle of the non-linear crystal or by changing its temperature.[66] The first option is the one used in both amplification stages inside the OPerA Solo.

4.2.2 Sum-frequency generation

The sum-frequency generation is an up-conversion process where two beams with frequencies ω_1 and ω_2 are combined to obtained a higher energy beam with frequency ω_3 (Figure 4.8).[66]

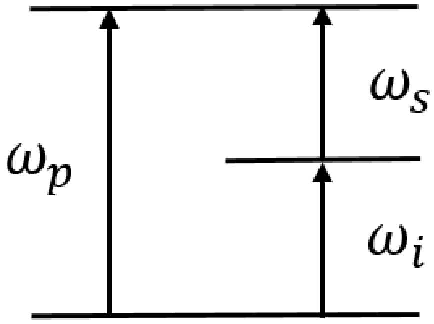

Figure 4.7: Frequency relationship in a parametric amplification between the pump, signal and idler beams.

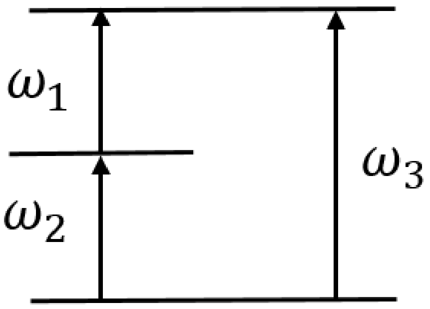

Figure 4.8: Frequency relationship in a sum-frequency interaction.

The process is used using Nd:YAG pulses at $\lambda_1 = 1064\,\text{nm}$, combined with its own second harmonic at $\lambda = 532\,\text{nm}$ to generate UV pulses at $\lambda = 355\,\text{nm}$.

A special case of the sum frequency generation is the second harmonic generation in which ω_1 and ω_2 are equivalent and ω_3 results in a frequency doubling. If this process is repeated, the fourth harmonic is obtained.

These processes sum-frequency, second harmonic and fourth harmonic are used in the OPerA Solo. The OPerA Solo applies the aforementioned process to the signal and idler beams allowing us to achieve different wavelengths.

5 Laser processing

This chapter covers the fundamentals of laser processing. The interaction of lasers with matter is a complex process that depends on the type of material, the laser wavelength, the laser intensity, the pulse length etc. Section 5.1 gives a short introduction to the matter-laser interaction processes. Section 5.2 covers the principle of nanosecond laser ablation. Section 5.3 covers the principles of the ultrashort pulse laser ablation, the methods to determine the laser threshold fluence and the pulse overlap.

5.1 Laser matter interaction

The interaction between the laser beam and the matter depends on different factors. On the laser side, the parameters that play an important roll are: type of beam (continuous or pulsed), wavelength, intensity, coherence, polarization, beam shape and angle of incidence. On the material side, the chemical composition and the microstructure will determine the interaction with the laser beam.[67] Depending on the laser intensity, different interactions may occur. An overview is depicted in figure 5.1.

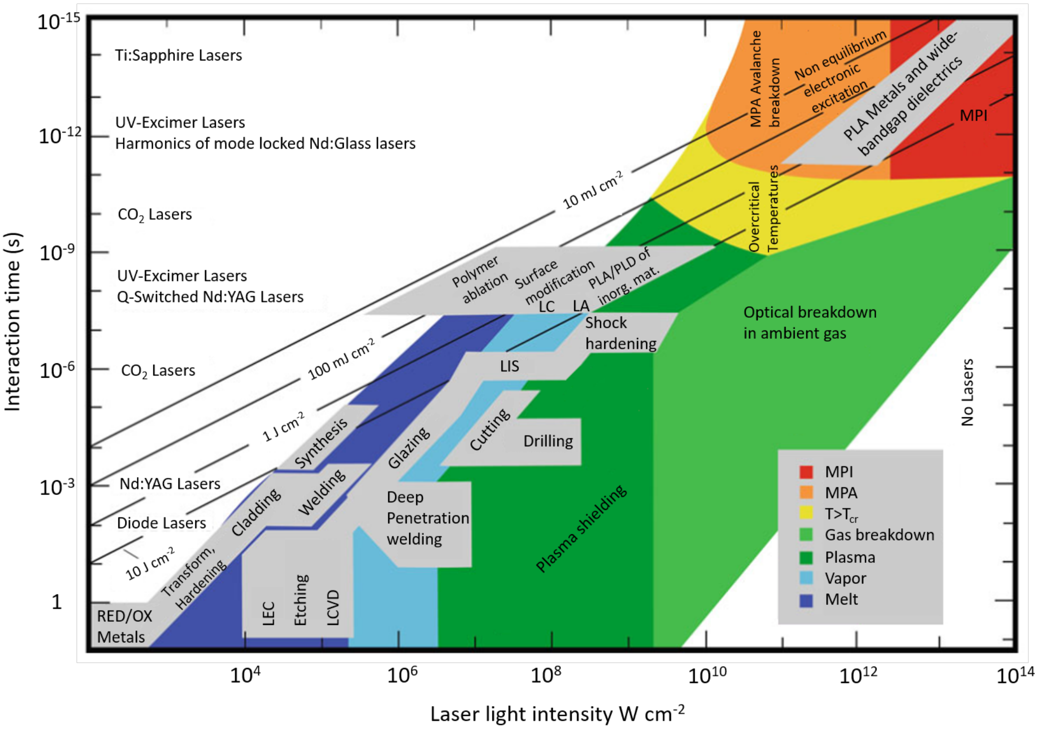

Figure 5.1: Overview of different laser-matter interactions depending on the laser intensity. The types of lasers to achieve this interactions are indicated.[67]

Laser material processing can be classified as: photothermal and photochemical. A photothermal process occurs when the thermalization of the energy (heat transmission) to the bulk of the material is faster than the process itself (evaporation, melting etc). On the contrary, a photochemical process occurs when the process is faster than the thermalization. In this case, a small heat transfer occurs. When both types of reactions occur on the material, the process is known as photophysical.[67]

In general, the primary excitations of a laser source with matter are not thermal. Some of the possible interactions on solids are: electronic excitations (interband and intraband excitations, excitons etc.) and excitations of phonons, polaritons etc. Impurities and defects can also create vibrational states where the laser can interact. All this interactions affect the amount of energy that is absorbed on the material. Similar to an incoherent light source, not all the light power that is applied by a laser source on a surface is absorbed by it. Part of it is reflected (P_{R}), part of it is absorbed (P_{A}) and part of it is transmitted (P_{T}).[68] The coupling efficiency on a material then is given by:

$$\eta_A = \frac{P_{\mathrm{A}}}{P} \tag{5.1}$$

Where P is the laser power. The amount of power on the sample can also be described with the intensity I in $\mathrm{W\,cm^2}$. The intensity dependence related with the depth Z is given by the Lambert-Beer law through the following relation:

$$I(z) = (1-R)I_{\mathrm{o}}e^{-\alpha z} \tag{5.2}$$

As the laser absorbed intensity is transformed into heat, the temperature distribution caused by the laser can then be described using the heat equation if the convection and radiation losses are disregarded.

$$Q(x,t) = \rho(T)c_{\mathrm{p}}(T)\frac{\delta T(x,t)}{\delta t} - \nabla[k(T)\nabla T(x,t)] + \rho(T)c_{\mathrm{p}}(T)\upsilon_{\mathrm{s}}\nabla T(x,T) \tag{5.3}$$

Where $\rho(T)$ is the mass density, $c_{\mathrm{p}}(T)$ is the specific heat coefficient at a constant pressure. υ_{s} is the speed of the sample with respect to the laser source. From this equation, it can be observed that the laser behaves as a heat source.

The thermalization time is another important concept to describe the laser-matter interaction. The thermalization time changes depending on the material that is treated. In metals, light is absorbed by the electrons. The time between electron-electron collisions is around 10^{-14} to 10^{-12} s. The relaxation time between the electron and the lattice through a phonon is then between 10^{-12} to 10^{-10} s. If the thermalization time is longer than the pulse length of a laser, equation 5.3 is not valid.

5.2 Nanosecond-laser ablation

The removal of material using short high-intensity laser pulses is known as laser ablation. Laser ablation suppresses the dissipation of thermal energy on the sample beyond the volume that is affected on the sample. To preserve this condition the thickness of the layer ablated by the pulse is in the order of the heat penetration depth $\mathrm{l_T} \approx 2(\mathrm{D_{Tl}})^{1/2}$ or the optical penetration depth $\mathrm{l}_\alpha = \alpha^{-1}$, the larger one will be considered for this purpose.

5.2.1 Nanosecond ablation mechanisms

The thermal ablation process starts when photons are absorbed increasing the temperature of the material. The increase on temperature changes the material properties, modifying the absorption of it. If the temperature rises beyond the evaporation temperature T_v the material is removed by evaporation with or without melting. Another possibility is that the increase of temperature increases the volume of the material under the laser beam. This induces a mechanical stress that, for certain materials, can create a pop-off. The stress changes the material properties as well, therefore changing the absorption of light.

Photochemical ablation occurs when the intensity of the nanosecond laser source is high enough to induce a direct bond breaking, removing the single molecules from the material surface. The broken bonds can also induce a mechanical stress that might result in a pop-off similar to the one described before. This process takes place without change on the surface temperature. The combination of both processes is known as photophysical ablation. In this process, both chemical and thermal processes contribute to the ablation rate.

The most common mechanism for laser ablation using a nanosecond laser in the IR, VIS and UV regimes is a thermal process. Hence, thermal evaporation is the dominant mechanism where surface melting is observed. The temperature and the ablation velocity of a surface hit by a laser source is depicted in figure 5.2.[67] The surface heats up to a stationary temperature T_st. T_st is reached after the evaporation of the material starts at time t_v. The constant ablation speed is reached at time t_st. After the pulse is over τ_l the cooling of the substrate begins. It is important to consider that, with nanosecond pulses the stationary regime is often not reached. Similarly, stored energy might caused the ablation of material even after the pulse is over.

Considering the temperature distribution described above (figure 5.2), the ablation rate by a laser pulse can be divided into different layers as described by:

$$\Delta h \approx \Delta h_1 + \Delta h_2 + \Delta h_3 + \Delta h_4 \tag{5.4}$$

Δh_1 describes the ablated material between the beginning of the heating process and t_v. This ablation is negligible and hence it is ignored. Δh_2 describes the ablation between t_v and t_st. Δh_3 is the ablation that occurs when the material is in the stationary temperature. In some cases the pulse inserts a large amount of energy to the substrate and the ablation is then described by Δh_4. In a nanosecond pulse, the three final steps play an important

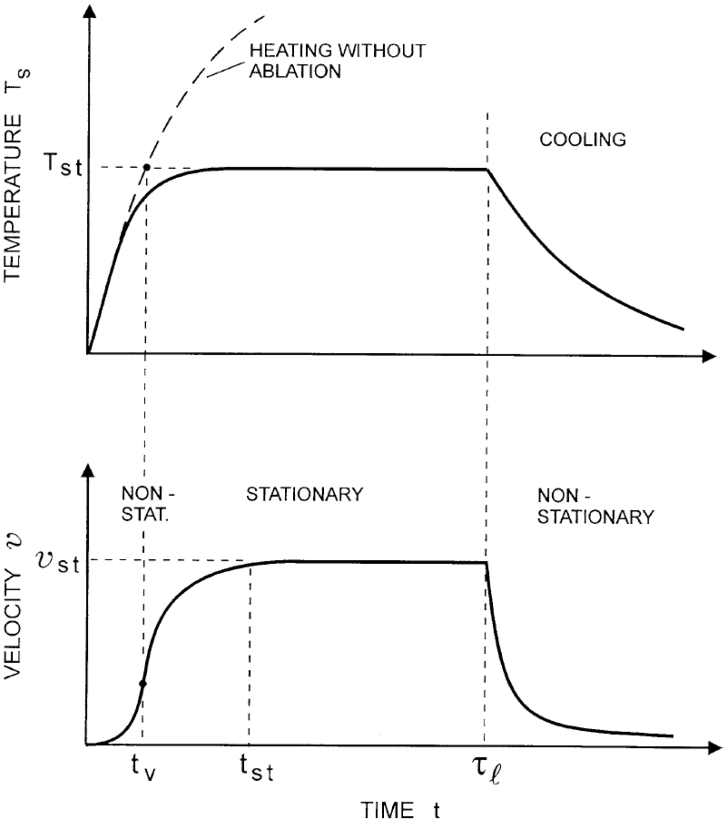

Figure 5.2: Temperature and ablation velocity schematic of a surface hit by a nanosecond pulse. In the initial stage the material heats up to a stationary temperature T_{st}. This point is after the evaporation time t_{v} is reached. After the pulse is over τ_{l} the material cools down. The ablation velocity becomes constant after T_{st} is reached.[67]

role in the ablated volume. The ablation threshold can be calculated considering the three ablation steps (Δh_2 to Δh_4) as a single contribution given by:

$$\Delta h \approx B(F - F_{\mathrm{th}}) \tag{5.5}$$

Where B is the ratio between the absorptivity and the material enthalpy, F is the fluence, F_{th} is the threshold fluence. Therefore, for the ablation to be significant the difference between the fluence and the threshold fluence needs to be larger than the enthalpy of the material. The threshold fluence (F_{th}) is defined as the fluence where significant ablation is observed. This depends on the material, its micro structure, material defects and on the laser parameters, especially laser wavelength and pulse duration. Typical values for bulk metals are within the range of 1 - 10 J cm^{-2}, for dielectrics in the range of 0.5 - 2 J cm^{-2} and for organic materials in the range of 0.01 - 1 J cm^{-2}. It is important that, for thin films, F_{th} depends on the film thickness.

Finally, the previous description considers one pulse per place. When several pulses occur in the same place, the so called incubation effect takes place. The incubation effect affects the absorption of the material increasing it in some cases. This leads to ablation below the F_{th}. An empirical relation for the threshold fluence depending on the number of pulses on the spot is given by:[69]

$$F_{\mathrm{th}}e(N) = F_1 N^{S-1} \tag{5.6}$$

Where F_1 is the single pulse threshold fluence, N is the number of pulses and S is the incubation coefficient. Therefore, it is expected that with a larger number of pulses in the same location, the fluence necessary to ablate will decrease. The incubation effect is due to increase of the absorption of the material. The absorption increase may be due to surface modifications.

Although, nanosecond ablation offers unique advantages, for certain materials the pulses are too long for high quality structuring, specially for materials with high thermal conductivity. Therefore, pico and femtosecond laser ablation are feasible options that will be discussed in the following section.

5.3 Ultrashort pulsed laser ablation

Ultrashort pulse laser ablation offers the advantage over nanosecond ablation of lower heat affected zones (HAZ) and higher precision structuring. It is mentioned in section 5.1 that the relaxation time between the electron and the lattice is between 10^{-12} to 10^{-10} s. If a material is ablated with a pulse which has a duration of 100 fs all the interactions within the material are electronic as there is not enough time for transmission of the energy from the electrons to the lattice. Figure 5.3 depicts the different interaction times for femtosecond laser interaction in metals and dielectrics.[70]

The higher structuring precision originates from the gaussian shape of the pulse. At lower fluences closer to the threshold fluence, just the highest energy part of the pulse removes the material. This allows high structuring precision, smaller than the spot size of the laser beam.

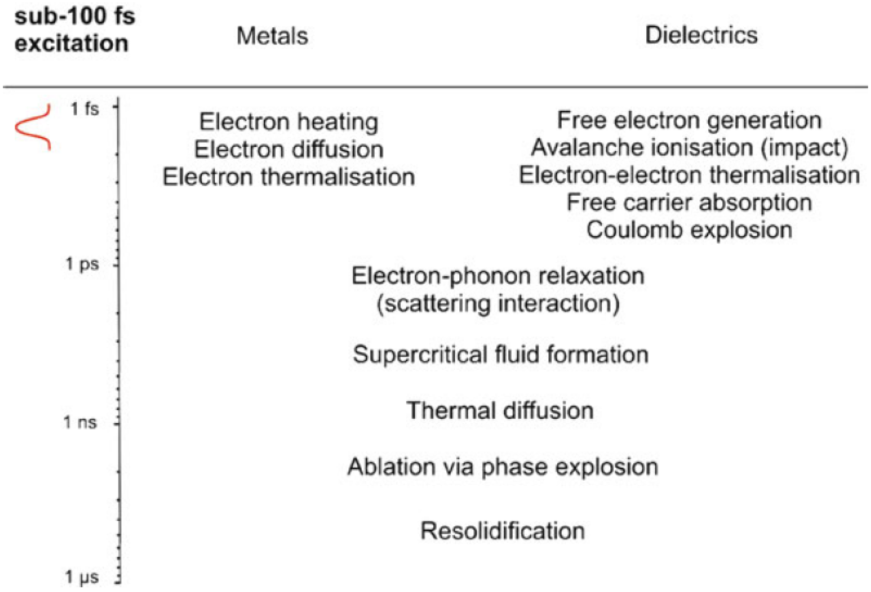

Figure 5.3: Interaction times of femtosecond pulses with dielectric and metals.[70]

5.3.1 Ablation mechanisms in dielectrics and metals

The ablation process using ultrashort pulses is different for dielectrics and metals. For dielectrics the initial step is to generate free electrons. The number of free electrons generated in the material is defined by:

$$\frac{\delta n_{\text{total}}}{\delta t} = n_{\text{mpi}}(I) + \beta(I)n \tag{5.7}$$

where n_{mpi} is the generation of free electrons due to multiphoton absorption and $\beta(I)$ is an intensity dependent impact ionization rate. Multiphoton absorption is strongly dependent on the laser intensity. For a pulse duration of 100 fs multiphoton ionization is the dominant absorption mechanism for laser intensities higher than $10^{14}\,\mathrm{W\,cm^{-2}}$.[71] Once the energy is absorbed and the free electrons are generated, the electron to electron collisions is multiplied by the inverse Bremsstrahlung (avalanche ionization). During this process electrons are accelerated by the energy provided from the laser beam. The free electrons increase the laser absorption leading to a higher number of free electrons. Due to the high density of free electrons the dielectric starts to behave as a metal. Afterward, the electrons leave the material, leaving a high concentration of positive ions on the surface. This positive ions then are removed in the so called Coulomb explosion. The Coulomb explosion is a non-thermal process. After the pulse passes, the electrons transmit the remaining energy to the lattice and thermalization occurs.[70]

For metals the case is different as the electrons are already free. The electrons that absorb the light take up energy. This leads to electron - electron thermalization, a process that takes place in tens of fs. The diffusive energy transport by the high energy electrons will take place as long as there is no thermal equilibrium between the electrons and the lattice. The thermal diffusion length that comes with this energy transfer is the key parameter for fs laser ablation.

As the temperatures of the electrons and the lattice differs for both dielectrics and metals, the surface temperature cannot be described using the classic heat equation (Equation 5.3).[70] Instead two coupled differential equations are then needed:

$$\begin{aligned} C_{\text{e}}\frac{\partial T_{\text{e}}}{\partial t} &= \nabla\cdot(k_{\text{e}}\nabla T_{\text{e}}) - \Gamma(T_{\text{e}} - T_{\text{l}}) + Q \\ C_{\text{l}}\frac{\partial T_{\text{l}}}{\partial t} &= \nabla\cdot(k_{\text{l}}\nabla T_{\text{l}}) - \Gamma(T_{\text{e}} - T_{\text{l}}) \end{aligned} \tag{5.8}$$

Where T_{e} and T_{l} are the electron and lattice temperature, C_{e} and C_{l} are the heat capacities of the electron and the lattice and k_{e} and k_{l} are the electron and lattice heat conductivities. The Term Γ accounts for the coupling between the two equations. Q is the laser source that, in most cases, is assumed to have a Gaussian profile.

5.3.2 Theoretical threshold fluence determination

Gamaly et al. developed a model to estimate the threshold fluence for dielectrics and metals.[71] The model starts using equation 5.7, evaluating the possibilities of having impact ionization or multiphoton absorption. The final result for dielectrics is given by:

$$F_{\mathrm{th}}^{\mathrm{d}} = \frac{3}{16}(\epsilon_{\mathrm{b}} + J_{\mathrm{i}})\frac{\lambda n_{\mathrm{e}}}{\pi} \tag{5.9}$$

and for metals:

$$F_{\mathrm{th}}^{\mathrm{m}} = \frac{3}{16}(\epsilon_{\mathrm{b}} + \epsilon_{\mathrm{esc}})\frac{\lambda n_{\mathrm{e}}}{\pi} \tag{5.10}$$

where ϵ_{b} is the ion binding energy, J_{i} is the ionization potential and ϵ_{esc} is the work function of the material. According to equation 5.9 the laser needs to overcome the ionization potential to create free electrons plus the binding energy of the ions, resulting in material ablation. For the metals (equation 5.10), the ionization potential and the ion binding energy need to be overcome. A linear relationship with the wavelength (λ) is also observed.

5.4 Threshold fluence determination and pulse overlap

As discussed above, the threshold fluence is the fluence where significant ablation is observed. Therefore, it is important to find an accurate method for its determination. Liu found a logarithmic relationship between the squared diameters of the single ablation spots and the threshold fluence.[72] This method has been further explained in different sources.[73 37]. The relationship found by Liu is given by:

$$D^2 = 2W_0^2 \ln(\frac{F}{F_{\mathrm{th}}}) \tag{5.11}$$

Where W_0 is the beam radius at the laser spot, D is the spot diameter. Due to the difficulties to measure W_0 accurately, the fluence is substituted by the pulse energy using the relationship:

$$F = \frac{E_{\mathrm{pulse}}}{\pi W_0^2} \tag{5.12}$$

where E_{pulse} is the pulse energy E. Leading to the equation below;

$$D^2 = 2W_0^2 \ln(\frac{E}{E_{\mathrm{th}}}) \tag{5.13}$$

Then the different squared diameters are plotted against the pulsed energies. In a graphical representation, a logarithmic scale is used on the x-axis, leading to a linear relationship. From the slope of the graph, W_0 is determined. Similarly, from the equation obtained from the linearization the threshold pulse energy (E_{th}) is calculated. Finally, using equation 5.12, the threshold fluence is calculated.

A laser written line is constructed by overlapping the pulses. The pulse overlap is optimized by testing different ablation speeds. The pulse overlap is given by:

$$\text{Pulse overlap} = 1 - \frac{V}{2W_0 f} \tag{5.14}$$

Where f is the frequency of the laser and V is the structuring speed. The pulse overlap is important as a too high pulse overlap can lead to damage of the materials below. An insufficient pulse overlap may lead to incomplete electrical insulation and shorted electrodes, or poor contact between the electrodes in the case of a monolithic connection.

6 Femtosecond laser structuring of ITO on PET

Indium tin oxide (ITO) is a transparent conducting oxide that is commonly used in OPV and OLEDs. It has a high transmission of 90 % in the visible spectral regime and a sheet resistance $R_\square = 12\,\Omega\,\square^{-1}$ *on glass and transmission of 80 % with a sheet resistance* $R_\square = 60\,\Omega\,\square^{-1}$ *on PET. To be used as an electrode in organic electronics, the ITO layer needs to be structured. Methods to pattern the ITO often involve chemical etching or photolithography which offer high quality but are not compatible with roll-to-roll production.*[74,75] *Ultrashort pulsed laser ablation is a proven technique to structure ITO on glass, producing high quality ablation with low bulges and electrical isolation of the different parts.*[76–78] *Similarly, ultrashort pulsed laser ablation has been used to structure ITO on PET.*[79–82] *However, the structuring of ITO on PET produced undesirable high bulges. The bulges may lead to shunts and defects in the devices as the layers on top are not thick enough to cover the bulges due to the thin-film nature of the devices. Hördemann introduced a method to reduce the height of the bulges by using a sacrificial layer reducing the bulge height to less than 50 nm.*[83] *The bulge height was also reduced using 5 passes with* $PO = 70\%$ *to less than 100 nm. Other ideas were tested like using different beam shape like Top-Hat or Donut, but bulges higher than 100 nm were still produced. In this chapter, the ablation of ITO on PET (*$T_{500\,nm} = 80\%$*,* $R_\square = 60\,\Omega\,\square^{-1}$*, thickness = 90 nm, Sigma Aldrich) was explored. First the threshold fluences ITO and PET were calculated for different wavelengths. The results are compared to the respective absorption spectrum (section 6.1). The ITO structuring process was then optimized for different wavelengths (section 6.2). Finally, section 6.3 concludes this chapter.*

6.1 Threshold fluence characterization

The threshold fluences, for both ITO and PET, were determined using the Liu-method described in section 5.4 for eight different wavelengths $\lambda = 360$ nm, $\lambda = 410$ nm, $\lambda = 450$ nm, $\lambda = 500$ nm, $\lambda = 550$ nm, $\lambda = 600$ nm, $\lambda = 650$ nm and $\lambda = 700$ nm. Direct ablation was performed on the ITO side. The calculated focused waists were $W_0 = 6.4\,\mu\text{m}$ at $\lambda = 360$ nm and $W_0 = 3.8\,\mu\text{m}$ at $\lambda = 700$ nm. The difference is due to the different numerical apertures of both objectives. Single pulse ablation was achieved by scribing lines using a speed of

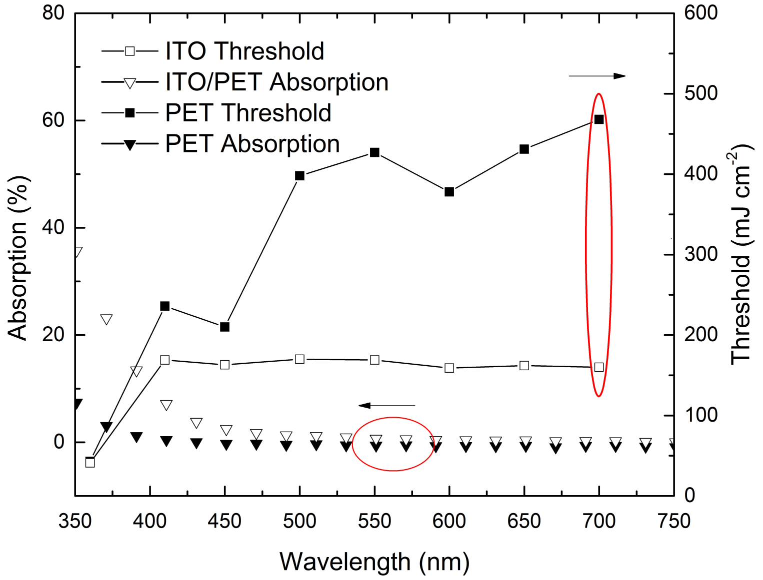

Figure 6.1: Threshold fluences at different wavelengths and absorption spectrum of ITO and PET. The threshold fluence shows no change for the ITO between $\lambda = 410\,\text{nm}$ and $\lambda = 700\,\text{nm}$, however for PET it shows an increasing value with increasing wavelength. The maximum working window for selective ablation, marked in red, is given at $\lambda = 700\,\text{nm}$.

$180\,\text{mm}\,\text{s}^{-1}$. The measured threshold fluences and the absorption spectrum, for both ITO and PET, are depicted in figure 6.1.

A relationship between the absorption spectrum of ITO and its threshold fluences can be observed. At $\lambda = 360\,\text{nm}$, the absorption increases to 30%, translating in a reduction of the threshold fluence from $F_{\text{th}} = 170\,\text{mJ}\,\text{cm}^{-2}$ to $F_{\text{th}} = 40\,\text{mJ}\,\text{cm}^{-2}$. Between $\lambda = 410\,\text{nm}$ and $\lambda = 700\,\text{nm}$, the threshold fluence of ITO remains constant at $F_{\text{th}} = 170\,\text{mJ}\,\text{cm}^{-2}$ matching the absorption spectrum that remains constant with almost no absorption. The threshold fluence is different to the $F_{\text{th}} = 250\,\text{mJ}\,\text{cm}^{-2}$ reported by McDonell et al. for $\lambda = 343\,\text{nm}$ at $\lambda = 1030\,\text{nm}$.[80] The difference can be explained by the different pulse length used in both studies, 90 fs compared to 500 fs.

The threshold fluence for PET does not follow the absorption spectrum as it shows an increasing magnitude towards higher wavelengths while the absorption strength remains constant. This matches equation 5.9 where a linear dependency of the threshold fluence on the wavelength is described. The equation does not describe the threshold fluences of ITO. One possible explanation is that the equation was developed to describe bulk materials such as the PET substrate rather than transparent thin-films such as ITO.

Finally, the best wavelength to achieve selective ablation is at $\lambda = 700\,\text{nm}$ where the working window is the largest. The working window is the difference between the threshold fluence of ITO and PET. This is marked in red in figure 6.1. In contrast, selective ablation at $\lambda = 360\,\text{nm}$ is complicated as both materials have a similar threshold fluence, $F_{\text{th}} = 40\,\text{mJ}\,\text{cm}^{-2}$.

6.2 Structuring process optimization

In this section the line structuring at different wavelengths was explored, focusing on selective ablation and low bulge generation. The different laser-written lines were ablated using changing stage speeds, leading to different pulse overlaps. If the pulse overlap is not sufficient, the ITO is not fully removed and electrical insulation may not be achieved. In contrast, if the pulse overlap is excessive, selective ablation is not obtained leading to damage to the layer below, in this case the PET substrate.

Laser structuring at λ=360 nm

Single pulse ablation was performed on the ITO layer. Figure 6.2a shows the single pulse ablation using a fluence $F = 60\,\mathrm{mJ\,cm^{-2}}$. Although the threshold fluences for both materials are identical at $F_{\mathrm{th}} = 40\,\mathrm{mJ\,cm^{-2}}$, the ablation shows negligible damage on the PET substrate below. The ablation depth is approximately 80 nm showing complete removal of the ITO layer. The bulges created by the ablation are higher than 200 nm.

Although single pulse ablation led to selective ablation, the pulse overlap resulted in some damage of the PET substrate below. Figure 6.2b shows a laser-written line with a pulse overlap of 66% and a fluence $F = 53\,\mathrm{mJ\,cm^{-2}}$. Even with lower fluence than the one used for the single pulse ablation, the PET substrate was damaged (black spots on Figure 6.2b). The damage stems from the close threshold fluences $F_{\mathrm{th}} = 40\,\mathrm{mJ\,cm^{-2}}$ for both materials at $\lambda = 360$ nm. It can also be noted that, in some areas, the ablation was not complete, therefore leading to shortened electrodes.

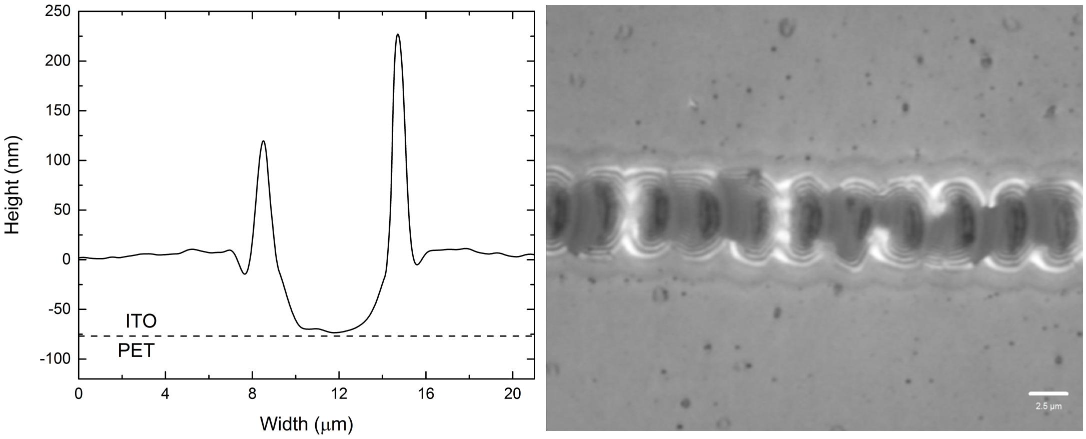

(a)

(b)

Figure 6.2: (a) Ablation profile of single pulse ablation at $\lambda = 360$ nm and $60\,\mathrm{mJ\,cm^{-2}}$. The ablation shows complete removal of the ITO layer and negligible damage to the PET substrate below. The bulges are higher than 200 nm. (b) Laser-written line in ITO on PET at $\lambda = 360$ nm and $53\,\mathrm{mJ\,cm^{-2}}$ and a pulse overlap of 66%. The PET shows visible damage (black spots) due to the similar threshold fluences of both materials.

Laser structuring at λ=410 nm

Laser structuring was performed at $\lambda = 410$ nm. A fluence $F = 200\,\mathrm{mJ\,cm^{-2}}$ was tested. This fluence is slightly higher than the threshold fluence $F_{\mathrm{th}} = 170\,\mathrm{mJ\,cm^{-2}}$ of ITO but lower than the one of PET, $F_{\mathrm{th}} = 240\,\mathrm{mJ\,cm^{-2}}$, at the given wavelength. Figure 6.3a shows a confocal 3D image of a laser-written line with a pulse overlap of 69%. Selective ablation was performed with no visible damage to the PET substrate below. However, the height of the bulges is ≥ 250 nm. This is confirmed on the profile image of the selected line (Figure 6.3b). The high bulges may lead to shorts with the top electrode. The laser-written line width is < 5 µm.

The pulse overlap was increased to 85%, to evaluate the effect on the bulges keeping the fluence constant at $F = 200\,\mathrm{mJ\,cm^{-2}}$. Figure 6.3c shows a confocal 3D image of the resulting laser-written line. The highest bulge is around 100 nm showing a significant improvement when compared to the lower pulse overlap. However, the higher pulse overlap led to damage of the PET substrate below as shown by the dark spots that go below 250 nm.

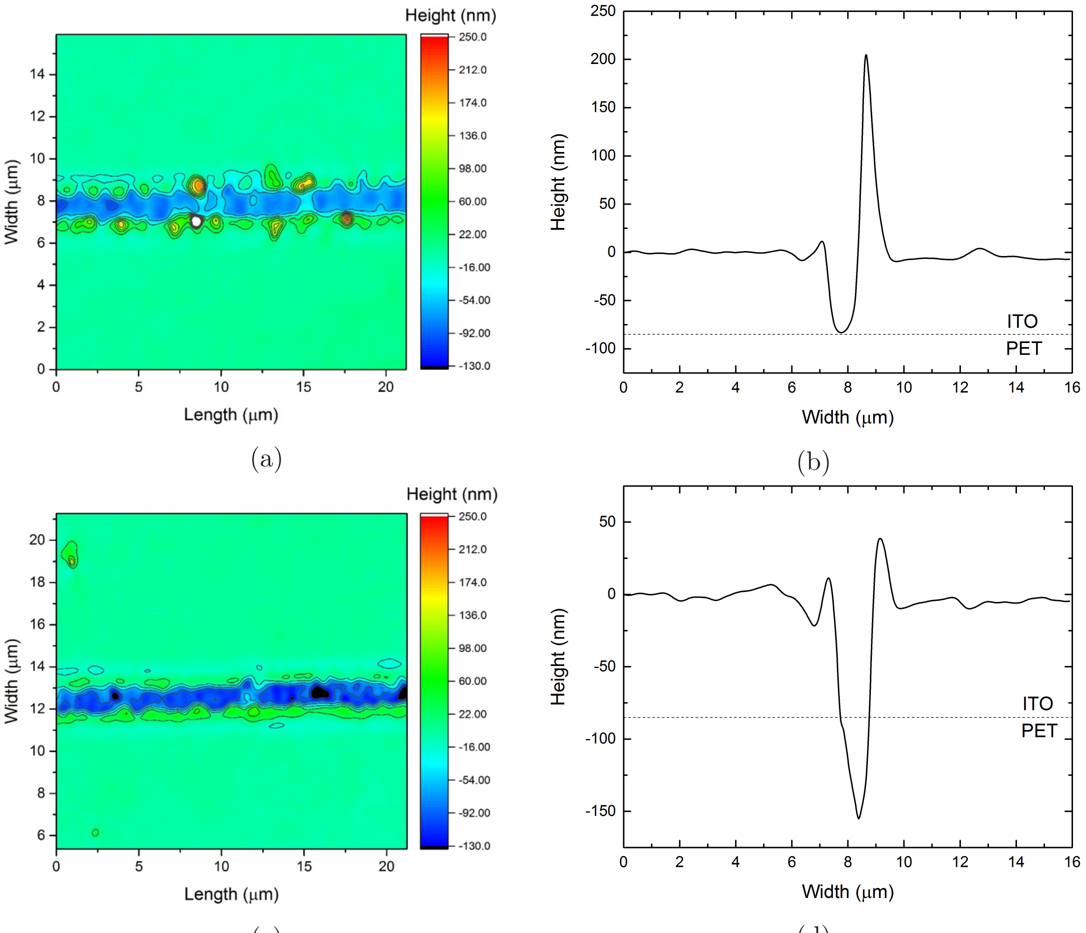

(a)

(b)

(c)

(d)

Figure 6.3: Comparison between laser-written lines at $\lambda = 410$ nm with different pulse overlaps. (a) and (b) show the 3D image and confocal profile of a laser-written line with a pulse overlap of 69%. The laser-written line shows selective ablation with negligible damage to the PET substrate below. However, the bulges are higher than 200 nm as shown in the profile picture (b). (c) and (d) show the 3D image and confocal profile when the pulse overlap is increased to 85%. The bulges improve around 100 nm (confocal profile (d)). However, the substrate shows damage due to the higher pulsed overlap. Both lines were structured with a $F = 200\,\mathrm{mJ\,cm^{-2}}$ and have a laser-written line width of ≤ 5 µm.

There is no significant increase on the laser-written line width as it remained ≤ 5 µm (Figure 6.3d). The damage may be created due to an incubation effect created by the higher pulse overlap. The incubation effect enhances the absorption of the PET.

Laser structuring at λ=550 nm

Due to the increment on the PET threshold fluence to $F_{\mathrm{th}} = 427\,\mathrm{mJ\,cm^{-2}}$, the working window becomes larger at $\lambda = 550\,\mathrm{nm}$ than at $\lambda = 410\,\mathrm{nm}$. Hence a higher fluence was chosen $F = 280\,\mathrm{mJ\,cm^{-2}}$ to evaluate the laser-written lines at $\lambda = 550\,\mathrm{nm}$. Using a pulse overlap of 72%, selective ablation was achieved, however, the observed bulges were higher than 200 nm. Following the observations at $\lambda = 410\,\mathrm{nm}$ where the increase in pulse overlap led to lower bulges, the pulse overlap was increased to 89% at $\lambda = 550\,\mathrm{nm}$. The laser-written lines exhibit selective ablation, with negligible damage to the PET substrate. The bulges are reduced to approximately 100 nm. The width of the laser-written lines is < 5 µm (Figure 6.4).

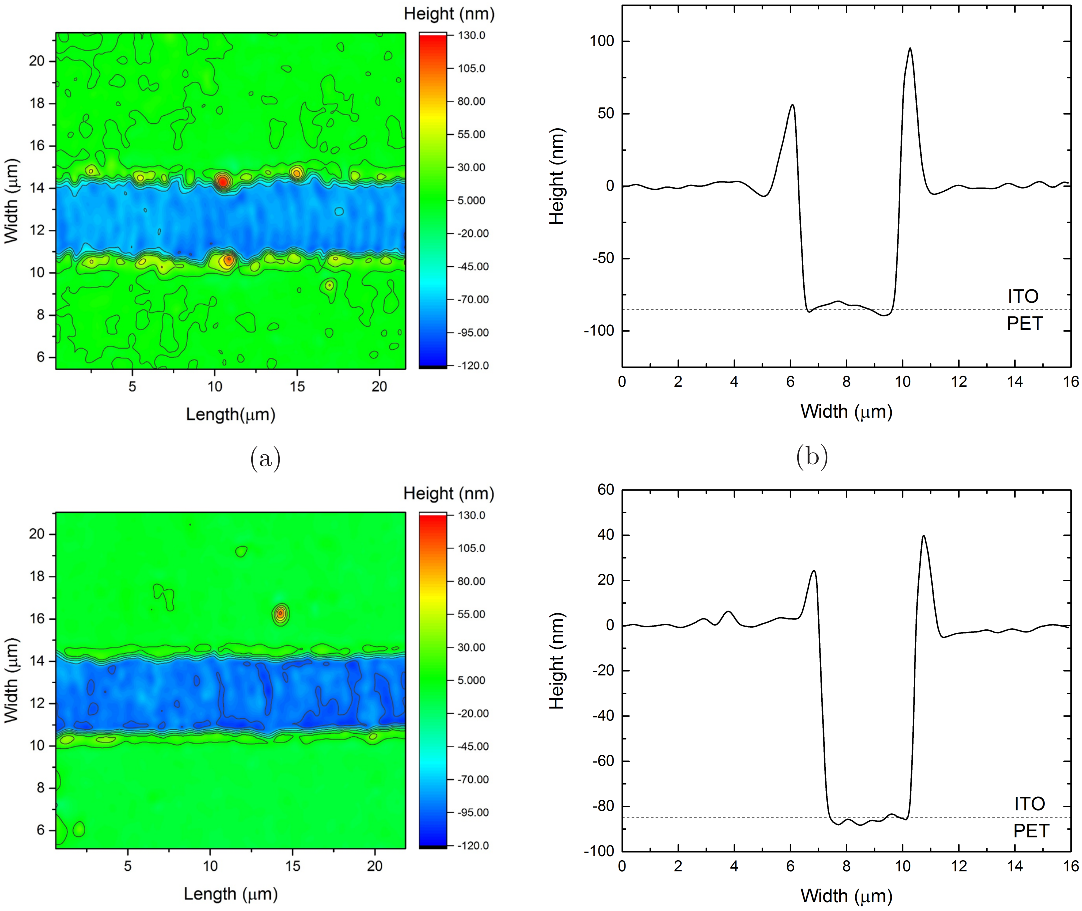

(a) (b)

(c) (d)

Figure 6.4: Comparison between laser-written lines at $\lambda = 550\,\mathrm{nm}$ with different pulse overlaps. (a) and (b) show the 3D image and confocal profile of a laser-writtend line with a pulse overlap of 89%. The laser-written line shows selective ablation with negligible damage to the PET substrate below. The bulges are around 100 nm as shown in the profile picture (b). (c) and (d) show the 3D image and confocal profile when the pulse overlap is increased to 95%. The bulges improve to ≤ 50 nm (confocal profile (d)). Selective ablation is achieved with negligible damage to the PET substrate below. Both lines were structured with a $F = 280\,\mathrm{mJ\,cm^{-2}}$ and have a laser-written line width of ≤5 µm.

Similar to the case with $\lambda = 410\,\mathrm{nm}$, a higher pulse overlap of 95% for $\lambda = 550\,\mathrm{nm}$ was evaluated, keeping the fluence constant at $F = 280\,\mathrm{mJ\,cm^{-2}}$. Figure 6.4c depicts selective ablation with negligible damage to the PET substrate. The bulge height is further decreased to $\leq 50\,\mathrm{nm}$. The largest operating window at $\lambda = 550\,\mathrm{nm}$ provides the opportunity to increase the pulse overlap to 95% without damaging the PET substrate below. The confocal profile image (Figure 6.4d) of the ablation confirms the negligible damage to the PET substrate. The width of the laser-written lines is $< 5\,\mathrm{\mu m}$.

Laser structuring at λ=650 nm

At $\lambda = 650\,\mathrm{nm}$, the working window is similar to the one at $\lambda = 550\,\mathrm{nm}$ as the threshold fluence of $\lambda = 650\,\mathrm{nm}$ of PET is $F_{\mathrm{th}} = 430\,\mathrm{mJ\,cm^{-2}}$. A lower fluence $F = 240\,\mathrm{mJ\,cm^{-2}}$ was evaluated. Figure 6.5a shows a confocal 3D image of a laser-written line using a pulse overlap of 90 %.

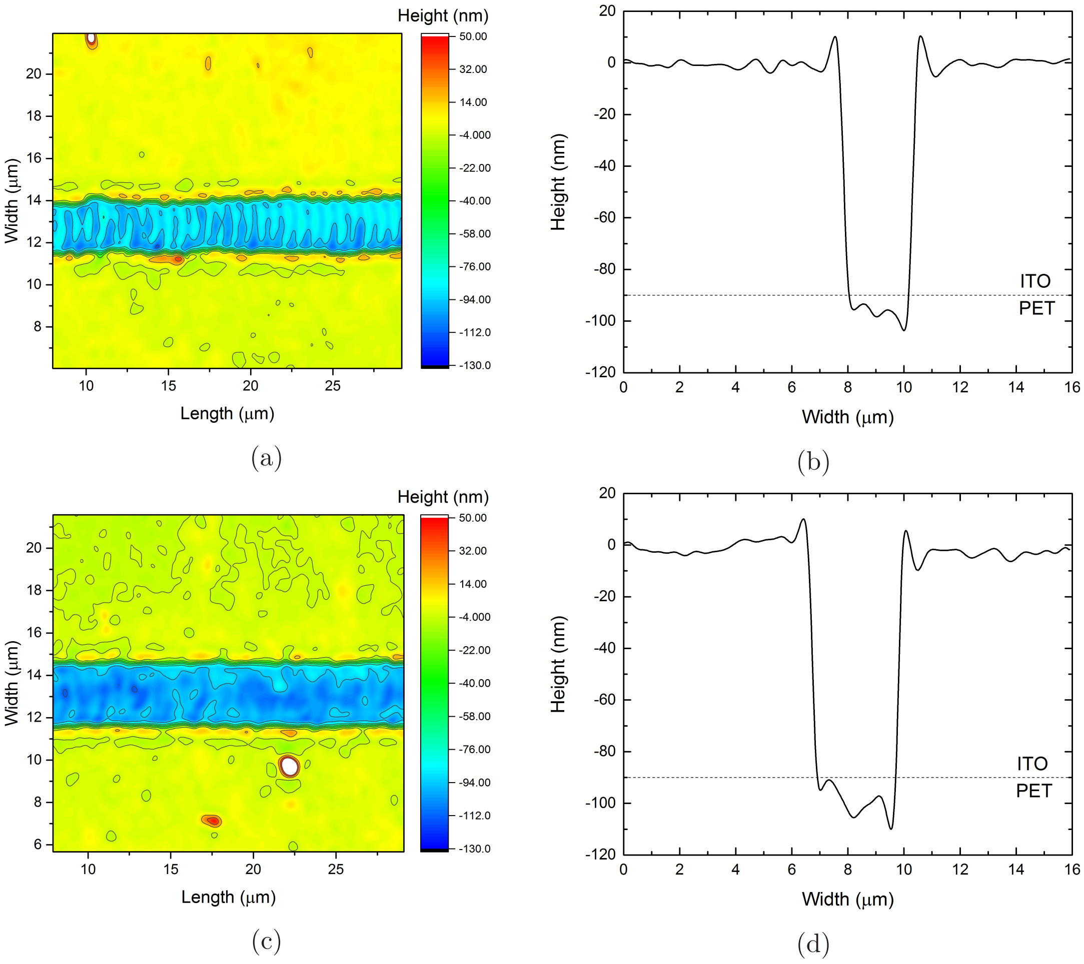

Figure 6.5: Comparison between laser-written lines at $\lambda = 650\,\mathrm{nm}$ with different pulse overlaps. (a) and (b) show the 3D image and confocal profile of a laser-written line with a pulse overlap of 90%. The laser-written line shows selective ablation with little damage to the PET substrate below. The bulges are around 50 nm as shown in the profile picture (b).(c) and (d) show the 3D image and confocal profile when the pulse overlap is increased to 95%. The bulges remain consistent around 50 nm (confocal profile (d)). Slight damage, in the order of 20 nm, is visible. Both lines were structured with a $F = 240\,\mathrm{mJ\,cm^{-2}}$ and have a laser-written line width of $\leq 5\,\mathrm{\mu m}$.

The laser ablation did only little damage to the PET substrate and bulge height ≤ 50 nm. The confocal profile image (Figure 6.5b) confirms the slight damage to the PET substrate and the low bulge height. The width of the laser-written lines is ≤4 µm.
Similar to the ablation with $\lambda = 550\,\text{nm}$, the larger operating window allows to increase the pulse overlap causing little damage to the PET substrate below. A pulse overlap of 95 % was evaluated keeping the fluence at $F = 240\,\text{mJ}\,\text{cm}^{-2}$. Figure 6.5c shows the 3D confocal image of the laser-written line. The PET substrate shows little damage, with a bulge height of ≤50 nm. The width of the laser written-line is < 5 µm (Figure 6.5d).

Laser structuring at λ=700 nm

At $\lambda = 700\,\text{nm}$, the working window becomes the largest as the threshold fluence for PET is the highest at $F_{\text{th}} = 470\,\text{mJ}\,\text{cm}^{-2}$ compared to the threshold fluence of ITO $F_{\text{th}} = 170\,\text{mJ}\,\text{cm}^{-2}$. A fluence $F = 250\,\text{mJ}\,\text{cm}^{-2}$ was evaluated. Figure 6.6a shows the laser-written line with a

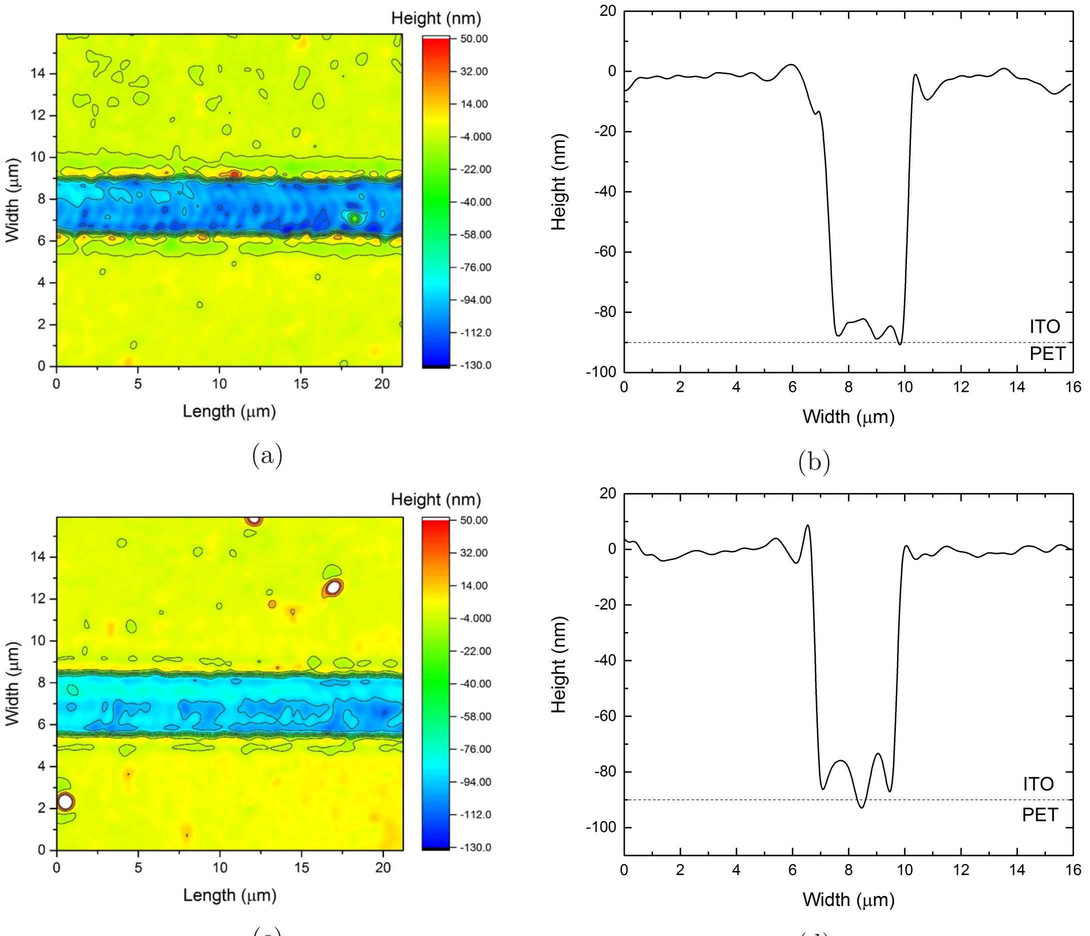

(a) (b)

(c) (d)

Figure 6.6: Comparison between laser-written lines at $\lambda = 700\,\text{nm}$ with different pulse overlaps. (a) and (b) show the 3D image and confocal profile of a laser-written line with a pulse overlap of 90%. The laser-written line shows selective ablation with little damage to the PET substrate below. The bulges are below 50 nm as shown in the profile picture (b).(c) and (d) show the 3D image and confocal profile when the pulse overlap is increased to 95%. The bulges remain below 50 nm (confocal profile (d)). Slight damage is visible on the PET substrate. Both lines were structured with a $F = 250\,\text{mJ}\,\text{cm}^{-2}$ and have a laser-written line width of ≤5 µm.

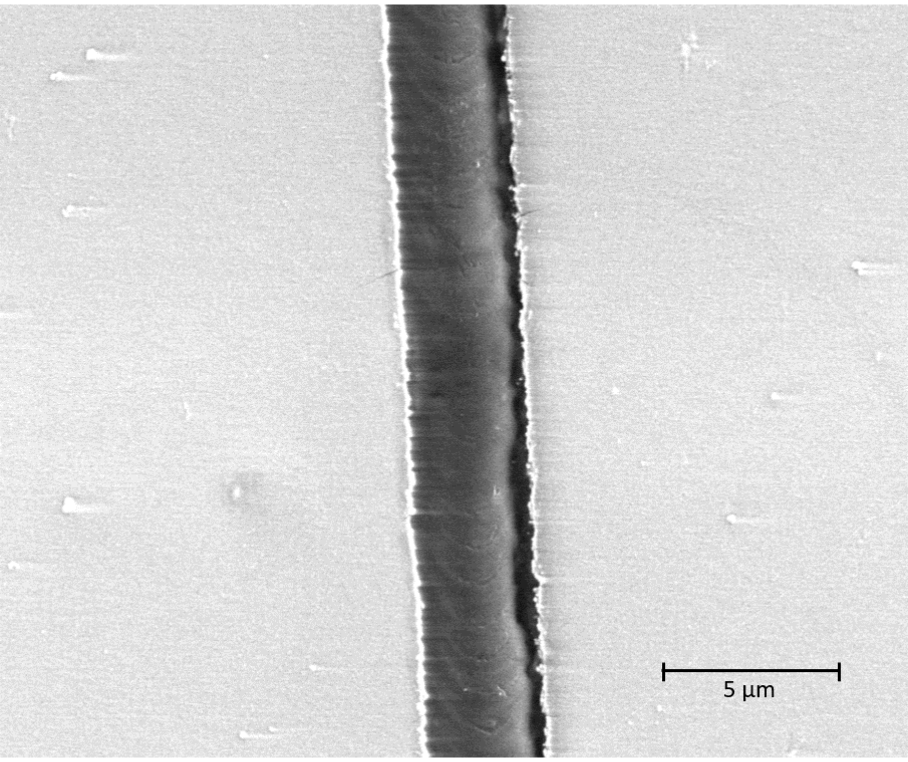

Figure 6.7: SEM image of the laser-written line at $\lambda = 700\,\mathrm{nm}$, $F = 250\,\mathrm{mJ\,cm^{-2}}$ and a pulse overlap of 95%. The damage on the PET substrate is negligible, with small visible lines in the overlapping area of the pulses.

pulse overlap of 89%. Selective ablation was attained on the laser-written line with negligible damage to the PET substrate below. The bulge height is $\leq 50\,\mathrm{nm}$. The profile image(Figure 6.6b) shows selective ablation with negligible damage caused to the PET substrate. The width of the laser-written line is $< 5\,\mu\mathrm{m}$.

The pulse overlap was again increased to 95%. Figure 6.6c shows the confocal 3D image with little damage to the PET substrate and low bulge height $\leq 50\,\mathrm{nm}$. The profile image (Figure 6.6d) exhibits slight damage to the PET. The bumps are due to slight melting of the PET. The line width is $\leq 5\,\mu\mathrm{m}$. The SEM image (Figure 6.7) confirms the slight damage to the PET layer below. Small, lines show the overlap of the pulses. However, this damage is negligible and does not affect the mechanical properties of the PET. The laser-written line width is confirmed to be $< 5\,\mu\mathrm{m}$.

6.3 Discussion

The threshold fluences F_{th}, for both ITO and PET at eight different wavelengths, covering the whole visible spectrum, were determined. A relationship between the threshold fluence of ITO and its absorption spectrum was observed, such that the linear absorption plays an important role on the ultrashort pulse ablation of ITO. In contrast, the threshold fluences of PET show a linear dependency with the wavelength. The threshold fluences of PET follow the prediction of equation 5.9. They do not follow the absorption spectrum of PET as its magnitude is mostly constant between $\lambda = 450\,\mathrm{nm}$ and $\lambda = 700\,\mathrm{nm}$. Equation 5.9 was determined using the assumption of a bulk material and surface processes on the skin layer. This results could help further theoretical work to explain the interaction of femtosecond lasers with thin films at different wavelengths.

Here, femtosecond laser structuring allowed to selectively structure ITO on top of PET with low bulges ≤ 50 nm and slight damage to the ITO substrate below at three different wavelengths $\lambda = 550\,\mathrm{nm}$, $\lambda = 650\,\mathrm{nm}$ and $\lambda = 700\,\mathrm{nm}$. At $\lambda = 410\,\mathrm{nm}$, selective ablation was achieved, however high bulges $\geq 200\,\mathrm{nm}$ were still produced. In all the evaluated wavelengths, the bulge height decreased with higher pulse overlaps. Therefore, a large working window is important as it allows a higher pulse overlap without damaging the layer below as it was demonstrated in this work. The laser-written line widths were in all cases $< 5\,\mu\mathrm{m}$. The line width is below the waist W_0 of the objectives. This demonstrate that femtosecond laser can successfully achieved high precision under the waist of the focused beam. The small line width will lead to smaller inactive areas on monolithically connected devices like OLEDs or OPVs modules. The best results were demonstrated at $\lambda = 700\,\mathrm{nm}$, $F = 250\,\mathrm{mJ\,cm^{-2}}$ and pulse overlap of 95%. The low bulges will allow the construction of thin-film devices on top of the ITO layer without shunts that decrease their performance. The selective ablation will allow the use of PET substrates for applications that require mechanical flexibility.

7 OLED modules structured by femtosecond laser ablation

OLEDs are rapidly becoming a new tendency on displays and luminaries. Several companies use them on mobile phones and flat screen TVs. For illumination large display areas are required. However, large areas come with detriment of the light homogeneity due to voltage losses.[42] *The voltage losses are caused by the high sheet resistance of the transparent electrodes, typically ITO. The problem increases when the OLED area increases as the driving current of the OLED depends on the size of the device. The most common concept to solve this issue is to use of metal bus bars that improve the conductivity.*[44,45,84–86] *However, the bus bars are visible reducing its appeal. The bus bars have a typical height of 300 - 500 nm, which exceeds the common thickness of the light emitting layers, that is, ≤100 nm. This can lead to shorts, and passivisation layers are necessary to solve this problem. A different approach is to monolithically connect the OLEDs into a large-scale module. The operating current then is limited by the smaller area of each individual OLED. This concept has been proven by Dugal et al.*[52]

In this chapter, femtosecond laser structured OLED modules are described. In section 7.1 the used materials, the architecture and the device design of the OLED module are described. In section 7.2 the threshold fluences were calculated for 5 different wavelengths $\lambda = 550\,\text{nm}$, $\lambda = 600\,\text{nm}$, $\lambda = 650\,\text{nm}$, $\lambda = 700\,\text{nm}$ *and* $\lambda = 750\,\text{nm}$. *Section 7.3 presents the optimized process to structure process P1, P2 and P3 for two different wavelengths* $\lambda = 550\,\text{nm}$ *and* $\lambda = 700\,\text{nm}$. *Section 7.4 describes the optoelectronic characterization of the devices. Section 7.5 gives our conclusions. Parts of this section are reprinted and adapted from Fragoso et al.*[87]

7.1 Materials, device design and architecture

7.1.1 Materials

The materials used for the OLEDs need to comply with several specifications. Besides the electronic requirements necessary to bring the free carriers into the device, the processibility of the materials is crucial to fabricate the devices. For the electron injection layer (EIL) and the emitting layer the feasibility to process the material from solution is necessary. For the hole injection layer (HIL) and the metal electrodes vacuum evaporation of the materials is required.

Zinc oxide

Zinc oxide (ZnO) is a transition metal oxide that has high electron mobility, wide band gap (3.3 eV) and low work function (4.2 eV).[88] Due to its electronic properties, it is used as electron injection and transport layer. It is also a material with low reactivity, leading to better stability on the devices.[88,89] In this experiments the layers were produced from a nanoparticle dispersion (N10, Avantama Ag. 0.55 wt% in isopropanol). After deposition of the layers the samples were annealed under nitrogen atmosphere on a hotplate (150°, 10 min).[90]

Polyethylenimine (PEI)

PEI is used to modify the work function of ZnO and facilitate the injection of electrons.[91] An ultrathin layer (1 to 10 nm) is applied on top of the ZnO layer. The work function is modified due to the ethylamine dipole within the self assembled monolayer (SAM) and the dipole between the SAM and the ZnO layer. The PEI layer is spincoated from a 2-methoxyethanol solution (0.4 wt%). After the application the samples were washed in ethanol and annealed under ambient atmosphere on a hotplate (100°C, 10 min). The work function of the bilayer (ZnO/PEI) is 3.3 eV.[90]

SuperYellow

SuperYellow is a yellow emitting polymer (Merck KGaA). The color of the emitted light in CIE 1931 XYZ color space is shown in Figure 7.1a.[92] SuperYellow has a HOMO level of -5.4 eV and LUMO level of -3.0 eV, resulting in a band gap of 2.4 eV. The molecular structure of SuperYellow is shown in figure 7.1b.

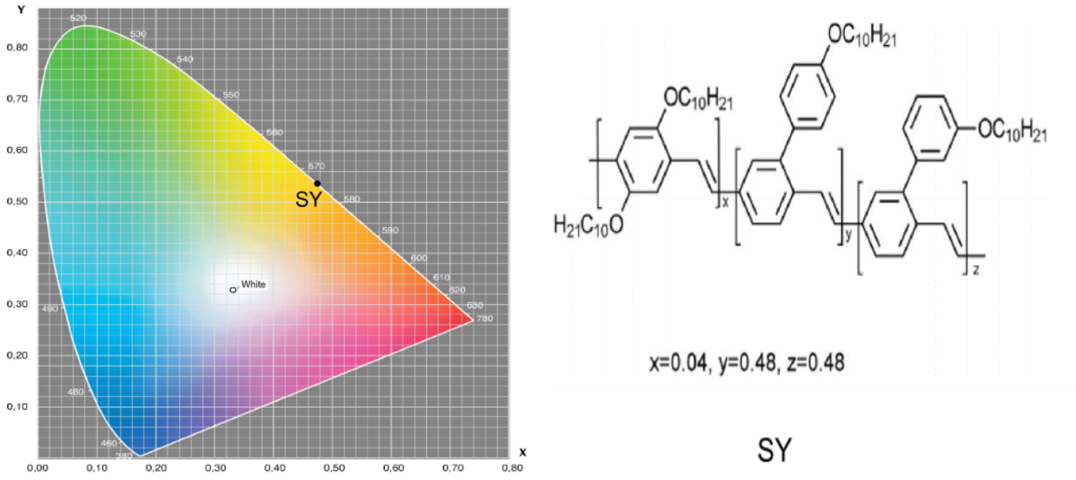

(a)

(b)

Figure 7.1: (a) SuperYellow emission in the CIE 1931 XYZ color space. (b) Molecular structure of SuperYellow.[92]

Molybdenum trioxide (MoO_3)

Molybdenum trioxide was used as HIL. A 10 nm layer was evaporated in high vacuum for this work. The work function of the MoO_3 layer is -5.9 eV. MoO_3 has been previously used in OLEDs leading to stable devices as the HIL encapsulates the emitting layer.[93].

7.1.2 Architecture and sample design

Figure 7.2a depicts the architecture and layer thicknesses of the OLED modules. ITO is used as bottom electrode. ZnO/PEI is the electron injection layer and SuperYellow is the emitting layer. MoO_3 is the hole injection layer and silver is the top electrode.

The individual OLEDs are connected in a module by structuring ITO as P1 to electrically isolate the bottom electrode. ZnO/PEI/SuperYellow is structured as P2 to permit the electrical connection between the OLEDs. MoO_3 and silver are structured as P3 to separate the top electrode.

The OLED module was designed on a 25 x 25 mm^2 ITO coated glass substrate (Figure 7.2b). The design permits the measurement of the individual OLEDs when two OLEDs per substrate are built. The total emitting area of the device is 1.625 cm^2. The ITO contact was laser structured twice, once for the P1 structuring step of the monolithic connection and once to isolate the top contact from the bottom electrode of the OLED B. The silver/MoO_3 top electrode was evaporated through a mask. The P3 step of the monolithic connection was structured using the laser on the silver.

7.2 Threshold fluence characterization

The threshold fluences were determined for five different wavelengths from $\lambda = 550$ nm to $\lambda = 750$ nm with 50 nm steps using the Liu method described in section 5.4. This range includes the wavelengths of the Ti:Sapphire laser and several commonly used green lasers. The ablation tests were done on proxy devices using the device architecture (figure 7.2a)

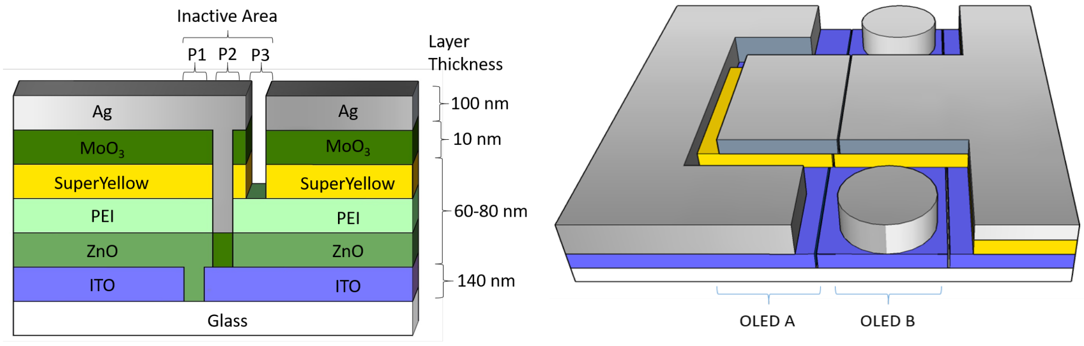

(a)

(b)

Figure 7.2: (a) OLED module architecture showing the P1, P2, P3 steps for the monolithic connection. (b) Sample design on a 25 x 25 mm^2 ITO coated glass substrate. The total emitting area of the device is 1.625 cm^2.

to consider the influence of the layers underneath. Single spots were attained by moving the µFAB stage at 180 mm s^{-1}. The calculated focused waist was $W_0 = 3.5\,\mu\text{m}$ at $\lambda = 750\,\text{nm}$.

Figure 7.3a shows the threshold fluences for the three materials ablated in steps P1, P2 and P3. The threshold of ITO ,$F_{\text{th}} = 170\,\text{mJ cm}^{-2}$, remains consistent during the whole wavelength range. SuperYellow threshold fluences, $F_{\text{th}} = 40\,\text{mJ cm}^{-2}$, also remain constant for all wavelengths. A similar tendency of the threshold fluences and the absorption is observed for both materials (figure 7.3b). The absorption spectra have a slight increase in absorption, however this is not significant and it is not reflected in the threshold fluences. The threshold fluences at different wavelengths do not follow equation 5.9 that expects a linear increase of the ablation threshold with the wavelength. It is possible that the difference stems from the thin-film nature of the layers.

Different to what was observed for ITO and ZnO/PEI/SuperYellow, the threshold fluence for MoO_3/Silver (P3) increases linearly with the wavelength, from $F_{\text{th}} = 230\,\text{mJ cm}^{-2}$ at $\lambda = 550\,\text{nm}$ to $F_{\text{th}} = 490\,\text{mJ cm}^{-2}$ at $\lambda = 750\,\text{nm}$ (Figure 7.3a). The decrease in absorption between $\lambda = 550\,\text{nm}$ and $\lambda = 750\,\text{nm}$ could partially explain the increase of the threshold fluence. However, this tendency follows equation 5.10 where a linear relationship between the wavelength and the threshold fluence is established. Although the MoO_3/Silver layer is also a thin-film, it is not semitransparent like ITO and ZnO/PEI/SuperYellow. This may explain the different tendencies for MoO_3/Silver, and ITO and ZnO/PEI/SuperYellow.

To facilitate the selective ablation of one layer on top of another it is important to have a working window, defined by the difference of the threshold fluences. Figure 7.3a clearly shows that for the selective ablation of ZnO/PEI/SuperYellow (P2) on top of ITO there is an equal working window for all the studied wavelengths. For the ablation of MoO_3/Silver (P3), the required fluence to structure P3 is higher than the one necessary to structure P1

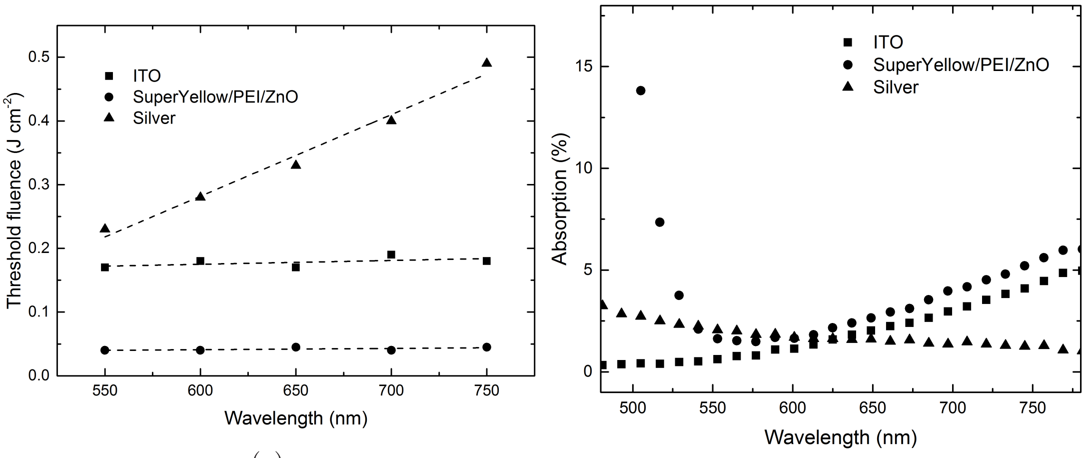

(a)

(b)

Figure 7.3: (a) Threshold fluence for ITO (P1), ZnO/PEI/SuperYellow (P2) and MoO_3 for five different wavelengths (b) absorption spectra for ITO (P1), ZnO/PEI/SuperYellow (P2) and MoO_3/silver (P3).

and P2. Therefore, the optimization of the pulse overlap is crucial to structure MoO_3/Silver (P3).

7.3 Structuring process optimization

In this section, line structuring with different wavelengths is explored. The lines are written by overlapping the pulses. The conditions are adjusted by changing the speed of the XYZ stage. An insufficient pulse overlap might lead to incomplete ablation, hence creating shorts or a high sheet resistance. An excessive ablation may lead to the damage of the layer below. The structuring requirements change depending on the ablation step. For ITO (P1), consistent lines are required (to achieve electrical insulation), with low bulges and small damage to the glass substrate below. For ZnO/PEI/SuperYellow (P2) selective ablation with a clean removal of the materials is the most important. Damage of the ITO below would hamper the performance or even prevent the operation of the device. If parts of the layers are not ablated, the series resistance of the device may increase, leading to lower efficiencies. Finally in the case of MoO_3/Silver (P3), it is most important not to damage the ITO layer below. The ZnO/PEI/SuperYello below can be damaged without affecting the device performance, however it is desirable to keep it as it functions as a buffer layer in case of melting of the silver top electrode during the ablation process. The melted silver may lead to shorts if it contacts the bottom electrode.
There is a constant working window for the structuring of P2 for all five studied wavelengths. The structuring processes were optimized for the two extreme cases, at $\lambda = 550\,\mathrm{nm}$ and at $\lambda = 750\,\mathrm{nm}$.

7.3.1 ITO structuring (P1)

Several fluences above the threshold fluence were tested to structure ITO (P1). The optimum parameters were $F = 370\,\mathrm{mJ\,cm^{-2}}$, pulse overlap of 86 % at $\lambda_1 = 550\,\mathrm{nm}$ and $F = 350\,\mathrm{mJ\,cm^{-2}}$,

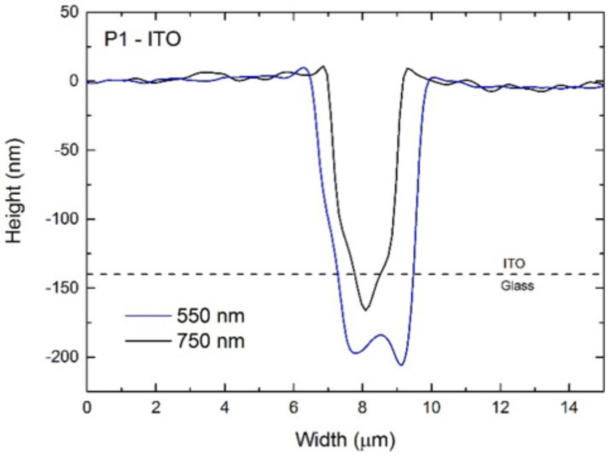

Figure 7.4: ITO structuring (P1) at $\lambda = 550\,\mathrm{nm}$ and $\lambda = 750\,\mathrm{nm}$. Slight damage to the glass substrate below is observed. The bulge is low, in the order of 20 nm, and the structured line width is ≤10 µm for both wavelenghts.

pulse overlap of 73 % at $\lambda_2 = 750$ nm. Both processes led to clean ablation with slight damage to the glass substrate below and electrical insulation. The slight damage on the glass substrate does not hamper the device performance. The bulge is low in the order of 20 nm and the line width is < 10 µm allowing small inactive areas. The ablation processes at both wavelengths led to electrical insulation. Figure 7.4 depicts the confocal profile for the ablation processes at both wavelengths.

7.3.2 ZnO/PEI/SuperYellow structuring (P2)

Several fluences within the operating window were tested to structure ZnO/PEI/SuperYellow (P2). The optimum parameters were $F = 110\,\text{mJ cm}^{-2}$, pulse overlap of 85 % at $\lambda_1 = 550$ nm and $F = 240\,\text{mJ cm}^{-2}$, pulse overlap of 86 % at $\lambda_2 = 750$ nm. Similar to the case for the ITO, the laser-written lines have a width of < 10 µm. The structuring process at $\lambda_2 = 750$ nm requires a higher fluence to fully remove the ZnO layer below and to allow a direct connection between the silver and the ITO. Figure 7.5a shows the confocal profile pictures of the laser-written lines, where nice selective ablation is achieved as no visible damage to the ITO layer is shown. This is further confirmed in figure 7.5b where the SEM picture shows the monolithic connection between the silver and the ITO layers with negligible damage to the ITO layer. The bulges are higher than 80 nm, however, they do not play a significant role on the P2 ablation. In both cases, the relative high pulse overlap is necessary to remove the ZnO layer without any residues and to allow a good connection between the ITO and the silver layers.

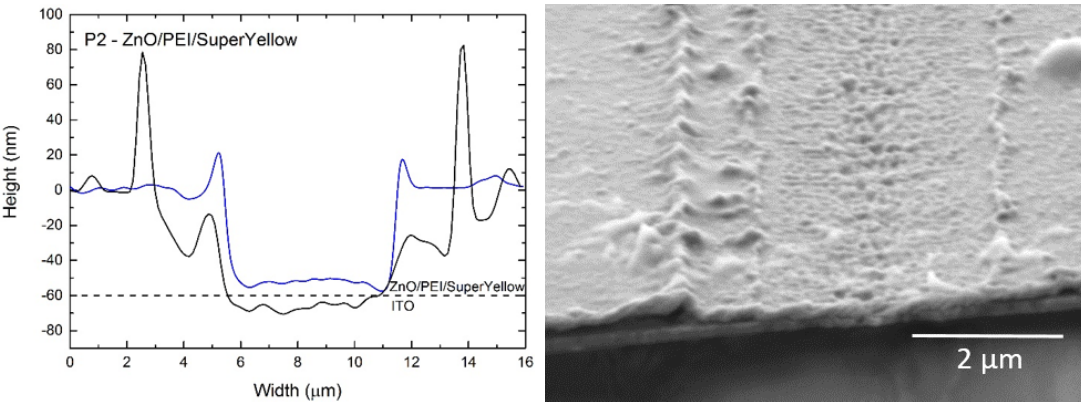

(a) (b)

Figure 7.5: (a) Confocal profile image of the laser-written lines of the ZnO/PEI/SuperYellow (P2) using $\lambda = 550$ nm and $\lambda = 750$ nm. Negligible damage to the ITO electrode below is visible. Bulges are present, however, they are not detrimental to the performance of the device. (b) SEM image showing the ablation of ZnO/PEI/SuperYellow (P2) at $\lambda = 750$ nm. The monolithic connection, between the silver and the ITO, is visible. The ITO shows negligible damage on the spot where the ablation took place.

7.3.3 MoO_3/silver (P3) structuring

Several fluences above the silver threshold fluence were tested to structure MoO_3/silver (P3). The optimum parameters were $F = 340\,\mathrm{mJ\,cm^{-2}}$, pulse overlap of 65% at $\lambda_1 = 550\,\mathrm{nm}$ and $F = 540\,\mathrm{mJ\,cm^{-2}}$, pulse overlap of 66% at $\lambda_2 = 750\,\mathrm{nm}$. The higher fluence used at $\lambda_2 = 750\,\mathrm{nm}$ reflects the higher threshold fluence. Figure 7.6a shows the confocal profile image of the laser-written lines using both wavelengths. At $\lambda_1 = 550\,\mathrm{nm}$, the ablation depth (140 nm) shows slight damage to the ZnO/PEI/SuperYellow layers underneath. However, this minor damage does not hamper the functionality of the device as the ITO is unscathed. Although a higher fluence was used at $\lambda_2 = 750\,\mathrm{nm}$, similar results to the ones observed at $\lambda_1 = 550\,\mathrm{nm}$ are present, with slight damage to the ZnO/PEI/SuperYellow layers underneath and no visible damage to the ITO layer underneath. The bulges are higher than 200 nm, however, as there are no layers on top of P3, this does not affect the performance of the device. Figure 7.6b shows the SEM image of the P3 structured line at $\lambda_2 = 750\,\mathrm{nm}$. The low contrast SuperYellow looks blacked. In the regions where the pulse overlapped, damage to the ZnO/PEI/SuperYellow is present. However, the image confirms that the ITO (false-colored) is intact. An increase on the pulse overlap to 89% leads to complete removal of the ITO layer, hence preventing the operation of the devices.

7.4 Optoelectronic characterization

Following the optimization of the structuring processes for P1, P2 and P3, single OLEDs as well as two and three OLED modules were built. Each OLED module has an active area of $1.625\,\mathrm{cm}^2$. For the OLED modules, this area was divided in two or three parts. As depicted in figure 7.2a, the area defined by the width between P1 and P3 is inactive and hence not emissive. Figure 7.7a shows the confocal 3D profile image of a representative P1, P2 and P3

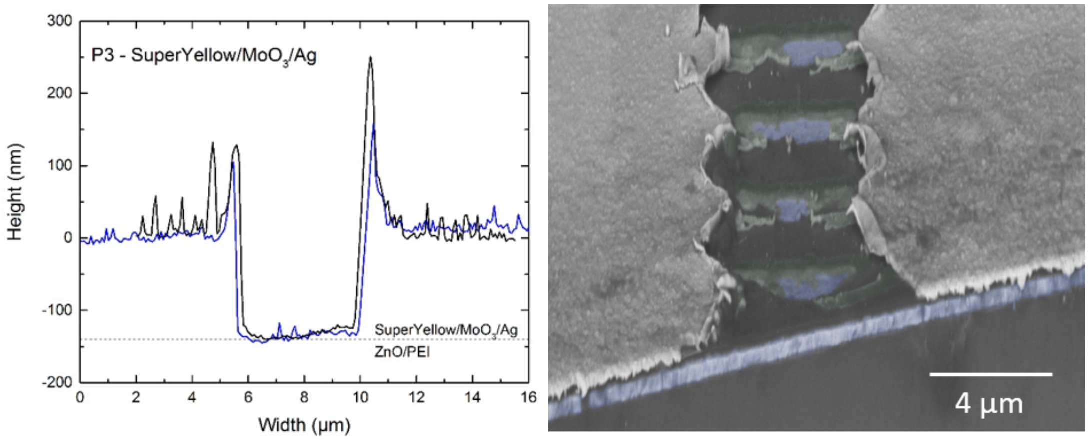

(a)

(b)

Figure 7.6: (a) Confocal profile image of the laser-written lines of MoO_3/silver (P3) at $\lambda = 550\,\mathrm{nm}$ and at $\lambda = 750\,\mathrm{nm}$. Negligible damage to the ITO electrode below is visible. The ablation depth shows damage to the ZnO/PEI/SuperYellow layers underneath. (b) SEM image showing the ablation of MoO_3/silver (P3) at $\lambda = 750\,\mathrm{nm}$. The low contrast SuperYellow appears black on the image. The ZnO/PEI/SuperYellow is damaged where the pulses overlap. The ITO appears unscathed.

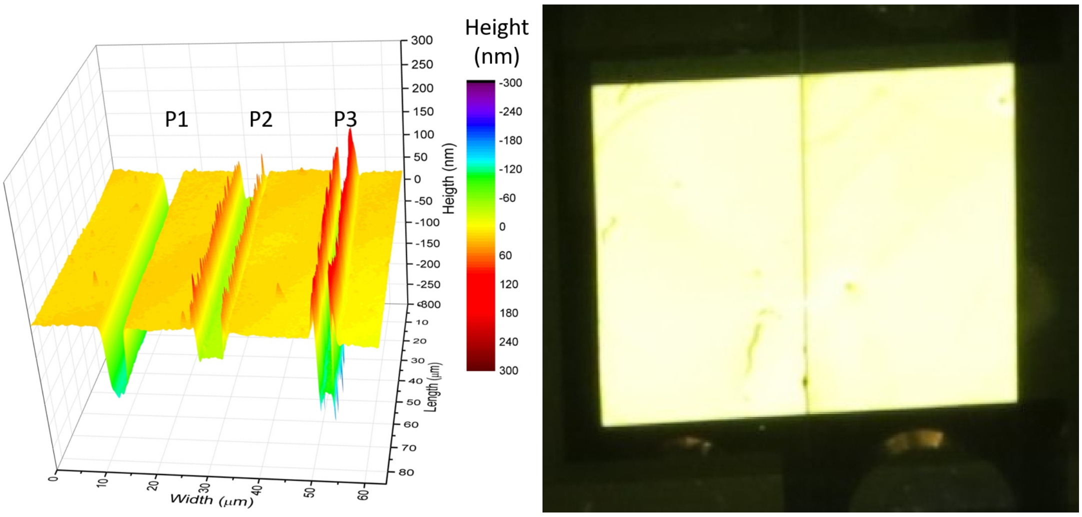

(a) (b)

Figure 7.7: (a) Confocal 3D profile image of the P1, P3 and P3 laser-written lines. The inactive area is confined within 45 µm. (b) Camera image of the lit OLED module. At larger distances and higher luminance the inactive area is concealed by the emitted light.

structuring forming a monolithic connection. The laser-written line widths of P1, P2 and P3 were all well below 10 µm, therefore the inactive width was confined within 45 µm, achieving a GFF = 99.6 %. The 45 µm structures are invisible to the human eye from a distance larger than 20 cm. Therefore, this type of monolithic connection is suitable for large-area lighting applications. Figure 7.7b shows a close up image of the two OLED mode at low luminance. The dark lines shows the monolithic connection.

Notably, for laser structured OPV modules, a GFF = 99.6% does not represent a significant improvement over a GFF = 98.5% found in literature[94]. However, for OLEDs, the reduction in the inactive area plays an important role in the concealment of it. The reported inactive area width for a GFF = 98.5% is 80 µm which is almost twice the 45 µm achieved during our work, making it visible at larger distances.

Figure 7.8a shows the onset voltages (V_{on}) of the different devices. V_{on} increases linearly with the number of serially connected OLEDs. The increase on the voltage compensates for the decrease of the current for the whole device. The V_{on} for the single device was $V_{\mathrm{on1}} = 2.7\,\mathrm{V}$, for the two OLED module $V_{\mathrm{on2}} = 5.2\,\mathrm{V}$ and for the three OLED module $V_{\mathrm{on3}} = 7.0\,\mathrm{V}$. The onset voltages were determined at a luminance $\mathrm{L} = 10\,\mathrm{cd\,m^{-2}}$. The observed linear increase further demonstrates the electrically working monolithic connection. The small deviations in the linearity of the device stem from some small discrepancies during the manufacturing process.

In a similar way the J-V curves demonstrate the working monolithic connections, as the voltage at a certain current density level increases linearly with the number of serially connected OLEDs. Figure 7.8a shows the J-V curves for the different devices. The voltages, measured at $J = 0.1\,\mathrm{mA\,cm^{-2}}$, are for the single device $V_1 = 2.3\,\mathrm{V}$, for the two OLED module $V_2 = 4.7\,\mathrm{V}$ and for the three OLED module $V_3 = 7.0\,\mathrm{V}$. Similar to the case of the V_{on}, the small deviations can be attributed to small discrepancies during the manufacturing process.

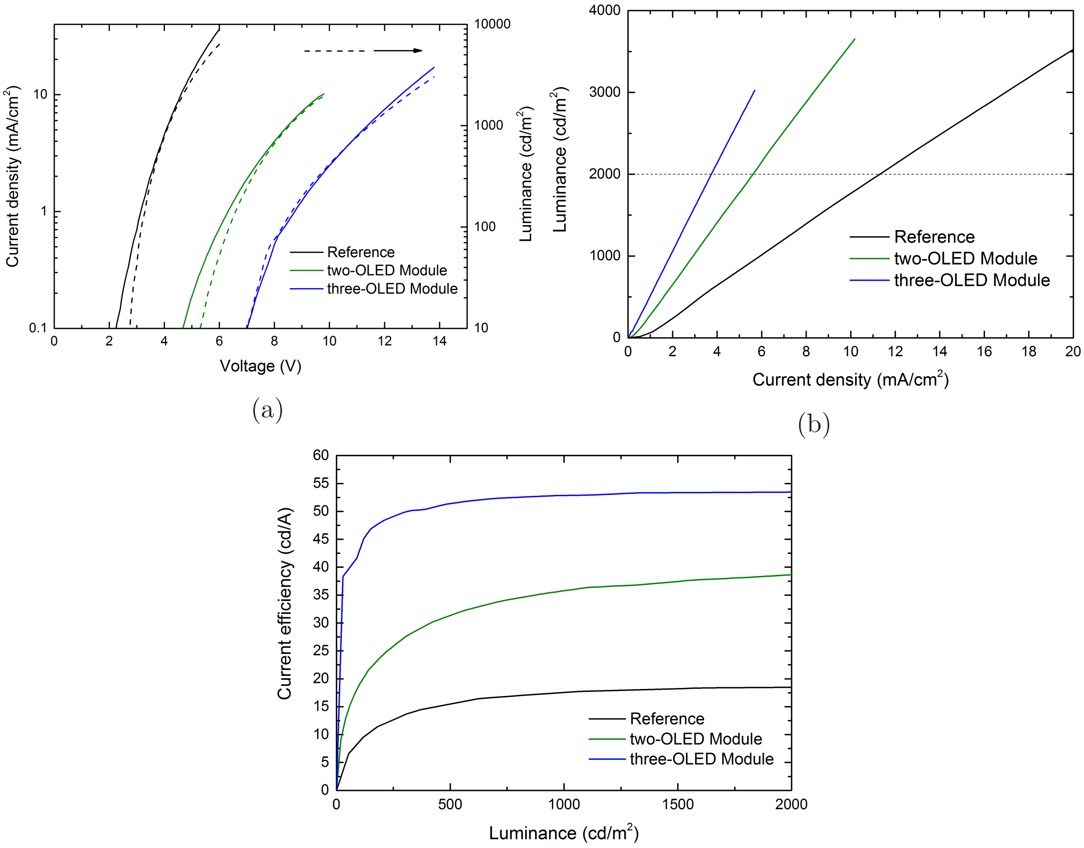

(a)

(b)

(c)

Figure 7.8: (a) JVL curves of the single OLED, two-OLED module and three-OLED module. Both the luminance and the onset voltages show a linear increase with the number of devices connected in series. (b) Luminance versus current density for the different devices. The current density decreases linearly for a given luminance with the number of devices connected in series. (c) Current efficiency of the single OLED reference, two-OLED and three-OLED module. The current efficiency increases linearly with the number of devices connected in series.

The luminance L against the current density also shows the desired effect of reducing the current for the OLED modules. For $L = 2000\,\mathrm{cd\,m^{-2}}$ (dotted line) the single OLED requires a $J = 11.4\,\mathrm{mA\,cm^{-2}}$, the two OLED module requires a $J = 5.7\,\mathrm{mA\,cm^{-2}}$ and the three OLED module requires a $J = 3.75\,\mathrm{mA\,cm^{-2}}$. As expected, the current density decreased linearly, similar to the linear increase for the voltage. This is shown in figure 7.8b.

An interesting parameter to measure is the current efficiency η_c. Figure 7.8c shows the current efficiencies of the different OLEDs. Similar to the V_on and the J-V curves, there is a linear increase of the current efficiency with the number of serially connected devices. η_c was measured at $L = 1000\,\mathrm{cd\,m^{-2}}$. For the single OLED reference device $\eta_{\mathrm{c}1} = 17\,\mathrm{cd\,A^{-1}}$. For the two and three-OLED modules, η_c increases to $\eta_{\mathrm{c}2} = 34\,\mathrm{cd\,A^{-1}}$ and $\eta_{\mathrm{c}3} = 53\,\mathrm{cd\,A^{-1}}$, respectively, demonstrating the linear increase of the current efficiency with the number of connected OLEDs.

A final interesting effect of the monolithically connected devices is the increase in the power efficiency (η). This is due to the dependance of the ohmic losses on the square of the current, $P_\mathrm{loss} = RI^2$. The power efficiency increases steadily for our devices with $\eta_1 = 12.5\,\mathrm{lm\,W^{-1}}$ for the single OLED reference. For the two and three-OLED modules $\eta_2 = 12.6\,\mathrm{lm\,W^{-1}}$ and

Table 7.1: Key performance parameters for the different single two and three OLED modules.

Device	V_{on} (at 10 cd m^{-2})	η_{c} (at 1000 cd m^{-2})	η(at 1000 cd m^{-2})
Reference	2.7 V	17 cd A^{-1}	12.5 lm W^{-1}
Two-OLED module	5.3 V	34 cd A^{-1}	12.6 lm W^{-1}
Three-OLED module	7.0 V	53 cd A^{-1}	14.0 lm W^{-1}

$\eta_1 = 14.0\,\text{lm}\,\text{W}^{-1}$ were achieved, again demonstrating the advantage of connecting the devices in series. Table 7.1 shows the key performance parameters of the different devices.

7.5 Discussion

Ultrashort pulsed laser structuring has been used to structure OLED modules. The study of the threshold fluence dependency on the wavelength shows that, for the semitransparent thin-films, the threshold fluences do not follow the equation 5.9 where a linear relationship between the threshold fluence and the wavelength is stated. However, this is not the case for the silver top electrode that shows linear increase with higher wavelengths as described in equation 5.10. This infers that, for thin semitransparent films, the linear absorption play a more important role than the non linear absorption. The results shown in this work could help to further understand the femtosecond ablation process with different wavelengths for thin-films.

It was demonstrated that it is feasible to structure P1, P2 and P3, for the described architecture (figure 7.2a), with both wavelengths $\lambda = 550\,\text{nm}$ and $\lambda = 750\,\text{nm}$. It is important to consider that selective ablation was achieved for the case of the silver, with damage on the SuperYellow underneath just on the overlapped area. With a more stable laser, where several non linear processes are not required to achieve the desired wavelength, it would be possible to achieve selective ablation by controlling the overlap and reducing it to a minimum. The presence of SuperYellow reduces the possibility of shunts between the top silver electrode and the bottom ITO electrode, reducing the number of failed devices. The possible reduction of failed devices is a key point for any production on an industrial scale.

The OLED modules show better optoelectronic characteristics than the single OLED reference devices as reflected by higher currents and power efficiencies. It is important to make further studies on the number of devices that may be connected in series. These studies have already been performed on OPV modules where a relationship between the number of devices, the width of the inactive area and the resistivity of the electrodes has been found.[95] The monolithic connection was demonstrated to work based on the increase of the onset voltages with the number of devices connected in series. Importantly. the reduced width of the inactive area that was achieved (≤45 µm) helps to conceal this non-emissive area and makes the laser a suitable tool to process large-area OLEDs for lighting applications.

A final interesting study to be performed in the future is the monolithic connection of tandem OLEDs. This would lead to further decrease of the current, leading to higher current efficiencies and more stable devices. The reduced current will also translate into a higher power efficiency that is an important selling point for luminaires.

Finally, it can be concluded that lasers are a suitable tool for industrial processes. In the ablation processes discussed herein, just a minimal fraction of the laser power was used. Therefore, the splitting of the beam for parallel ablation of several lines is possible. Also the developments of new femtosecond lasers with repetition rates in the range of hundreds of KHz or even MHz will allow the fast processing in roll-to-roll devices with speeds as high as $1\,\mathrm{m\,s^{-1}}$.

8 Single-junction and tandem solar modules on top of ITO

Organic solar cells have reached PCEs above 13 % in small-scale devices with photoactive areas around 10 mm^2.[28] *When the device is scaled up, the sheet resistance of the semi-transparent electrode, typically ITO, hampers the performance of the device. To reduce this effect the device is separated into several small units. The units are then connected in series, effectively reducing the total current of the device and increasing the voltage. This is usually accomplished through a monolithic connection as explained in section 2.2. Mechanical methods can be used to structure the different steps. However, this leads to a large inactive area, decreasing the performance of the device. The use of ultrashort pulsed lasers has been demonstrated as a viable alternative to structure organic solar modules, reducing the inactive area and allowing selective ablation of the different layers.*

In this chapter, the structuring process to manufacture solar modules, using different light-harvesting materials, is described. Section 8.1 introduces the materials used to build the solar modules. In section 8.2 a single-junction solar minimodule with a photoactive area of 10.5 mm^2 is constructed. The single-junction solar minimodule uses Poly[N-9-heptadecanyl-2,7-carbazole-alt-5,5-(4,7-di-2-thienyl-2,1,3-benzothiadiazole)], Poly[[9-(1-octylnonyl)-9H-carbazole-2,7-diyl]-2,5-thiophenediyl-2,1,3-benzothiadiazole-4,7-diyl-2,5-thiophenediyl] (PCDTBT) as donor material and [6,6]-Phenyl C_{71} butyric acid methyl esther ($PC_{71}BM$) as acceptor to form the BHJ. Section 8.3 describes the structuring steps to manufacture single-junction modules using a nanoparticulate active layer. The nanoparticles are formed from Poly(3-hexylthiophene-2,5-diyl) (P3HT) as donor and indene-C60 bisadduct ($IC_{60}BA$) as acceptor. In section 8.4 the ablation of single-junction and tandem devices is explored. Both single-junction and tandem devices are manufactured using Poly(4,8-bis[(2-ethylhexyl)oxy]benzo[1,2-b:4,5-b]dithiophene-2,6-diyl3-fluoro-2-[(2-ethylhexyl)carbonyl]thieno[3,4-b]thiophenediyl) (PTB7) and $PC_{71}BM$ as acceptor to form the active layer. Section 8.5 introduces the use of the ultrashort pulsed laser as a tool to optimize the cell width of the manufactured solar modules. Section 8.5 was done together with Konstantin Glaser, who focused his work in the optimization and upscaling of tandem solar cells. Finally, section 8.6 concludes this chapter.

8.1 Materials

The materials that are used to build organic solar cells need to fulfill certain requirements regarding the deposition processes and electronic configuration. This is especially important for tandem devices, where two solar cells are deposited on top of each other. As they are deposited from solution, the application of the top solar cell may dissolve the layers underneath. Therefore, a solvent barrier is necessary. Here, a Poly(3,4-ethylendioxythiophen):poly (styrolsulfonate) (PEDOT:PSS) formulation was used as solvent barrier. Solution processing, via doctor blading or spincoating, is a must for the materials that form the BHJ. There is a wide range of materials that can be used as active layers in organic solar devices. In this section three different polymers (PCDTBT, P3HT and PTB7) were used. As acceptors, two different fullerenes, $PC_{71}BM$ and $IC_{60}BA$, were used. ZnO and MoO_3 (ETL and HTL) were previously described in section 7.1.

PCDTBT

PCDTBT is a carbazole based copolymer that was first reported in 2007.[96] The material has a relatively deep HOMO at -5.5 eV.[97] In combination with $PC_{71}BM$ as acceptor material the fabricated devices show a high $V_{\mathrm{oc}} = 900\,\mathrm{mV}$ and $\mathrm{PCE} = 7\%$.[97] PCDTBT devices have shown a lifetime close to 7 years which demonstrate its high stability.[98] The molecular structure is depicted in figure 8.1.

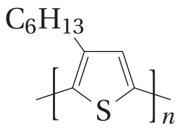

P3HT

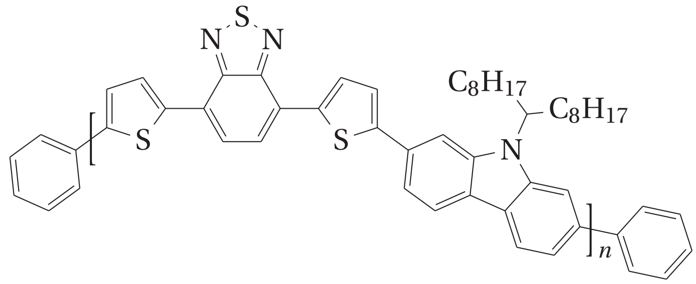

PCDTBT

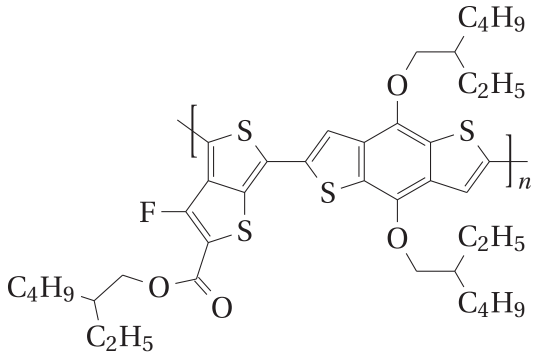

PTB7

Figure 8.1: Molecular structure of three different polymers (PCDTBT, P3HT and PTB7) used as electron donors in this work.

P3HT

P3HT is the most common used polymer material in organic solar cells; just in 2014 there were more than 1000 publications related to P3HT.[99] It has a low glass-transition temperature and it is highly crystalline. The HOMO of P3HT is at -5.0 eV and it has a relatively large bandgap (1.9 eV) limiting the current of the devices. When combined with $IC_{60}BA$, the devices can achieve a PCE of 6.5 % with high $V_{oc} = 830\,\mathrm{mV}$.[100] The molecular structure of P3HT is shown in figure 8.1.

PTB7

PTB7 is a commonly used material in organic solar cell research that was first published in 2009.[101] It has a HOMO of -5.15 eV and LUMO of -3.31 eV, resulting in a band gap of 1.84 eV. When combined with $PC_{71}BM$, it has demonstrated PCEs as high as 9.2 % with a $V_{oc} = 750\,\mathrm{mV}$.[102] The molecular structure is shown in figure 8.1.

$PC_{71}BM$

$PC_{71}BM$ is a fullerene derivative that was first reported in 2003.[103] It has a HOMO of -5.15 eV and LUMO of -3.31 eV, resulting in a band gap of 1.84 eV. It has the advantage over other fullerene derivatives that is not symmetric. Hence, it absorbs more light. Considering that the fullerene is a large fraction of the active layer, the enhanced light absorption permits a significant increase of the J_{sc}. The molecular structure is shown in figure 8.2.

$IC_{60}BA$

$IC_{60}BA$ is a fullerene derivative that was first reported in 2010.[104] It has a HOMO of -5.80 eV and a LUMO of -3.74 eV resulting in a band gap of 2.06 eV. The design of this fullerene took into consideration the adjustment of the LUMO to have a better match with the donor material, mostly P3HT. This leads to an increase in the V_{oc}.[105] The molecular structure is shown in figure 8.2.

PEDOT:PSS

PEDOT is a highly conductive and semitransparent π-conjugated polymer.[106] To become processable from solution, PEDOT is combined with PSS forming the PEDOT:PSS composite. However PEDOT:PSS has an acidic nature with a PH-value between 1 and 2. PEDOT:PSS is widely used as HTL because it is not soluble in non-polar solvents, therefore it is possible to apply the active layers on top of it without damaging the PEDOT:PSS layer. It has a work function of -5.1 eV.[107]

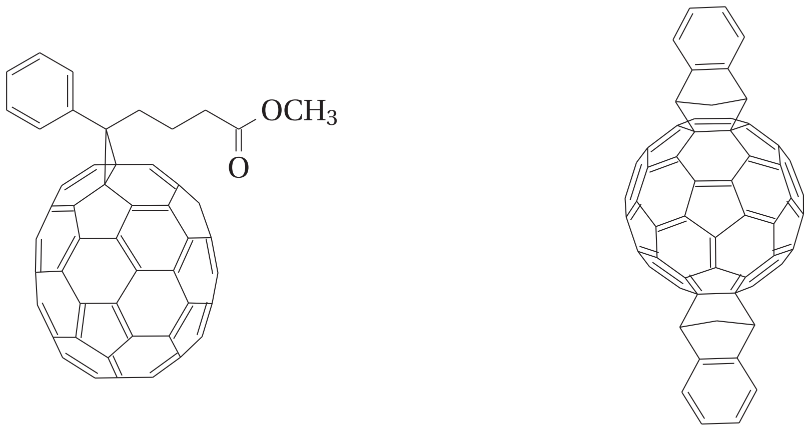

PC$_{71}$BM IC$_{60}$BA

Figure 8.2: Molecular structure of two fullerenes (PC$_{71}$BM and IC$_{60}$BA) used as electron acceptors in this work.

8.2 Solar modules with PCDTBT:PC$_{71}$BM

8.2.1 Architecture and solar module design

Single-junction solar modules were constructed using the inverted architecture shown in figure 8.3a. ZnO and MoO$_3$ are used as ETL and HTL respectively. The active layer comprises the mixture of PCDTBT:PC$_{71}$BM. ITO and silver are the bottom and top electrodes.
The first solar modules were built on a 16 x 16 mm^2 substrate. The substrate contains four different solar cells. P1, P2 and P3 were structured as shown in figure 8.3b. The ITO layer was structured as P1. The ZnO and the active layer were structured as P2. Finally, the silver/MoO$_3$ layers were structured as P3. An additional line, perpendicular to P1,P2 and P3, was realized to electrically insulate the device. The red square on top of the silver electrode shows the photo active area of one of the four solar cells. Two of the devices were structured as solar modules, keeping the other two as reference single-junction solar cells.

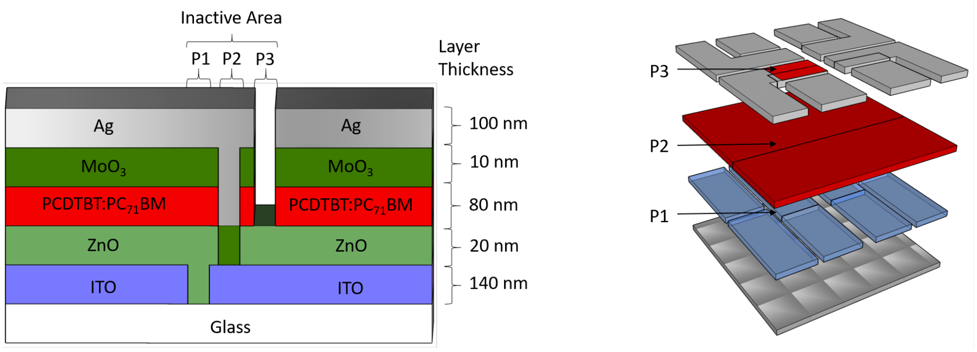

(a) (b)

Figure 8.3: (a) Single-junction solar module architecture showing the P1, P2 and P3 structuring steps. (b) Device architecture and design showing P1, P2 and P3 The red square on top of the silver electrode shows the photoactive area of one of the four solar cells. The substrate area is 16 x 16 mm^2.

8.2.2 Threshold fluences

The ITO and silver threshold fluences were determined in section 7.2 at $\lambda = 750\,\mathrm{nm}$. Similarly, the threshold fluence of the PCDTBT:$PC_{71}BM$ (P2) layer was calculated using the Liu method described in section 5.4. Single pulse ablation was achieved by moving the stage with a speed of $180\,\mathrm{mm\,s^{-1}}$. The logarithmic fit at $\lambda = 750\,\mathrm{nm}$ is shown in figure 8.4a. The extrapolated threshold fluence for PCDTBT:$PC_{71}BM$ is $F_{\mathrm{th}} = 40\,\mathrm{mJ\,cm^{-2}}$.

8.2.3 Structuring process optimization

The optimized parameters to structure P1, P2 and P3 were determined by changing the stage speed, testing different pulse overlaps with different fluences above the threshold fluence. The structuring requirements for each step are similar to the OLED modules (section 7.3). For P1 it is important to electrically insulate the bottom electrode of the different solar cells. For P2, it is important to completely remove the photoactive layer without damage to the ITO layer below. The complete removal of the PCDTBT:$PC_{71}BM$ and the ZnO layers enables a good electrical connection between bottom and top electrodes of neighboring solar cells. Finally, for P3 it is important to completely remove the silver top electrode, without damaging the ITO layer below. However, it is important to prevent damage to the active layer at this stage, as it prevents shorts between the silver and the ITO electrodes.

The structuring of the ITO (P1) at $\lambda = 750\,\mathrm{nm}$ was performed with the same parameters as for the OLED module in section 7.3, with $F = 350\,\mathrm{mJ\,cm^{-2}}$ and a pulse overlap of 73 %. The ablation showed slight damage to the glass that does not hamper the performance of the device. A fluence $F = 80\,\mathrm{mJ\,cm^{-2}}$ and a pulse overlap of 91% were used to structure PCDTBT:$PC_{71}BM$ (P2). The ITO layer is unscathed with clean removal of the PCDTBT:$PC_{71}BM$ (P2) layer. Small remainders are visible (Figure 8.4c), however, they do not affect the electrical connection between the ITO and the silver. The laser-written line width is $<10\,\mu\mathrm{m}$ (Figure 8.4b). Finally, silver/MoO_3 (P3) was structured using the same parameters as reported before for the OLED module with $F = 540\,\mathrm{mJ\,cm^{-2}}$ and pulse overlap of 66 %. The ablation resulted in no damage to the ITO layer and good electrical insulation of the neighboring silver electrodes. The width of laser-written lines is $<10\,\mu\mathrm{m}$.

8.2.4 Electrical characterization

The structuring parameters found in the previous section were used to build a solar module using the substrate design shown in figure 8.3b. The width of the inactive area between P1 and P3 was approximately $100 \pm 40\,\mu\mathrm{m}$, leading to a high GFF = 96 %. The large standard deviation comes from the manual alignment of the sample on the XYZ stage of the workstation. Figure 8.5 shows the J-V curves for the best solar module and reference solar cell. The solar module delivers a $V_{\mathrm{oc}} = 1.75\,\mathrm{V}$ twice the one of the solar cell that has $V_{\mathrm{oc}} = 0.870\,\mathrm{V}$. This indicates a working monolithic connection with clean ablation of the PCDBT:$PC_{71}BM$ layer. The smaller photoactive area of each solar cell in the solar module limits the current

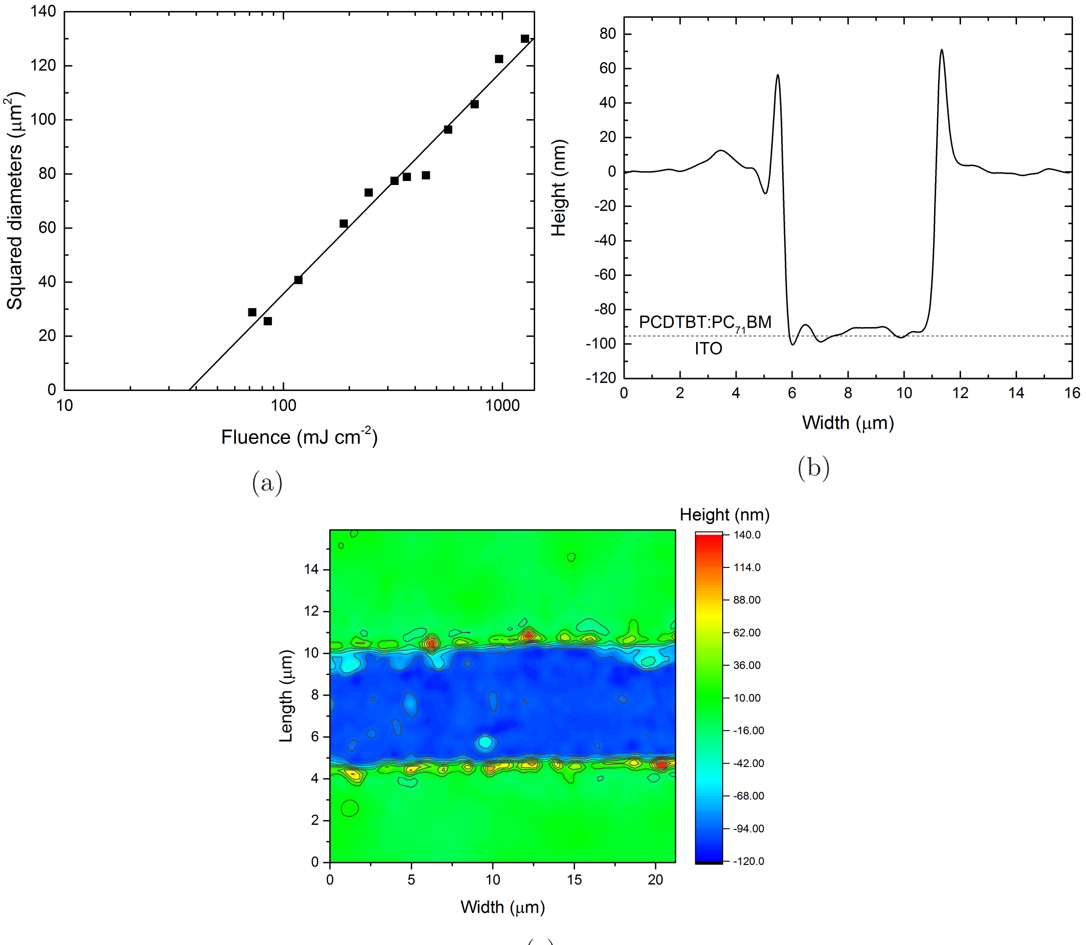

(a)

(b)

(c)

Figure 8.4: (a) Determination of the threshold fluence by a linear fit for PCDTBT:PC$_{71}$BM at $\lambda = 750$ nm. (b) and (c) Confocal images of the laser written lines into PCDTBT:PC$_{71}$BM (P2) at $\lambda = 750$ nm, using a $F = 80$ mJ cm^{-2} and a pulse overlap of 91 % (b) Profile image showing a width of < 10 µm and no damage to the ITO layer below. (c) 3D confocal image showing clean ablation with little remainders and no damage to the ITO layer below.

Table 8.1: Optoelectronic key performance parameters of the laser structured PCDBT:PC$_{71}$BM solar module.

Device	PCE (%)	FF (%)	J_{sc} (mA cm^{-2})	V_{oc} (V)	GFF (%)
Solar module	4.2	62	4.0	1.75	96
Solar cell	4.2	64	7.8	0.870	100

to approximately half of the current of the reference solar cell. The solar module produces $J_{sc} = 4$ mJ cm^{-2} compared to $J_{sc} = 7.8$ mJ cm^{-2} for the reference solar cell. The fill factors (64% and 62%), of the reference solar cell and solar module, are comparable. Finally the PCE = 4.2% is equivalent for both devices. The key performance parameters of the devices are summarized in table 8.1.

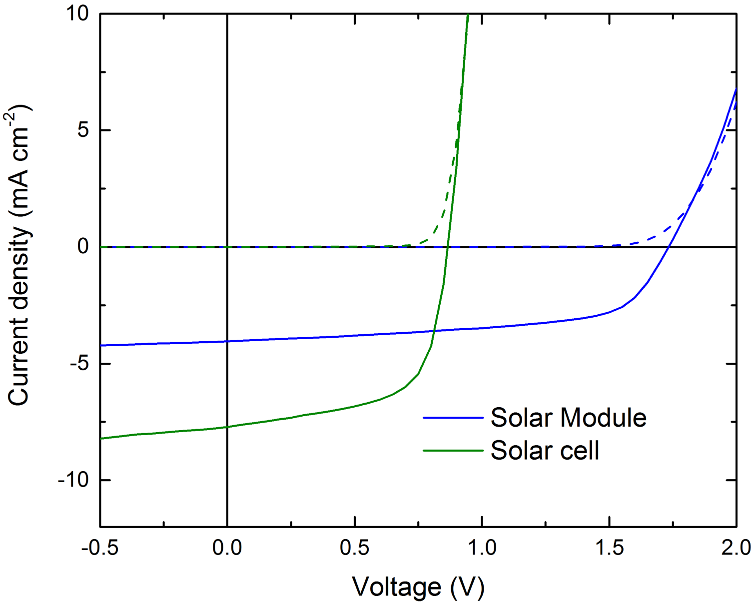

Figure 8.5: J-V curves of the best solar module and reference single-junction solar cell using PCDTBT:PC$_{71}$BM as photoactive layer.

8.3 Solar modules with nanoparticulate P3HT:IC$_{60}$BA

The use of nanoparticles dispersed in alcohol or water represents an ecofriendly alternative to the use of harmful solvents like chlorobenzene or dichlorobenzene to fabricate organic solar cells. This is specially important for the future industrial production of organic solar cells, as the use of toxic solvents may increase the production costs, making them less competitive. Highly efficient organic solar cells, using P3HT:ICBA nanoparticles dispersed in ethanol, have been demonstrated before.[108] The devices have also been upscaled to areas larger than 1 cm^2 using doctor blading.[109]

8.3.1 Architecture and solar module design

Figure 8.6a shows the architecture used for the solar module with the P1, P2 and P3 structuring steps. The P3HT:IC$_{60}$BA devices were built using an inverted architecture with ZnO and MoO$_3$ as ETL and HTL respectively. ITO and silver are used for the bottom and top electrodes. The main difference to the structuring process of PCDTBT:PC$_{71}$BM solar modules is that, here, the ITO and ZnO were structured together as the P1 step. In this section two solar module designs were used: a design with a photoactive area of 10.5 mm^2 depicted on figure 8.3b and a larger substrate (25 x 25 mm^2) with a photoactive area of 1.8 cm^2 (Figure 8.6b). The ITO and ZnO layers have an additional laser-written line that allows contact with the top electrode without shortening the device.

8.3.2 Threshold fluences

The ITO and silver threshold fluences were calculated in section 7.2. The threshold fluence for the P3HT:IC$_{60}$BA photoactive layer was determined using the Liu method (section 5.4).

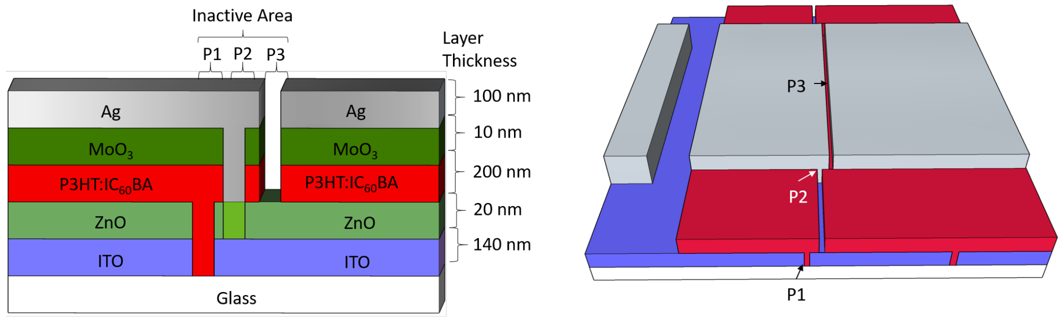

(a) (b)

Figure 8.6: (a) Single-junction solar module architecture with nanoparticulate P3HT:IC_{60}BA showing P1, P2 and P3 structuring steps. (b) 25 x 25 mm^2 design showing P1, P2 and P3 structuring steps. The solar module has a photoactive area of 1.8 cm^2.

The threshold fluence of the photoactive layer was determined at $\lambda = 550$ nm and $\lambda = 750$ nm. At $\lambda = 750$ nm, the ablation of the as-cast layer (before sintering) was also evaluated. The linear fits are shown in figure 8.7a. At $\lambda = 550$ nm, a threshold fluence $F_{\mathrm{th}} = 56\,\mathrm{mJ\,cm^{-2}}$ was calculated for the sintered layer. At $\lambda = 750$ nm, a threshold fluence $F_{\mathrm{th}} = 52\,\mathrm{mJ\,cm^{-2}}$ was calculated for the sintered layer. A threshold fluence $F_{\mathrm{th}} = 16\,\mathrm{mJ\,cm^{-2}}$ was determined for the as-cast layer at $\lambda = 750$ nm. The decrease in the threshold fluence has been observed before for nanoparticulate layers as compared with sintered layers by Chung et al.[110] This can be explained by a lower energy requirement to ablate the nanoparticles as compared with the layers. The threshold fluences at both wavelengths, $\lambda = 550$ nm and $\lambda = 750$ nm, show little change.

8.3.3 Structuring process optimization

The structuring process was optimized at $\lambda_1 = 550$ nm. Although ITO was structured together with ZnO (P1), the parameters of the neat ITO layer were used. ITO/ZnO was ablated with $F = 370\,\mathrm{mJ\,cm^{-2}}$ and a pulse overlap of 85 %. This leads to electrical insulation of the different sections structured on ITO with the laser. A fluence, $F = 70\,\mathrm{mJ\,cm^{-2}}$ and a pulse overlap of 85 % were used to structure P2. The 3D confocal image (Figure 8.7c) shows clean ablation facilitating a good contact between the bottom and top electrode. The width of the laser-written lines is $< 10\,\mu\mathrm{m}$ (Figure 8.7b). The same parameters reported in section 7.3, $F = 340\,\mathrm{mJ\,cm^{-2}}$ and a pulse overlap of 65 %, were used to structure the top electrode (P3). This leads to good electrical insulation of the top electrode and no damage to the ITO layer below. The laser-written line width is $< 10\,\mu\mathrm{m}$.

8.3.4 Electrical characterization

Solar modules were built using the two different designs depicted in figure 8.3b and figure 8.6b. The structuring parameters were initially tested on the 16 x 16 mm^2 substrate depicted in figure 8.3b. The devices were built using the process described by Sankaran et al.[109] Figure 8.8 shows the J-V curves of the best devices. The solar cell exhibits $V_{\mathrm{oc}} = 0.813$ V

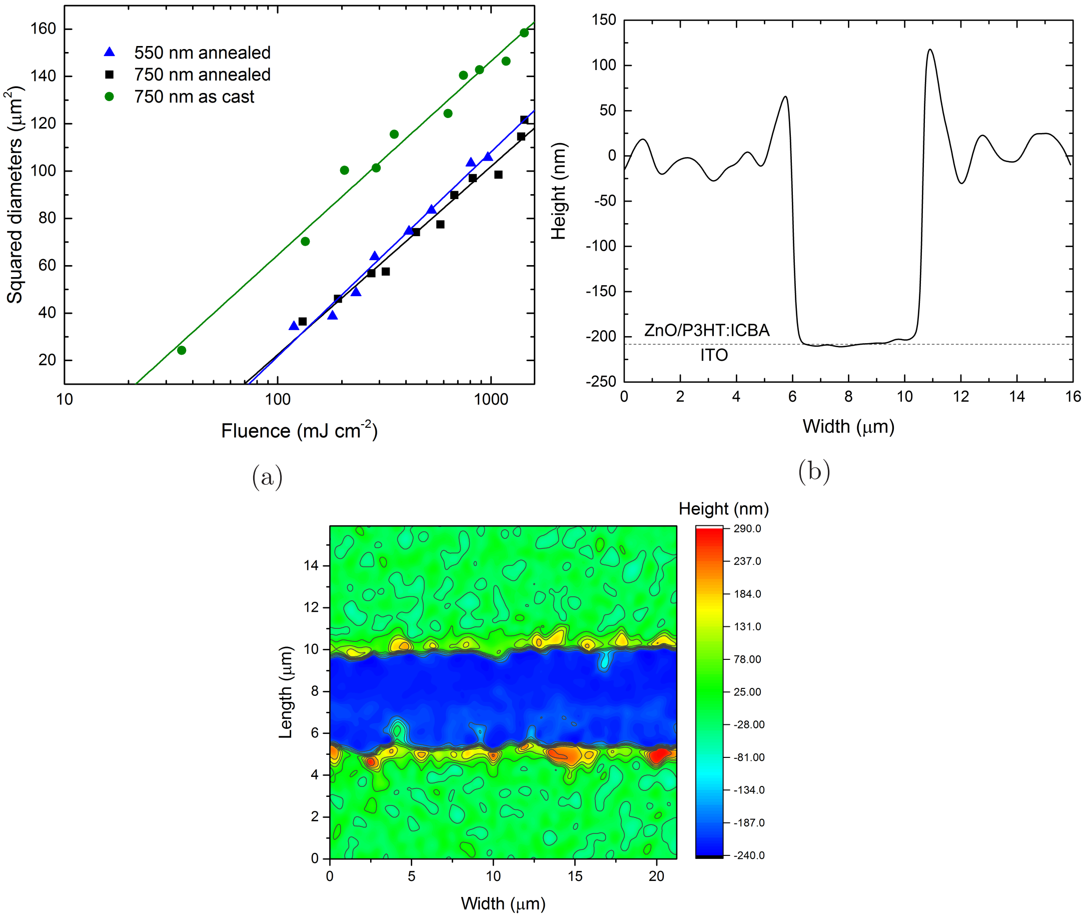

(a)

(b)

(c)

Figure 8.7: (a) Linear fits to determine the threshold fluences of P3HT:IC$_{60}$BA (P2) at $\lambda = 550\,\text{nm}$ and $\lambda = 750\,\text{nm}$. At $\lambda = 750\,\text{nm}$ the threshold fluence was calculated for both as cast and sintered layers. The as-cast layer shows a significant decrease of the threshold fluence. Both annealed threshold fluences at $\lambda = 550\,\text{nm}$ and $\lambda = 750\,\text{nm}$ are similar. (b) and (c) Confocal images for the structuring of P3HT:IC$_{60}$BA (P2) at $\lambda = 550\,\text{nm}$ with $F = 70\,\text{mJ cm}^{-2}$ and a pulse overlap of 85 % (b) Profile image showing a width of $< 10\,\mu\text{m}$ and no damage to the ITO layer below. (c) 3D image showing clean ablation with little remainders and no damage to the ITO layer below allowing a good connection between the electrodes of two neighboring solar cells.

compared to a $V_{\text{oc}} = 1.620\,\text{V}$ of the solar modules. The V_{oc} doubling reflects the working monolithic connection between the individual solar cells. The short-circuit current density was $J_{\text{sc}} = 3.2\,\text{mA cm}^{-2}$ for the solar module and $J_{\text{sc}} = 8.9\,\text{mA cm}^{-2}$ for the solar cell. A higher current density of $J_{\text{sc}} = 4.5\,\text{mA cm}^{-2}$ was expected for the solar module. The current density loss can be explained by the different areas of the connected solar cells. The smaller solar cell limited the current density of the whole device. This translates into a lower PCE as the solar cell exhibits a PCE = 3.8% compared to a PCE = 2.8% of the solar modules. The fill factor $FF = 57\%$ is slightly better for the solar modules than the $FF = 53\,\%$ for the solar cells. The change on fill factor may be attributed to the lower current density of the solar module. The small solar modules have a GFF = 96%.

The solar module's photoactive area was upscaled to $1.8\,\text{cm}^2$ using the design depicted in figure 8.6b. The devices were built using doctor blading as described by Sankaran et al.[109] Figure 8.8 shows the J-V curves for the solar modules composed of two solar cells. The solar

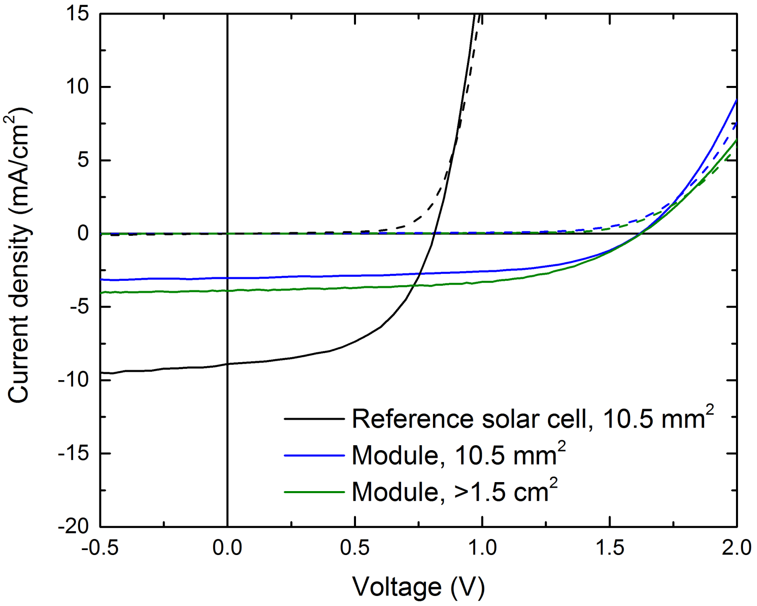

Figure 8.8: J-V curves of the best solar modules (10.5 mm^2 and 1.8 cm^2 and reference solar cell (10.5 mm^2 using nanoparticulate P3HT:ICBA.

Table 8.2: Optoelectronic key performance parameters for the laser structured nanoparticulate P3HT:ICBA solar modules.

Device	PCE (%)	FF (%)	J_{sc} (mA cm^{-2})	V_{oc} (V)	GFF (%)
Solar cell (0.1 cm^2)	3.8	53	8.9	0.813	100
Solar module (0.1 cm^2)	2.8	57	3.2	1.620	96
Solar module (1.8 cm^2)	3.5	55	3.9	1.620	98

module exhibits a $V_{oc} = 1.620$ V matching the voltage of the smaller solar modules. The fill factor $FF = 55$ %, shows some improvement over the $FF = 52$ % reported by Sankaran et al.[109] Notably, the devices built by Sankaran et al. were 33 % smaller. Therefore, the larger area of the devices reported herein also has an impact on the FF as more shunts can be expected. The solar module produces a $J_{sc} = 3.9$ mA cm^{-2}, showing a better alignment and fewer losses due to the small width of the inactive area of approximately 100 µm. The solar module exhibits a PCE = 3.5% similar to the smaller 10.5 mm^2 solar cell. The device has a GFF > 98 %. The key performance parameters of both, the 10.5 mm^2 solar cell and module and 1.5 cm^2 solar module, are summarized in table 8.2.

8.4 Tandem solar modules with PTB7:PC71BM

Tandem solar cells allow to increase the PCE of the photovoltaic devices beyond the Shockley–Queisser limit. Due to the thin-film nature of some of the organic solar devices, not all the light is absorbed by a single device. Hence, using twice the same absorber layer increases the light absorption and the PCE of the device. In this section the structuring process to manufacture tandem solar modules using PTB7:PC$_{71}$BM as absorber layer is described. The increase of the layer thickness of tandem devices, represent a challenge to remove the active layers and connect the neighboring solar cells into a module.

8.4.1 Architecture and solar module design

The architectures used for the single-junction and tandem solar modules are shown in figure 8.9. The tandem architecture is composed of two PTB7:PC$_{71}$BM solar cells connected through a recombination layer. A solvent barrier enables the deposition of the second solar cell. Here, PEDOT:PSS M-HTL Solar was used as solvent barrier. A second PEDOT:PSS formulation CPP 105D is used to improve the adherence of the M-HTL Solar layer on the absorber layer. ZnO and MoO$_3$ are used as ETL and HTL, respectively.

8.4.2 Threshold fluences

The ITO and silver threshold fluences were calculated in section 7.2. The threshold fluences for the single-junction and tandem active layers were determined at $\lambda = 550\,\mathrm{nm}$ and $\lambda = 750\,\mathrm{nm}$ using the Liu method (section 5.4). The threshold fluences at $\lambda = 550\,\mathrm{nm}$ were $F_{\mathrm{th}} = 35\,\mathrm{mJ\,cm^{-2}}$ for the single-junction absorber layer and $F_{\mathrm{th}} = 60\,\mathrm{mJ\,cm^{-2}}$ for the tandem absorber layer (Figure 8.10a). The threshold fluences at $\lambda = 750\,\mathrm{nm}$ were $F_{\mathrm{th}} = 40\,\mathrm{mJ\,cm^{-2}}$ for the single-junction absorber layer and $F_{\mathrm{th}} = 90\,\mathrm{mJ\,cm^{-2}}$ for the tandem absorber layer. The difference between the wavelengths could be caused by the change in the absorption for PTB7:PC$_{71}$BM as the absorption is slightly higher at $\lambda = 550\,\mathrm{nm}$ than at $\lambda = 750\,\mathrm{nm}$.[111] The difference between the single-junction and the tandem absorber layer threshold fluences is due to the layer thickness difference.

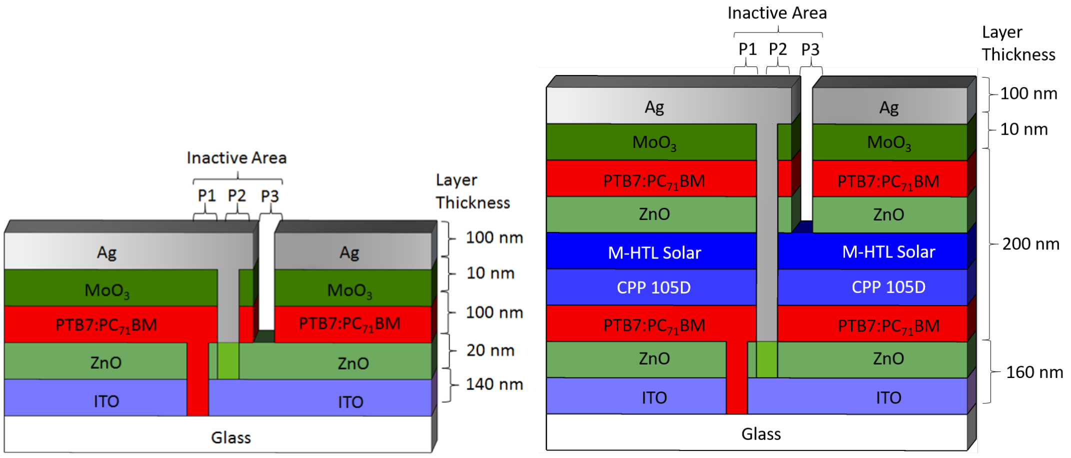

(a) (b)

Figure 8.9: (a) Single-junction solar module architecture with P1, P2 and P3 structuring steps. (b) Tandem solar module architecture with P1, P2 and P3 structuring steps.

8.4.3 Structuring process optimization

The process parameters were optimized at $\lambda = 550\,\text{nm}$. ITO/ZnO layer (P1) was structured using the parameters used in section 8.3. The optimized parameters to structure the photoactive layer (P2) are $F = 13\,\text{J cm}^{-2}$ and a pulse overlap of 85 % for the single-junction solar modules, and $F = 15\,\text{J cm}^{-2}$ and a pulse overlap of 89 % for the tandem solar modules.

The fluence and pulse overlap are slightly higher for the tandem devices to guarantee a clean ablation with negligible remainders (Figure 8.10c). The P2 structuring confocal profile image of the tandem device is shown in Figure 8.10b. There is no visible damage to the ITO underneath. Although the bulges are higher than 500 nm, they do not hamper the performance of the devices as no shorts can be created. The laser-written line width is $< 10\,\mu\text{m}$. To structure the silver/MoO_3 (P3) electrodes the same parameters as for the previously described single-junction modules were used (sections 8.2 and 8.3). The laser-written line into silver shows complete removal of the silver top electrode. However, the photoactive layer is not entirely removed on the tandem device.

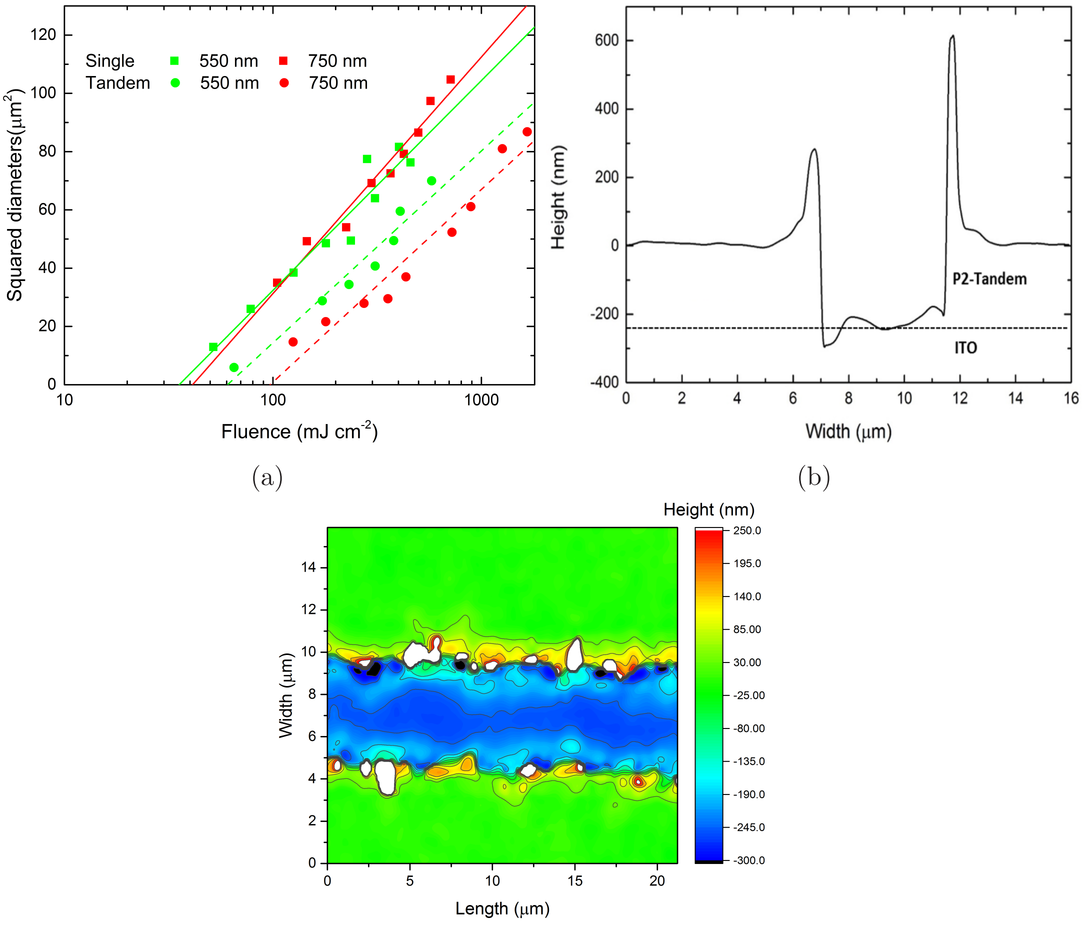

(a)

(b)

(c)

Figure 8.10: (a) Linear fits to determine the threshold fluences of PTB7:$PC_{71}BM$ in single-junction (continuous line) and tandem (dashed lines) devices at $\lambda = 550\,\text{nm}$ (green) and $\lambda = 750\,\text{nm}$ (red). (b) and (c) Confocal images of the laser-written line into the active layer (P2) in a tandem device at $\lambda = 550\,\text{nm}$ with $F = 15\,\text{mJ cm}^{-2}$ pulse overlap of 89% (b) Profile image showing a width of $< 10\,\mu\text{m}$ and no damage to the ITO layer below. (c) 3D confocal image showing clean ablation with no remainders and no damage to the ITO layer below.

8.4.4 Electrical characterization

Single-junction and tandem solar modules were built using the 16 x 16 mm^2 design shown in figure 8.3b. J-V curves for both single-junction and tandem solar cell and modules are depicted in figure 8.11. The voltage doubling due to the monolithic connection is evident as the single-junction solar modules exhibit a $V_{oc} = 1.451$ V while the single-junction solar cells exhibit a $V_{oc} = 0.720$ V. The solar tandem devices exhibit the voltage doubling as well. The tandem solar cells exhibit a $V_{oc} = 1.285$ V and the tandem solar modules exhibit a $V_{oc} = 2.476$ V. The tandem devices show a voltage loss when compared to the single-junction devices. This is probably due to water adsorption in the PEDOT:PSS layer during the structuring process. PEDOT:PSS is a hygroscopic material, and it has been demonstrated that this leads to water absorption and the degradation of the devices.[112] This effect is also reflected in the lower fill factor of the tandem reference solar cell ($FF = 48\%$) and solar module ($FF = 44\%$). The tandem solar cell exhibits PCE = 4.6 % and the tandem solar solar module exhibits PCE = 4.0 %. The single-junction solar cell and solar module exhibit PCE = 5.7 % and PCE = 5.5 %, respectively. Single-junction and tandem devices were completely built under nitrogen atmosphere with no exposition to air. The single-junction solar cells in nitrogen exhibit a PCE = 6.0 % and the tandem solar cells exhibit a PCE = 6.4 % for the tandem solar cells. The PCE reduction caused by air exposition is higher on the tandem devices that have the PEDOT:PSS layers than on the single-junction layers. The single junction solar modules have a GFF = 96% and the tandem solar modules have a GFF = 93%. The difference is due to the manual alignment of the devices on the XYZ stage of the workstation that leads to different inactive areas. The key performance parameters of the devices are summarized in table 8.3.

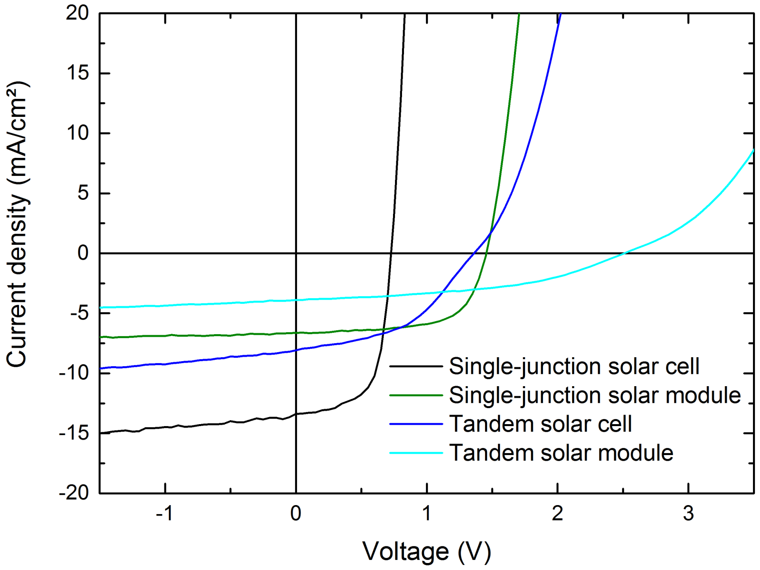

Figure 8.11: J-V curves for the single-junction, tandem solar cells and modules.

Table 8.3: Key performance parameters for the laser structured single-junction and tandem solar modules and reference cells using PTB7:PC$_{71}$BM as absorber layer.

Solar devices	PCE (%)	FF (%)	J_{sc} (mA cm^{-2})	V_{oc} (V)	GFF (%)
Single cell (Nitrogen)	6.0	60	14.1	0.720	100
Single cell (Air)	5.7	62	12.8	0.723	100
Single module (Air)	5.5	66	5.8	1.450	96
Tandem cell (Nitrogen)	6.4	53	8.3	1.460	100
Tandem cell (Air)	4.6	48	7.5	1.285	100
Tandem module (Air)	4.0	44	3.6	2.476	93

8.5 Rapid experimental optimization of the solar cell width

The width of each solar cell is very important for the final performance of a solar module. If the solar cell is too wide, the performance decreases due to the resistive losses in the electrode. If the solar cell is too narrow, a larger number of monolithic connections is necessary, resulting in an increase of the inactive area of the device. Hence, a compromise is necessary, and the width and number of solar cells in a module should be optimized. This has been accomplished using simulation methods where the resistance of the electrodes is estimated.[95]

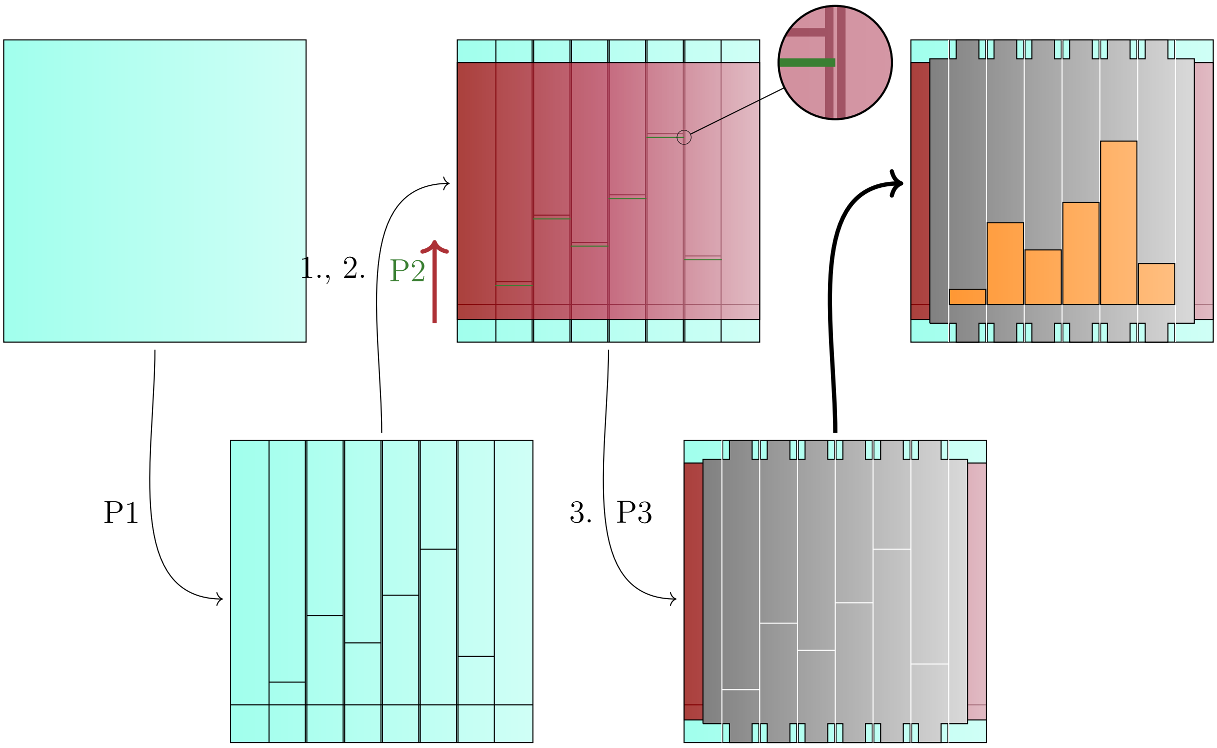

Figure 8.12: Substrate design for the solar cell width optimization. Initially the ITO is structured for different solar cell widths. The photoactive layer is coated and P2 is structured. The top electrode is coated and P3 is structured. The width of each of the solar cells is determined by the position of the monolithic connection. The solar cells are measured through the monolithic connection, hence considering the inactive area in the measurements. The solar cell widths are shown in orange.[113]

A substrate was designed to quickly find the optimum cell width in an experimental way. P1, P2 and P3 are structured using the laser ablation parameters found in section 8.4. Initially, the ITO electrode is structured. The position of P1 defines the solar cell widths to be evaluated. The photoactive layer and the top electrode are coated and structured forming a monolithic connection. The devices are measured through the monolithic connection, therefore the inactive area is considered in the measurements. The different widths are placed in different positions on the test substrates to account for possible inhomogeneities. The design construction process is shown in figure 8.12.

The sample design (Figure 8.12) was used to optimize the cell width of single-junction and tandem solar modules according to the architectures depicted in figure 8.9. The V_{oc} remains constant for the different solar cell widths (Figure 8.13a). The J_{sc} slightly declines for the single-junction devices with larger solar cell widths and it remains almost constant for the tandem devices (Figure 8.13b). The fill factor is the parameter with the highest impact. It decreased from 70% to less than 45% for the single-junction devices and from 52% to 45% for the tandem devices when the solar cell width is increased (Figure 8.13c). The larger

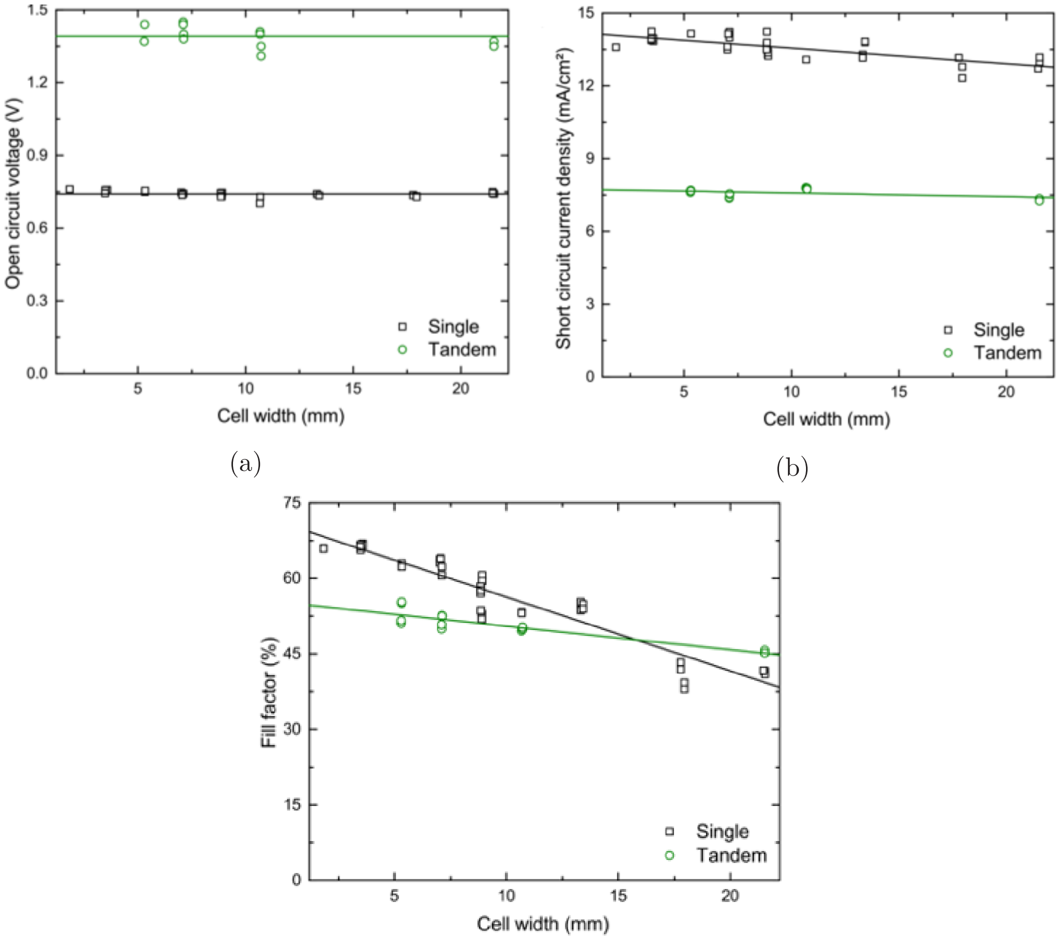

(a)

(b)

(c)

Figure 8.13: Key performance parameters for the single-junction and tandem devices for different cell widths. a) Short circuit current density against solar cell width. It shows a slight decline for the single-junction device but almost none for the tandem with larger cell lengths. b) Fill factor against solar cell width. The fill factor shows a significant decrease for the single-junction device with larger cell widths. c) The V_{oc} remains constant within the evaluated width range.[113]

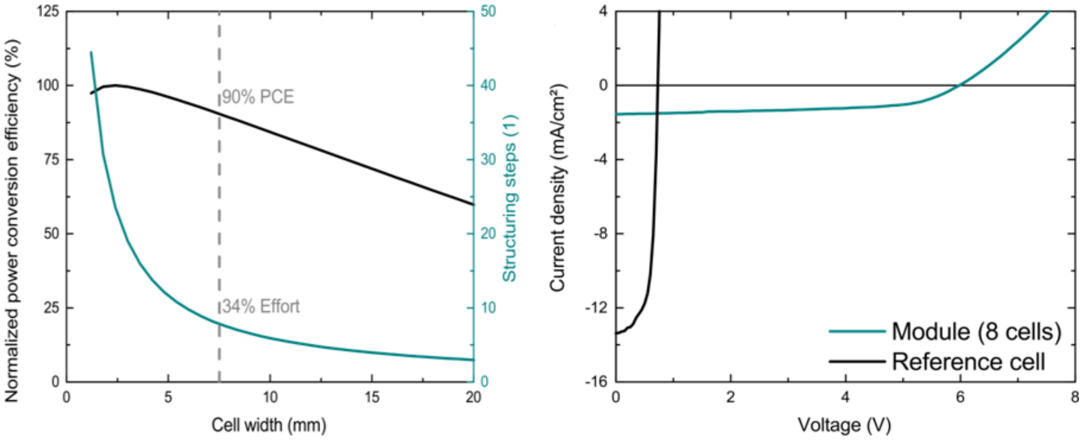

(a) (b)

Figure 8.14: a) Number of structuring steps and PCE versus cell width. b) J-V curves of the reference solar cell (10.5 mm^2) and the eight-cell-solar module (6.5 cm^2) built with the previously determined solar cell width. The solar module has 87 % of the reference solar cell PCE.[113]

reduction for the single devices stems from the larger operating currents that increase the ohmic losses.

Solar modules were built to prove the previous findings focusing on the single-junction devices as they showed the higher decline. Figure 8.14a shows that the maximum PCE is achieved with a solar cell width of 2.4 mm. However, this requires the maximum number of monolithic connections, hence of laser structuring steps. A solar cell width of 6 mm will yield 90% of the maximum PCE, but will require 34% less structuring steps resulting in a reasonable exchange that will ease the fabrication of the devices.The decrease in the number of processing steps may also lead to a higher yield as there are fewer possibilities of defects.

Solar modules were then built with a total photoactive area of 6.5 cm^2. The J-V curves for both the reference solar cell (10.5 mm^2) and the solar module are shown in figure 8.14b. The solar module has PCE = 5.0% and the reference solar cell has PCE = 5.7% (Figure 8.14b). The ratio between both PCEs is 87% demonstrating the accuracy of the experimental method (90% was predicted). The slightly lower PCE can be explained due to the larger area (6.5 cm^2) leading to more inhomogeneities of the layers. The solar modules have a GFF = 99% demonstrating the reduction of the lost area with the use of lasers.

8.6 Discussion

In this chapter, laser structuring of monolithic connections to construct organic solar modules was demonstrated. The devices were built using three different photoactive layers, PCDTBT:PC$_{71}$BM, nanoparticulate P3HT:IC$_{60}$BA and PTB7:PC$_{71}$BM in single-junction and tandem architectures. Table 8.4 shows a summary of the threshold fluences of these materials.

The threshold fluence of the single-junction devices, using PCDTBT:PC$_{71}$BM and PTB7:PC$_{71}$BM, are similar (35 and 41 mJ cm^{-2}). The threshold fluence of the sintered

Table 8.4: Threshold fluences of the photoactive layers PCDTBT:$PC_{71}BM$, nanoparticulate P3HT:$IC_{60}BA$ and PTB7:$PC_{71}BM$ in single-junction and tandem architectures.

Material	$\lambda = 550\,\mathrm{nm}$ (mJ cm^{-2})	$\lambda = 750\,\mathrm{nm}$ (mJ cm^{-2})
PCDTBT:$PC_{71}BM$	-	40
P3HT:$IC_{60}BA$ sintered	56	52
P3HT:$IC_{60}BA$ as-cast	-	16
PTB7:$PC_{71}BM$ single-junction	35	41
PTB7:$PC_{71}BM$ tandem	60	90

P3HT:$IC_{60}BA$ nanoparticulate layer is slightly higher. This could be caused by the thicker layer of P3HT:$IC_{60}BA$ (200 nm). The as-cast P3HT:$IC_{60}BA$ nanoparticulate layer has a significantly lower threshold, as the nanoparticles are easier to ablate as shown by by Chung et al.[110]. The effect of the wavelength is evident on the PTB7:$PC_{71}BM$ layers, both single-junction and tandem. The increase at $\lambda = 750\,\mathrm{nm}$ may be originated from the sharp absorption reduction of the layer.

Ultrashort pulsed lasers are suitable to structure solar modules using ITO as bottom electrode on a glass substrate. The large working window between the threshold fluence of ITO (P1) and the threshold fluence of the photoactive layers (P2), facilitates the selective ablation of the P2 layer. Although the silver (P3) has a higher threshold fluence than the ITO (Figure 7.3a), the ablation without damage to the ITO is possible when working with a fluence close to the threshold fluence of silver and a low pulse overlap.

Finally, the use of ultrashort pulsed lasers facilitate the experimental optimization of the solar modules. One substrate is enough to test and to find the most adequate solar cell width in terms of PCE and number of processing steps. The PCE of the test solar module was 87 % of the PCE of the reference solar cell (Maximum expected PCE). The prediction of the experiment was 90%. The small difference can be explained due to the larger photoactive area of the test solar modules. The GFF of these devices was higher than 99 % again demonstrating the advantages of using ultrashort pulsed lasers.

9 All-solution semi-transparent modules

ITO has been the most used semi-transparent electrode in OPV. However, it has several disadvantages, as it cannot be produced through a roll-to-roll process and it is highly brittle which limits its applicability in mechanically flexible devices, which is one of the inherent advantages of OPV. Likewise, the use of vacuum processed metal top electrodes hinders the implementation of a full roll-to-roll process that will decrease the future price of OPV. Several alternatives have been studied to substitute both electrodes, such as metal inks,[114–117] *silver nanowires,*[117–122] *high conductive polymers,*[121–124] *metal grids*[125] *and hybrids.*[126–132] *All-solution solar modules have also been constructed following this concept,*[117] *however P1, P2 and P3 have been mechanically scribed leading to low geometric fill factors and imprecision due to the manual processes performed to structure.*

In this chapter ultrashort pulse lasers were used to structure a flexible all-solution solar module. The materials and the device architecture are described in section 9.1. In section 9.2 the threshold fluences for the different materials is determined. Section 9.3 describes the ablation process for certain wavelengths and in section 9.4 the construction of a laser structured solar module is described. Section 9.5 provides a short discussion of the results depicted in this chapter. This results depicted in this chapter were part of the master thesis of Torsten Friedrich. The device architecture was developed by Jens Czolk, Manuel Koppitz and Dominik Landerer.[132]

9.1 Materials and architecture

9.1.1 Materials

ZnO was used as ETL, and the material is described in section 7.1. PEDOT:PSS is used to improve the lateral conductivity of the silver mesh on PET used in this chapter. PEDOT:PSS is described in section 8.1.

PET foil with silver mesh

A 50 µm thick PET foil with 10 µm wide and 40 nm thick printed silver lines was used as bottom electrode. The silver mesh covers 9 % of the PET substrate as depicted on figure 9.1a. The silver mesh electrode has a sheet resistance $R_{\square} = 16\,\Omega\,\square^{-1}$ which is comparable to that of ITO on glass and lower than that of ITO on PET. The transmission of the PET with the silver grid is close to 80 % as shown in figure 9.1b. When combined with a layer of PEDOT:PSS the transmission declines slightly in the infrared spectral regime.

Hybrid electrodes (HYE) comprising PEDOT:PSS and silver nanowires

A commercially available solution of PEDOT:PSS mixed with silver nanowires (Clevios HYE) was used as one of the electrodes. The nanowire diameter was estimated to be approximately 20 nm. They have an average length of 20 µm. The sheet resistance of the corresponding electrodes are dependent on the thickness. Therefore a compromise between sheet resistance and transmission of the layer is necessary (Figure 9.1d). Figure 9.1c shows an SEM image of the nanowires combined with PEDOT:PSS. The nanowires are homogeneously distributed.

PBTZT-stat-BDTT-8

PBTZT-stat-BDTT-8 is a royal blue polymer with absorption peaks at $\lambda = 600$ nm and $\lambda = 640$ nm. It is composed of substituted benzodithiophene, thiophene, and benzothiadiazole. The LUMO and HOMO are reported to be -3.7 and -5.4 eV, respectively. The material has demonstrated PCE = 4.5% for semi-transparent flexible devices. It was used on the con-

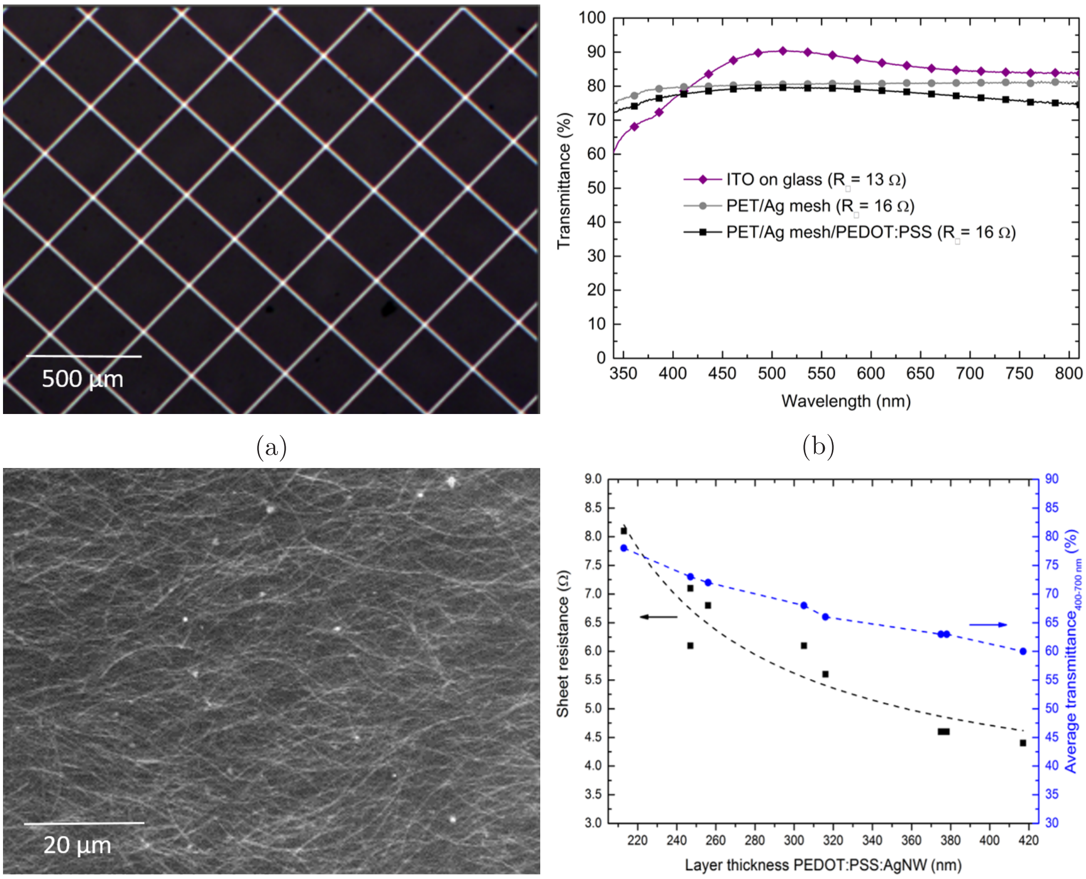

(a) (b)

(c) (d)

Figure 9.1: (a) Silver grid optical microscope image. (b) Transmission of the silver grid alone and in combination with PEDOT:PSS.(c) SEM image of the HYE electrode. The nanowires are homogeneously distributed inside the PEDOT:PSS layer. (d) Transmission and sheet resistance versus layer thickness of the HYE electrode.[132]

struction of the ”Solar Tree”, an exhibition showing the potential of OPV during the Expo Milan, 2015.[133]

$PC_{60}BM$

[6,6]-phenyl C_{61} butyric acid methyl ester ($PC_{60}BM$) is a fullerene derivative that is one of the most common acceptor materials used in OPV research. It was first discovered in 1995 as soluble derivative of C_{60}.[134] The LUMO and HOMO level are reported to be -4.3 and -6.0 eV respectively.[16] It has a moderate absorption and therefore does not contribute to the generation of electron-hole pairs in the organic solar cell.

techPCBM

techPCBM is a combination of $PC_{60}BM$ and $PC_{71}BM$ with a ratio of 9:1. The material possesses some of the advantages of $PC_{71}BM$ (section 8.1). The combination with $PC_{60}BM$ reduces the price, making it more suitable for future large scale industrial applications.

9.1.2 Architecture

An inverted architecture was used to build semi-transparent solar modules. The silver grid in combination with PEDOT:PSS form the bottom electrode. For the construction of the solar modules the silver grid was pre-structured during the printing process. Hence the structuring efforts were focused on the selective ablation of the PEDOT:PSS layer. ZnO is used as ETL and together with PBTZT-stat-BDTT-8:techPCBM is structured as P2. HYE layer is used as top electrode. No extra HTL was used, as PEDOT:PSS is a common HTL

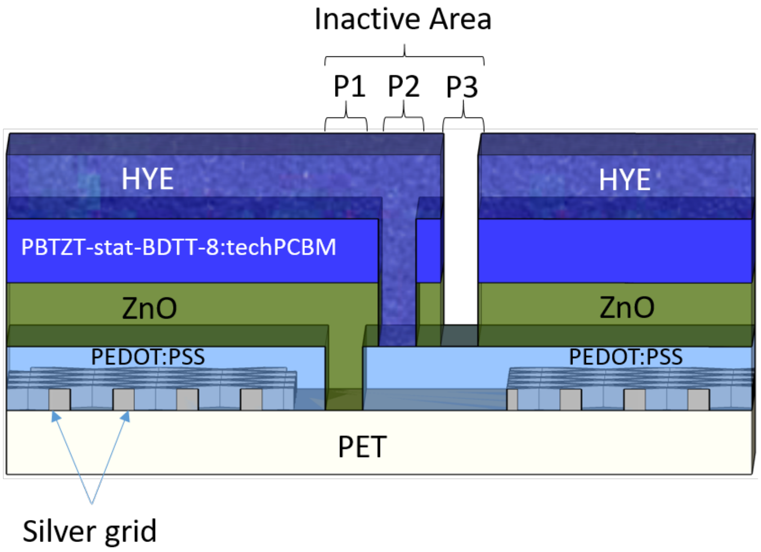

Figure 9.2: Semi-transparent solar module architecture with layer thicknesses and P1, P2 and P3 structuring steps. The bottom electrode is a hybrid electrode composed of a silver grid and PEDOT:PSS. PEDOT:PSS is structured as P1 using the ultrashort pulsed laser. The silver grid is pre structured. ZnO is used as ETL and together with the BTZT-stat-BDTT-8:techPCBM layer, it is structured during the P2 step. Finally the top electrode is fabricated from HYE and it is structured as P3.

with a suitable work function. The device architecture and P1, P2 and P3 structuring steps of the solar module is depicted in figure 9.2. All the layers were processed from solution using doctor blading with the exception of the silver grid. To process the layers on the PET substrate, it is attached to a glass substrate using a solvent. However, the solvent layer thickness between the glass and the PET changes from sample to sample, leading to changes of the thickness of the different layers.

9.2 Threshold fluences

The threshold fluences were determined using the Liu method (section 5.4) for the wavelengths $\lambda = 360\,\mathrm{nm}$, $\lambda = 410\,\mathrm{nm}$, $\lambda = 450\,\mathrm{nm}$, $\lambda = 500\,\mathrm{nm}$, $\lambda = 550\,\mathrm{nm}$, $\lambda = 575\,\mathrm{nm}$, $\lambda = 600\,\mathrm{nm}$, $\lambda = 650\,\mathrm{nm}$, and $\lambda = 700\,\mathrm{nm}$. The threshold fluences are plotted on Figure 9.3a. The absorption of PEDOT:PSS, PBTZT-stat-BDTT-8:techPCBM and HYE are depicted in Figure 9.3b. PBTZT-stat-BDTT-8:techPCBM and HYE absorptions were measured on the stack and not the individual layers.

For PEDOT:PSS (P1) a relationship between the threshold fluence and the absorption spectrum is observed. The highest threshold fluence matches with the lowest absorption at $\lambda = 410\,\mathrm{nm}$. The absorption increases at $\lambda = 360\,\mathrm{nm}$ causing a decrease in the threshold fluence. The threshold fluence shows a slight increase in the range from $\lambda = 550\,\mathrm{nm}$ to $\lambda = 700\,\mathrm{nm}$ from $F_{\mathrm{th}} = 50\,\mathrm{mJ\,cm^{-2}}$ to $F_{\mathrm{th}} = 75\,\mathrm{mJ\,cm^{-2}}$.

The threshold fluence of PBTZT-stat-BDTT-8::techPCBM also correlates with the absorption. The highest absorption of the PBTZT-stat-BDTT-8:techPCBM (P2) was found at $\lambda = 360\,\mathrm{nm}$ coinciding with the lowest threshold fluence of $F_{\mathrm{th}} = 13\,\mathrm{mJ\,cm^{-2}}$. As the absorption increases, the threshold fluence decreases towards $\lambda = 575\,\mathrm{nm}$. The threshold fluences remain consistent with small variations between $\lambda = 500\,\mathrm{nm}$ and $\lambda = 650\,\mathrm{nm}$. At $\lambda = 700\,\mathrm{nm}$ the threshold fluence increases which can be attributed to the reduction of the absorption.

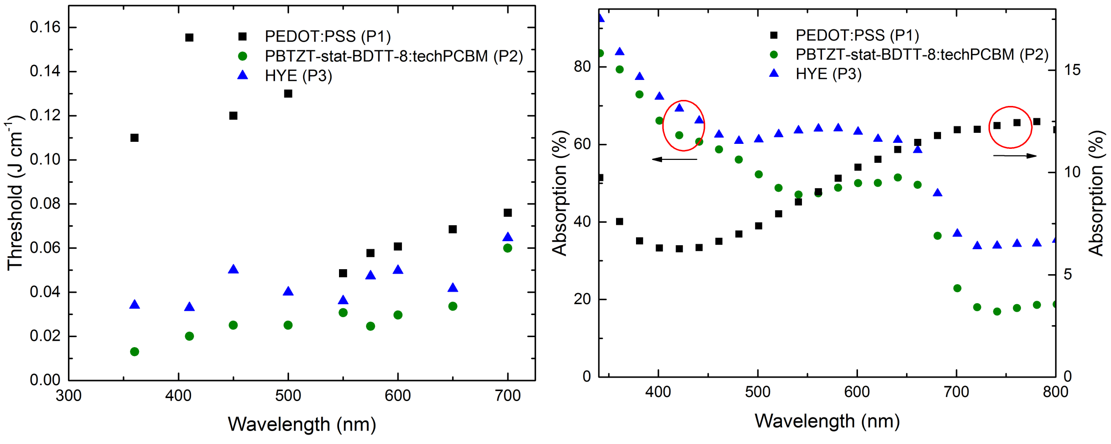

(a)

(b)

Figure 9.3: (a) Threshold fluences of PEDOT:PSS, PBTZT-stat-BDTT-8:techPCBM and HYE. (b) Absorption spectra of PEDOT:PSS, PBTZT-stat-BDTT-8:techPCBM and HYE.

The threshold fluences of HYE follows a similar pattern with the minimum located at $\lambda = 360\,\text{nm}$ and $\lambda = 410\,\text{nm}$ with $F_{\text{th}} = 34\,\text{mJ}\,\text{cm}^{-2}$ and $F_{\text{th}} = 33\,\text{mJ}\,\text{cm}^{-2}$ respectively. The threshold fluence $F_{\text{th}} = 50\,\text{mJ}\,\text{cm}^{-2}$ at $\lambda = 450\,\text{nm}$. The threshold fluence shows slight changes between $\lambda = 550\,\text{nm}$ and $\lambda = 650\,\text{nm}$. At $\lambda = 700\,\text{nm}$ there is again an increase following the abrupt reduction in the absorption.

The threshold fluence for the three layers do not match equations 5.9 and 5.10. The equations predicted a linear relationship between the threshold fluence and the wavelength. The different observation may originate from the thin-film nature and the transparency of the materials as the equations were developed using the assumptions of having bulk materials and surface processes.

9.3 Structuring process optimization

As PEDOT:PSS is an important material that is commonly used in organic electronics, here the ablation results are shown for three different wavelengths, $\lambda = 360\,\text{nm}$, $\lambda = 450\,\text{nm}$ and $\lambda = 600\,\text{nm}$. A single wavelength, $\lambda = 600\,\text{nm}$, was studied to ablate PBTZT-stat-BDTT-8:techPCBM (P2) and HYE (P3). $\lambda = 600\,\text{nm}$ was chosen as the PBTZT-stat-BDTT-8:techPCBM (P2) photoactive layer exhibits the highest absorption in this point.

9.3.1 PEDOT:PSS structuring (P1)

Fluences close to the threshold fluence were tested using different stage speeds, thus changing the pulse overlap to find the adequate structuring parameters. The bottom electrode is composed of the silver grid and a layer of PEDOT:PSS. The silver grid was pre-structured. Therefore, the focus was on the structuring of PEDOT:PSS to complement the pre-structuring process. One of the requirements to structure PEDOT:PSS is to diminish the damage on the PET layer following the considerations in chapter 6. A second structuring requirement is to produe the bulges below 200 nm to prevent shorts with the top electrode. Finally, it is important to completely remove the PEDOT:PSS layer to electrically insulate the two solar cells.

PEDOT:PSS has been previously structured using laser ablation. Semaltianos et al. used a picosecond laser to structure PEDOT:PSS on top of glass.[135] Photomechanical ablation was identified as the possible ablation mechanism. The threshold fluence was calculated at $F_{\text{th}} = 130\,\text{mJ}\,\text{cm}^{-2}$ for $\lambda = 1064\,\text{nm}$, with 10 ps pulses and layers with a thickness of 100 nm. No measurements of the bulge height were provided for the laser-written lines. Schoonderbeek et al. tested the ablation of PEDOT:PSS on top of PET with both ns and ps laser sources.[136] The ns pulses achieved no optimized ablation and formed melted lines. The ps pulses at $\lambda = 1030\,\text{nm}$ and $\lambda = 515\,\text{nm}$ resulted in complete removal of the PEDOT:PSS.

Laser structuring at λ=360 nm

Selective ablation of PEDOT:PSS on top of PET was not achieved. At $\lambda = 360\,\text{nm}$ the ablation threshold of PEDOT:PSS, $F_{\text{th}} = 78\,\text{mJ}\,\text{cm}^{-2}$, is higher than the threshold fluence of PET, $F_{\text{th}} = 40\,\text{mJ}\,\text{cm}^{-2}$. The confocal profile show an ablation depth close to 600 nm and peaks higher than 1000 nm (Figure 9.4). Overlapping the pulses to achieve continuous lines increased the damage on the PET substrate. Therefore, ablation at $\lambda = 360\,\text{nm}$ is not suitable to structure PEDOT:PSS on top of PET.

Laser structuring at λ=450 nm

A fluence $F = 135\,\text{mJ}\,\text{cm}^{-2}$ slightly higher than the threshold fluence $F_{\text{th}} = 120\,\text{mJ}\,\text{cm}^{-2}$ was chosen. Figure 9.5a shows the 3D confocal image of the laser-written line with a pulse overlap of 77 %. The laser-written line shows complete removal of the PEDOT:PSS layer with slight damage to the PET below. The laser-written line achieved electrical insulation with a laser-written line width of $< 10\,\mu\text{m}$ (Figure 9.5b). The bulges are higher than 200 nm, increasing the possibility of shunts with the top electrode. A higher pulse overlap was explored to decrease the bulge height. Significant damage to the PET layer below occurred. A fluence slightly lower than the threshold fluence, $F = 100\,\text{mJ}\,\text{cm}^{-2}$, was then evaluated. Although the single pulse ablation is not possible with this fluence, the pulse overlap created some sort of incubation effect, probably due to surface modifications. These surface modifications resulted in the reduction of the threshold fluence, and therefore the possibility of structuring with a fluence lower than F_{th}. Figure 9.5c shows the laser-written line with $F = 100\,\text{mJ}\,\text{cm}^{-2}$ and a pulse overlap of 88 %. The line shows a reduction on the bulge height to 120 nm and complete removal of the PEDOT:PSS layer, achieving electrical insulation. The PET

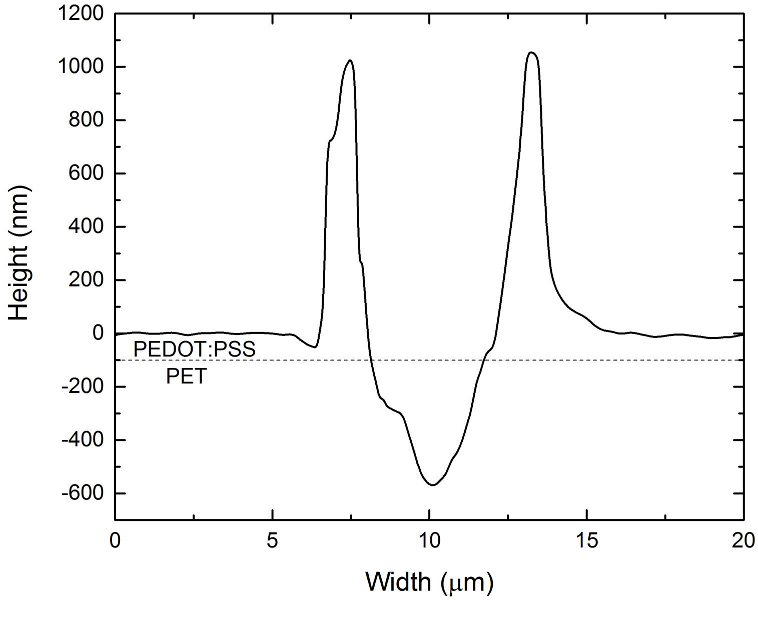

Figure 9.4: Confocal profile picture of the single pulse ablation of PEDOT:PSS on top of PET $\lambda = 360\,\text{nm}$. The PET shows significant damage as the ablation depth is close to 600 nm. The ablation bulges are above 1000 nm.

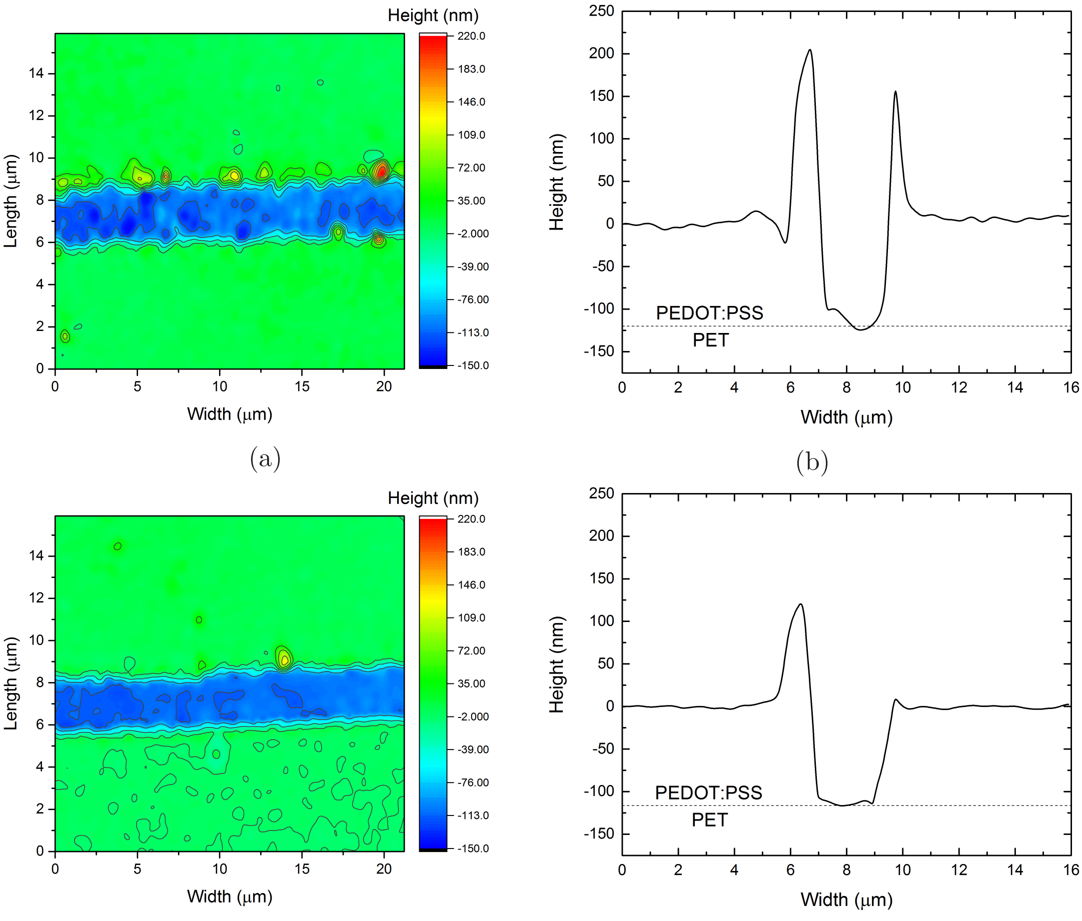

(a) (b) (c) (d)

Figure 9.5: (a) and (b) 3D confocal image and profile for the laser-written line on PEDOT:PSS at $\lambda = 450\,\mathrm{nm}$, $F = 130\,\mathrm{mJ\,cm^{-2}}$ and pulse overlap of 77%. The line shows slight damage to the PET substrate below. The bulge height is 200 nm. (c) and (d) 3D confocal image and profile for the laser-written line on PEDOT:PSS at $\lambda = 450\,\mathrm{nm}$, $F = 100\,\mathrm{mJ\,cm^{-2}}$ and pulse overlap of 88 %. The increase in pulse overlap leads to lower bulge height (120 nm) with negligible damage to the pet substrate below.

substrate before shows little damage with a laser-written line width of $< 10\,\mu\mathrm{m}$ (Figure 9.5d). The increase in pulse overlap resulted in lower bulges on the laser-written lines.

Laser structuring at λ=600 nm

A fluence $F = 100\,\mathrm{mJ\,cm^{-2}}$ higher than the threshold fluence $F_{\mathrm{th}} = 60\,\mathrm{mJ\,cm^{-2}}$ was chosen at $\lambda = 600\,\mathrm{nm}$. Figure 9.6a shows the 3D confocal image of the laser-written line with a pulse overlap of 84 %. Negligible damage to the PET substrate was produced by the laser ablation. The laser-written line has width of $< 10\,\mu\mathrm{m}$ and complete removal of the PEDOT:PSS layer leading to electrical insulation of the bottom electrode. The bulges present on the line are higher than 300 nm (Figure 9.6b) increasing the possibility of shunts with the top electrode. The pulse overlap was increased to 98%, successfully reducing the bulge height under 150 nm (Figure 9.6d). The laser-written lines show complete removal of the PEDOT:PSS layer achieving electrical insulation and a width of $\leq 10\,\mu\mathrm{m}$. The PET substrate shows negligible

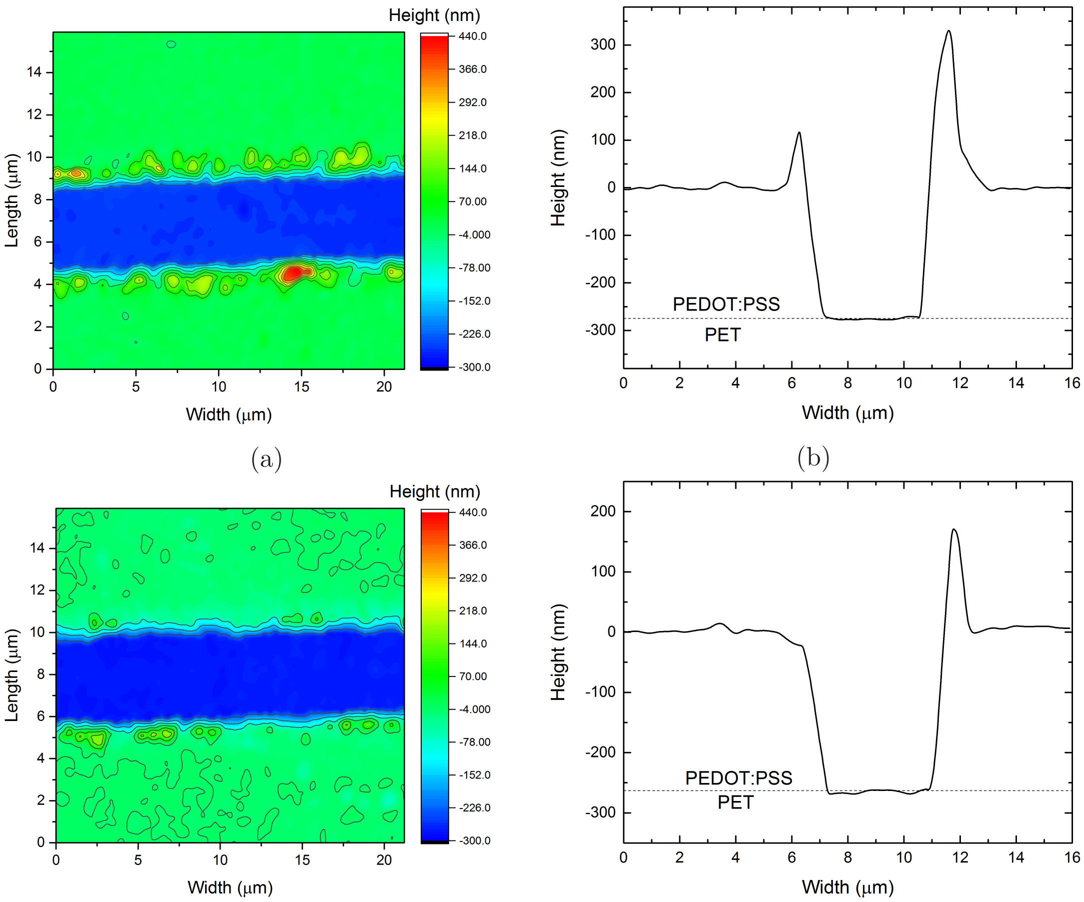

(a) (b)

(c) (d)

Figure 9.6: (a) and (b) 3D confocal image and profile for the laser-written line into PEDOT:PSS at $\lambda = 600\,\mathrm{nm}$, $F = 100\,\mathrm{mJ\,cm^{-2}}$ and pulse overlap of 84 %. The line shows negligible damage to the PET substrate below. The bulge height is 300 nm. Laser-written line width is $< 10\,\mu\mathrm{m}$.(c) and (d) 3D confocal image and profile for the laser-written line into PEDOT:PSS at $\lambda = 600\,\mathrm{nm}$, $F = 100\,\mathrm{mJ\,cm^{-2}}$ and pulse overlap of 98%. The line shows negligible damage to the PET substrate below. The increase in the pulse overlap leads to a reduction of the bulge to 150 nm. Laser-written line width is $< 10\,\mu\mathrm{m}$.

damage (Figure 9.6c). Similar to the case at $\lambda = 450\,\mathrm{nm}$, the increase in pulse overlap resulted in lower bulges.

9.3.2 PBTZT-stat-BDTT-8:techPCBM (P2) structuring

One of the requirements to structure PBTZT-stat-BDTT-8:techPCBM (P2) is to minimize the damage to the PEDOT:PSS layer below. The bulge height does not play an important role, as they do not cause any shunt. Complete removal of the PBTZT-stat-BDTT-8:tech-PCBM (P2) improves the connection of the devices as the remaining PBTZT-stat-BDTT-8:techPCBM (P2) would increase the serial resistance hampering the performance of the device.

Laser structuring at λ=600 nm

The structuring of PBTZT-stat-BDTT-8:techPCBM (P2) was optimized at $\lambda = 600\,\mathrm{nm}$, using a $F = 30\,\mathrm{mJ\,cm^{-2}}$ which is slightly higher than the threshold fluence $F_{\mathrm{th}} = 25\,\mathrm{mJ\,cm^{-2}}$.

Figure 9.7a shows the 3D confocal image of the ablation with a pulse overlap of 75 %. The laser-written line has an average ablation depth of 105 nm resulting in slight damage to the PEDOT:PSS layer below. The damaged is due to melting of the PEDOT:PSS layer. The laser-written line width is < 5 µm (Figure 9.7b).

The pulse overlap plays an important role in the selective ablation of thin-films. The pulse overlap was evaluated from 70 % to 98 % (Figure 9.7c). Up to a pulse overlap of 87 % the ablation depth is close to 100 nm, resulting in negligible damage to the PEDOT:PSS layer below. A pulse overlap of 90 % increases the average ablation depth to 140 nm due to the presence of ablation on the PEDOT:PSS. A pulse overlap of 92% results in the complete removal of the PEDOT:PSS layer below. The reason for the ablation of the layer below is the incubation effect created by the previous pulses. The incubation effects with a pulse overlap higher than 90 % increase the absorption enough to lead to ablation of the PEDOT:PSS layer below even when part of the energy was already used to ablate the PBTZT-stat-BDTT-8:techPCBM. These results accentuate the importance of the pulse overlap in the selective ablation of thin-films.

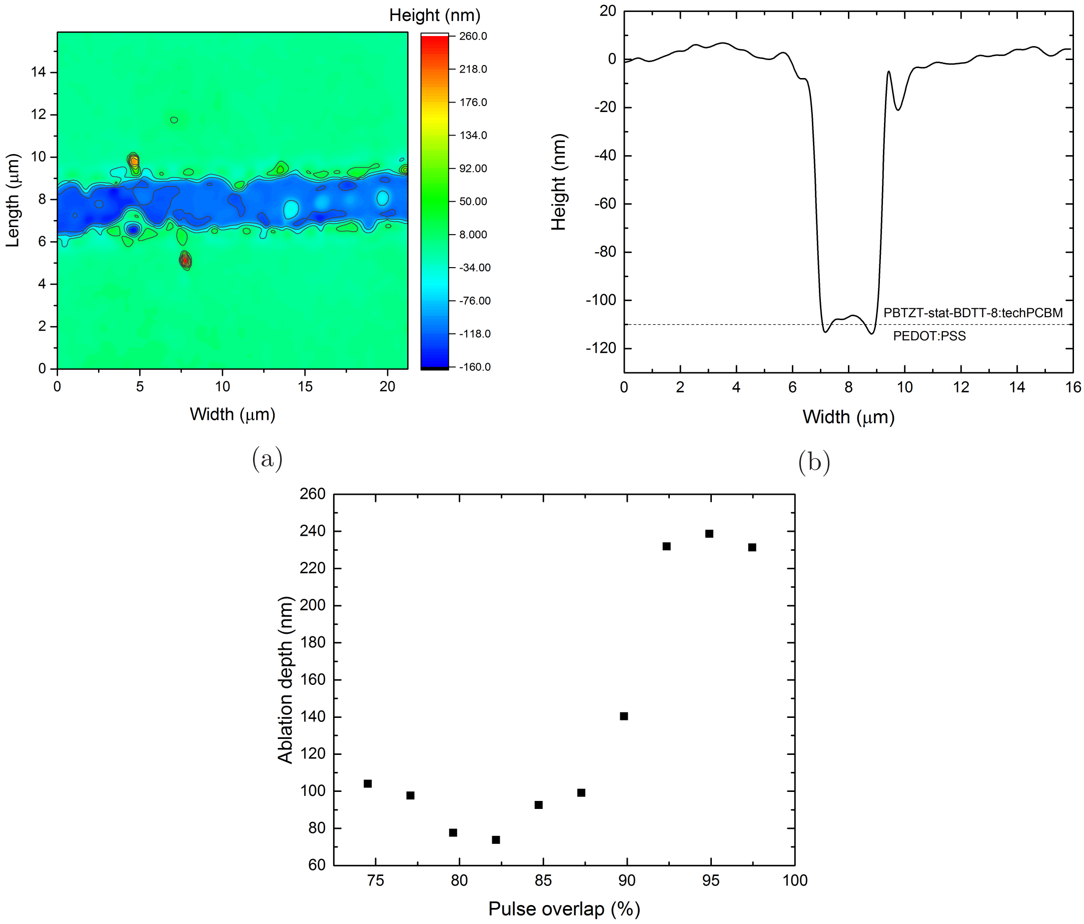

(a)

(b)

(c)

Figure 9.7: (a) and (b) 3D confocal image and profile for the laser-written line into PBTZT-stat-BDTT-8:techPCBM at $\lambda = 600\,\mathrm{nm}$, $F = 30\,\mathrm{mJ\,cm^{-2}}$ and pulse overlap of 70%. The line shows little damage to the PEDOT:PSS electrode below. Laser-written line width is < 5 µm. (c) Pulse overlap against ablation depth. A pulse overlap up to 88 % results in selective ablation of the PBTZT-stat-BDTT-8:techPCBM on top of PEDOT:PSS.

9.3.3 HYE (P3) structuring

In order to use HYE (P3) as top electrode, it is crucial to structure the HYE layer without damage to the bottom PEDOT:PSS electrode. The combination of PEDOT:PSS with silver nanowires has been previously structured. Guo et al. fabricated organic solar modules using PEDOT:PSS with silver nanowires as top electrode and ITO/IMI as bottom electrode.[137] They achieved a GFF = 95% with a PCE = 2.4% for a 3-cell solar module with an photoactive area of 0.1 cm^2.

Laser structuring at λ=600 nm

A fluence $F = 30\,\text{mJ cm}^{-2}$ which is below the threshold fluence $F_{\text{th}} = 50\,\text{mJ cm}^{-2}$ was selected. At this fluence the pulses do not cause ablation but melt the material. Figure 9.8a shows a processed line with a pulse overlap of 81%.

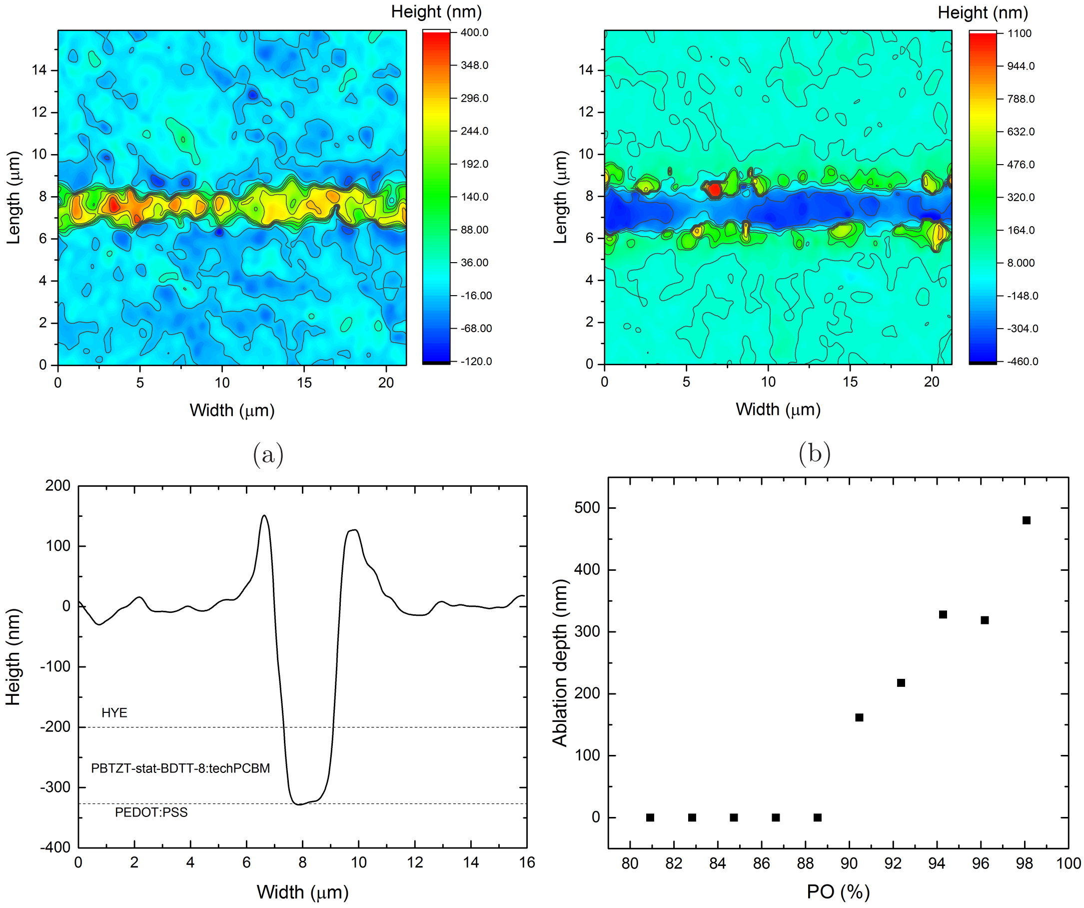

(a)

(b)

(c)

(d)

Figure 9.8: (a) 3D confocal image of the laser-written line into HYE at $\lambda = 600\,\text{nm}$ using $F = 30\,\text{mJ cm}^{-2}$ and a pulse overlap of 81 %. The line shows melting of the material. (b) and (c) 3D confocal image and profile for the structured line on HYE at $\lambda = 600\,\text{nm}$, $F = 30\,\text{mJ cm}^{-2}$ and pulse overlap of 94 %. The line shows little damage to the PEDOT:PSS layer below. Laser-written line width is $< 5\,\mu\text{m}$. (d) Pulse overlap against ablation depth. A pulse overlap below 91 % results in no ablation and just melting of the material. A pulse overlap above 98% results in complete removal of the PEDOT:PSS bottom electrode.

The laser created a melted line with a thickness of approx. 2.5 µm. The melted material results in an incubation effect that causes ablation of the material when the pulse overlap is increased. Figure 9.8b shows the laser-written line with a pulse overlap of 94 %. The ablation depth is approximately 350 nm showing the removal of the HYE top electrode together with the PBTZT-stat-BDTT-8:techPCBM absorption layer. Slight damage to the PEDOT:PSS might be present. The laser-written line width is < 5 µm (Figure 9.8c). If the pulse overlap is further increased the PEDOT:PSS layer is damaged. Figure 9.8d shows the relationship between the pulse overlap and the ablation depth, showing that when the pulse overlap is higher than 98 % the PEDOT:PSS layer is completely removed.

9.4 Solar module characterization

Using the structuring parameters described in the previous section, laser structured solar modules were built. Each solar module is composed of two solar cells. The J-V curves of solar cells and the structured solar module are shown in figure 9.9a. The devices were measured under illumination through the top and bottom electrode. The voltage of the solar modules was twice the voltage of the single solar cells. This demonstrates the working monolithic connection of the device. The individual devices showed a poor fill factor $FF = 48\%$, however the current density reduction on the solar module decreased the ohmic power losses leading to an improved fill factor of $FF = 53\%$ for the device illuminated through the top electrode. This is also true for the device under illumination through the bottom electrode side where the fill factor improved to $FF = 55\%$. The device exhibits a transparency of 20% with a PCE = 3.0% when illuminated through the bottom electrode. The device has a PCE = 2.6% under illumination through the top electrode. The reduction is due to the lower transmission of the top electrode when compared with the bottom electrode, leading to a reduction in the current density of the device. When comparing the efficiency of the solar module with the solar cell a slight decrease on the efficiency is present. This is due to a slight mismatch on the solar cells' area due to the manual alignment of the device on the workstation.

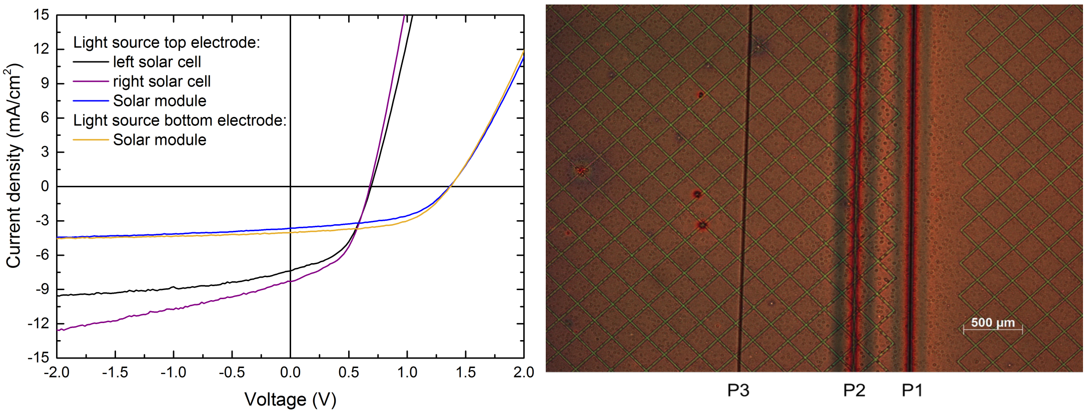

(a) (b)

Figure 9.9: (a) J-V curves of the single solar cells and solar module illuminated through either electrode. (b) Optical microscope image of the monolithic connection of the solar module.

Table 9.1: Key performance parameters for the semi-transparent solar module.

Device (illuminated through)	PCE (%)	FF (%)	J_{sc} (mA cm^{-2})	V_{oc} (V)
Left subcell (Top electrode)	2.5	48	7.4	0.69
Right subcell (Top electrode)	2.7	48	8.3	0.68
Module (Top electrode)	2.6	53	3.6	1.45
Module (Bottom electrode)	3.0	55	4.0	1.4

The inactive area width of the device is approximately 1 mm (Figure 9.9b) leading to a low GFF. The large structuring width was caused by the prestructuring of the silver grid that was done considering mechanical methods and no laser ablation. However, there is no technical limitation to achieve a higher GFF. The devices have an photoactive area larger than 1 cm^2, clearly showing the possibility to upscale the devices. The key parameters for the solar module are shown in table 9.1:

9.5 Discussion

In this chapter, the use of femtosecond lasers to selectively structure polymer layers has been demonstrated. All the polymer layers are coated from solution, using processes than can be transferable to industrial scale, such as doctor blading. The device exhibits a decent efficiency with PCE = 3 % and a transparency of 20 %. Notably, all three structuring steps were performed with structuring widths under 5 µm. Hence, the lines are invisible to the human eye. The solar modules have no visible features, like bus bars or large monolithic connections, making them ideal for window integration. The solar modules are also mechanically flexible, exhibiting most of the promising concepts behind OPV.

Selective ablation of the PEDOT:PSS electrode with low bulges under 150 µm was achieved. The pulse overlap plays an important role, as higher pulse overlap leads to lower ablation bulges. PEDOT:PSS may play a role in the future for other organic electronic devices, therefore achieving selective structuring with low bulges is crucial for future production. Selective ablation of PBTZT-stat-BDTT-8:techPCBM (P2) layer on top of PEDOT:PSS was also demonstrated. Selective ablation of thin film polymer layers is an important milestone in the way to roll-to-roll process of organic solar modules in the future. For HYE (P3) the layer was ablated without damaging the PEDOT:PSS bottom electrode below, ergo preserving the functionality of the device.

Ablation below the threshold fluence was demonstrated for PEDOT:PSS (P1) and HYE (P3). The initial pulses melt the material creating an incubation effect that increases the absorption leading to ablation of the layers. The use of lower fluences facilitates the selective ablation of the layers. The high overlap of picosecond pulses restricts the ablation into metal thin-films.[138] However, femtosecond pulses enhance ablation even with fluences below the threshold fluence. Further investigations are required on this topic to determine the mechanism that enhances or limits the ablation with pulse overlap.

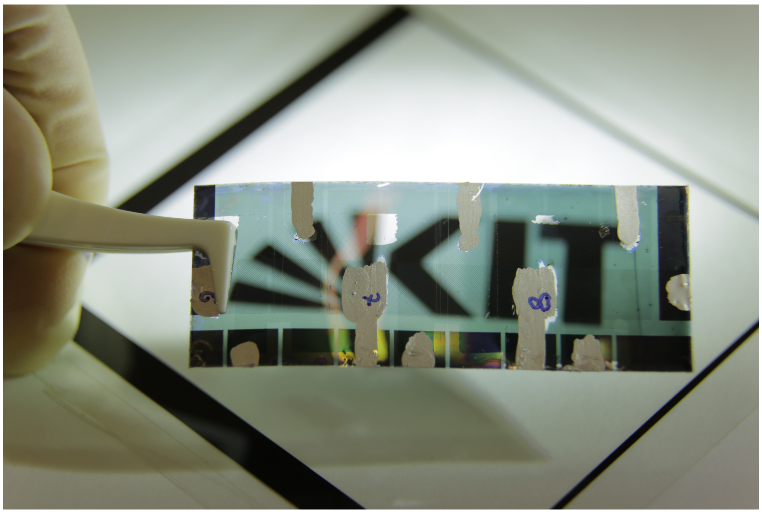

Figure 9.10: P1, P2 and P3 structuring steps on the semitransparent solar module. The solar module is all-solution on a flexible substrate. The small structured widths of P1, P2 and P3 lead to a homogeneous surface, ideal for window integration.

The threshold fluences follows the absorption spectrum at the studied wavelengths. This observation cannot be described with equations 5.9 and 5.10 where an increasing value of the threshold fluence with higher wavelengths is expected. The difference is due to the thin film nature of our layers and the semi-transparency of them, factors that were not considered for the previous equations. This matches the observations of chapter 7 for SuperYellow and ITO on top of glass. It also matches the observations of ITO on PET (chapter 6)
Although, devices using ITO as bottom electrode were previously demonstrated in this work in chapter 8. The selective ablation of polymer thin-films on top of other polymers is a bigger challenge as the working windows are severely reduced. Therefore, the working solar module all laser structured with ultrashort pulsed lasers is an important accomplished to fabricate these devices in the future.

10 All-solution opaque modules

In chapter 9 the construction of all-solution semi-transparent solar modules on flexible substrates was demonstrated. However, several applications require a rigid glass substrate. Koppitz et al. successfully demonstrated the construction of all-solution organic solar modules on glass using silver ink, as bottom electrode, and PEDOT:PSS with silver nanowires (HYE) as top electrode.[117] *The solar modules were structured using a lithography process for the silver electrode (P1), manually wiping the absorber layer (P2) and by tape patterning the HYE electrode (P3). These processes are not ideal for the future industrial fabrication of OPV.*

In this chapter structuring process to construct opaque all-solution solar modules on a glass substrate is optimized. Section 10.1 describes the silver ink used to apply the bottom electrode and the architecture used to construct the solar modules. In section 10.2 the threshold fluences for the different materials in the visible spectrum ($\lambda = 360\,\mathrm{nm}$ to $\lambda = 700\,\mathrm{nm}$) is reported. Section 10.3 summarizes the structuring process for P1, P2 and P3. Section 10.4 describes the characteristics of the laser structured solar modules. Finally, section 10.5 gives the conclusions for the chapter. This chapter was done as the master thesis of Tim Wünnemann. The experiments were prepared in collaboration with Manuel Koppitz.

10.1 Materials and device architecture

10.1.1 Materials

Some of the materials used for the construction of the opaque solar modules have already been described in previous chapters. ZnO was described in section 7.1 and is used as ETL. The electron donor PBTZT-stat-BDTT-8 and the electron acceptor techPCBM that formed the absorber layer were discussed in section 9.1. Finally, HYE used for the top electrode is also discussed in section 9.1.

Silver

The silver layer was processed from a metal-organic decomposition (MOD) silver ink. It has a sheet resistance of $R_\square = 0.9\,\Omega\,\square^{-1}$ at an optimized layer thickness of 165 nm. The root-mean-square roughness of the layer is approximately 3 nm. The low roughness is a necessary requirement as any spike on the silver layer might cause shunts, hence hindering the performance of the device. Silver has a work function of 4.3 eV.

Primer

A UV-curing primer (Polyprimer) was used before the application of the silver layer. It was diluted in 2-propanol (1:100). It can produce homogenous layers with thicknesses up to 15 µm and it is non-hygroscopic. The used layer has an approximate thickness of 10 nm.

10.1.2Device architecture and design

An inverted architecture was used to construct the solar modules. It requires top illumination as the silver bottom electrode is opaque. The first layer is a primer that flattens the substrate and improves the adhesion of the silver ink. The flat surface is important as any protuberance larger than 200 nm may translate on a silver peak and create shunts with the top electrode. The silver works as bottom electrode, with ZnO as ETL. The absorber layer is composed of the donor-acceptor mixture of PBTZT-stat-BDTT-8:techPCBM. HYE was used as top electrode.

Silver was structured as P1. ZnO was structured together with PBTZT-stat-BDTT-8:techPCBM as P2. HYE was structured as P3.

Figure 10.1b depicts the substrate design of the solar modules. The red area on the top electrode illustrates the photoactive area of the device. The photoactive area is approximately 1 cm^2 with some variations due to the manual structuring of the top electrode. Each substrate contains two solar modules. The design allows the measurement of the individual solar cells, marked on the design as solar cell A and solar cell B. Solar cell A can be measured using both sides of the silver electrode, accessing the top electrode through the monolithic connection. Solar cell B is accessed using the right side of the silver bottom electrode and the top electrode. The width of the solar module is reduced to prevent any pulse-to-pulse variation that might prevent the structuring of the devices.

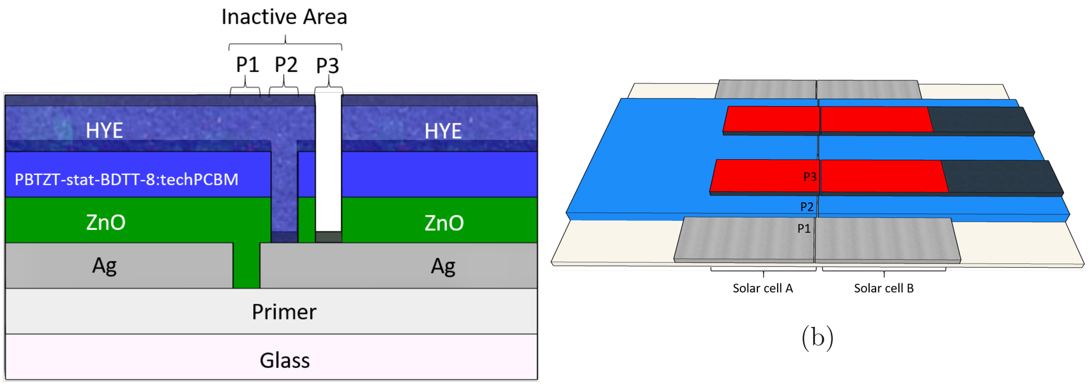

(b)

(a)

Figure 10.1: (a) Architecture of the all-solution opaque solar module showing the inactive area with the P1, P2 and P3 structuring steps. (b) All-solution opaque solar module design on glass with P1, P2 and P3 structuring steps.

10.2 Threshold fluences

The threshold fluences were determined for three different silver layer thicknesses, 50 nm, 100 nm and 150 nm. The 50 nm layer is semitransparent, enabling the manufacturing of semitransparent devices. The 150 nm is close to the optimized layer thickness of 165 nm. The 100 nm were chosen as an intermediate layer thickness for comparison purposes. The threshold fluences were determined using the Liu method (section 5.4) for the wavelengths $\lambda = 360$ nm, $\lambda = 410$ nm, $\lambda = 450$ nm, $\lambda = 550$ nm, $\lambda = 575$ nm $\lambda = 600$ nm, $\lambda = 650$ nm and $\lambda = 700$ nm. Figure 10.2a depicts the threshold fluences for the various layer thicknesses and wavelengths. The threshold fluence F_{th} increases with larger wavelengths for the three different silver thicknesses. It matches the expected linear relationship between the threshold fluence and the wavelength described in equation 5.10. It also matches the absorption spectrum of silver (Figure 7.3b) with decreasing absorption for longer wavelengths. The threshold fluence is also larger for thicker layers, with lower threshold fluences for the 50 nm layers than for the 150 nm layer. This can be explained with the larger amount of material that needs to be ablated.

Figure 10.2b shows the threshold fluences for PBTZT-stat-BDTT-8:techPCBM (P2) and HYE (P3) layers. There is no clear relationship between the threshold fluence and the wavelength for PBTZT-stat-BDTT-8:techPCBM (P2) and HYE (P3) layers. In section 9.2, the threshold fluences showed a relationship with the absorption spectrum, however, the device was semitransparent. Here, in the case of an opaque device, the silver reflects the laser pulses, changing the ablation. The threshold fluences of PBTZT-stat-BDTT-8:techPCBM (P2) and HYE (P3) do not follow equation 5.9 that predicts a linear relationship between the threshold fluence and the wavelength. It can be observed that the longer wavelengths should facilitate the selective ablation of PBTZT-stat-BDTT-8:techPCBM (P2) and HYE (P3) layers as the operating window is the largest among the studied wavelengths.

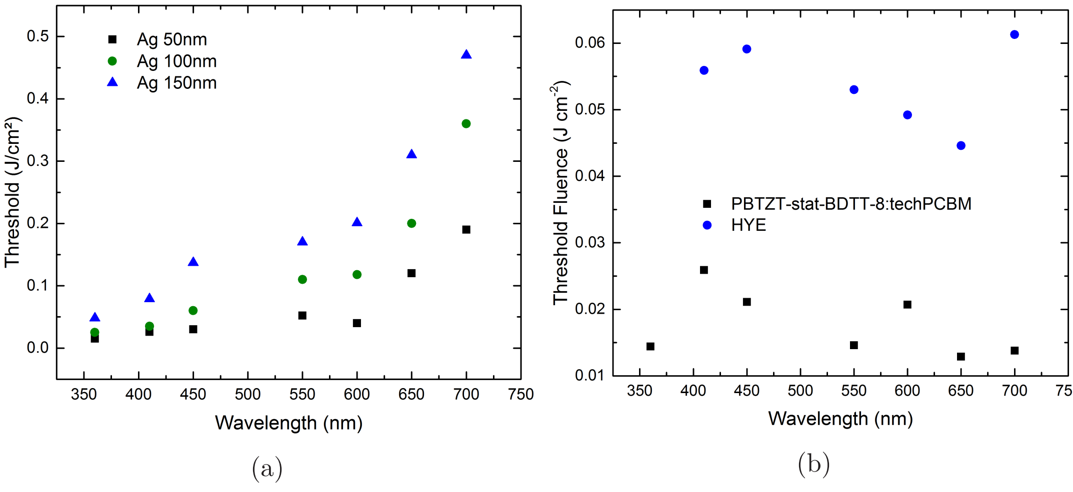

(a) (b)

Figure 10.2: (a) Threshold fluences for different silver layer thicknesses (P1). (b) Threshold fluences of PBTZT-stat-BDTT-8:techPCBM and HYE.

10.3 Structuring process optimization

10.3.1Silver layer structuring (P1)

The ablation process was optimized for 150 nm thick silver layers which is closest to the optimum thickness of 165 nm.

Laser structuring at λ=360 nm

The structuring process at $\lambda = 360\,\text{nm}$ was studied. A fluence $F = 60\,\text{mJ}\,\text{cm}^{-2}$ slightly higher than the threshold fluence $F_{\text{th}} = 55\,\text{mJ}\,\text{cm}^{-2}$ was tested. With a pulse overlap lower than 95 % clean ablation was not achieved with several spots where the silver was not completely removed. The ablation mechanism seems to change to stress ablation with a pulse overlap higher than 98% as some peeling is observed on the sample. Where the silver was completely removed, the silver shows no bulges (Figure 10.3b). However, this is not consistent along the whole laser-written line and the ablation shows high bulges larger than 1 µm. An example of the latter is marked by a red circle in figure 10.3a. The laser-written line width is approximate 9 µm.

Laser structuring at λ=450 nm

At $\lambda = 450\,\text{nm}$, a fluence $F = 150\,\text{mJ}\,\text{cm}^{-2}$ slightly above the threshold fluence $F_{\text{th}} = 140\,\text{mJ}\,\text{cm}^{-2}$ was investigated. The pulse overlap was evaluated from 74 % to 99 %. Although, in all the samples, bulges above 200 nm were found. It should be noticed that with higher pulse overlap, the height of the bulges increased. With a pulse overlap of 99 % a similar peeling effect to the one observed at $\lambda = 360\,\text{nm}$ occurred. Figure 10.4 shows the 3D confocal image and profile of the laser-written line with a pulse overlap of 74 %. Selective

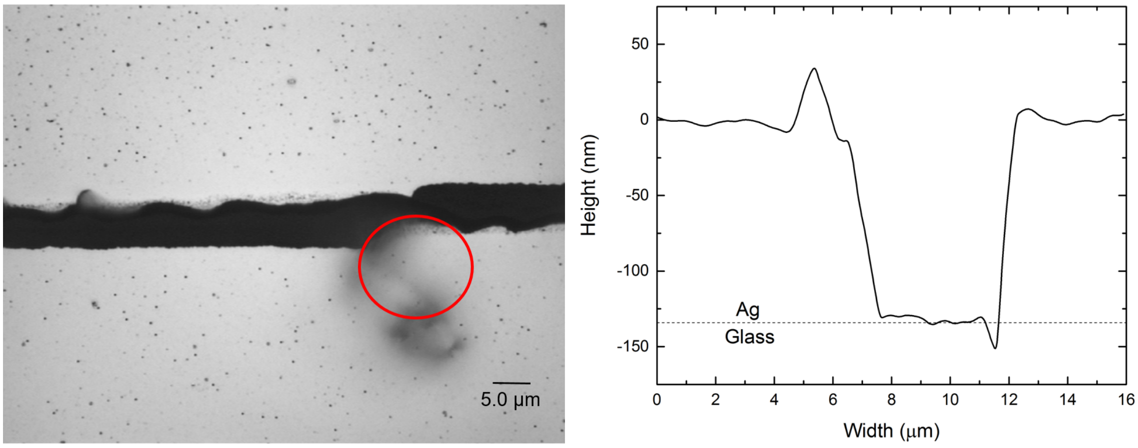

(a) (b)

Figure 10.3: (a) Optical microscope image and (b) confocal profile of the laser-written lines into silver at $\lambda = 360\,\text{nm}$, $F = 60\,\text{mJ}\,\text{cm}^{-2}$ and a pulse overlap of 98%. The peeled silver is encircled in red. On the places where the silver was completely removed the bulges are lower than 20 nm.

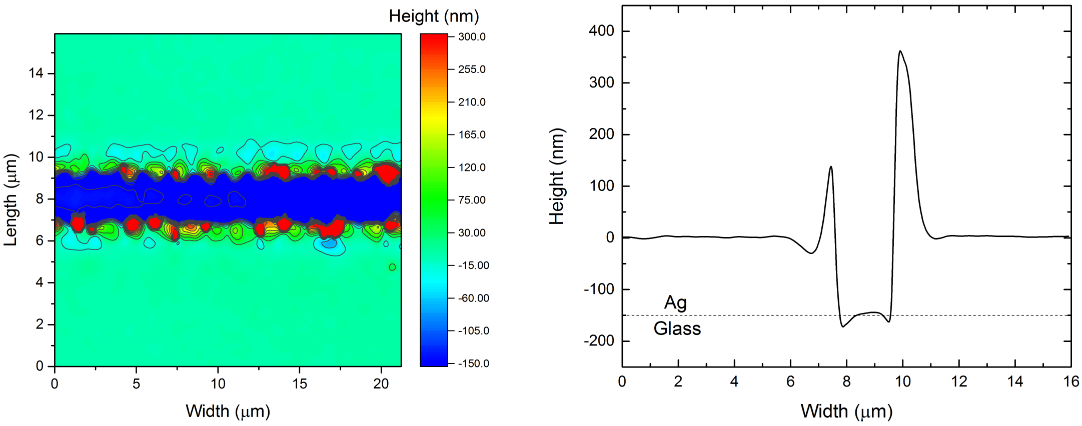

(a)

(b)

Figure 10.4: (a) 3D confocal image and (b)confocal profile of the laser-written lines into silver at $\lambda = 450$ nm, $F = 150$ mJ cm^{-2} and a pulse overlap of 74%. The laser-written line shows complete removal of the silver. The bulges are higher than 200 nm.

ablation was achieved with complete removal of the silver layer and no visible damage to the glass substrate underneath. The bulges have a height of more than 200 nm.

Laser structuring at λ=600 nm

At $\lambda = 600$ nm, a fluence $F = 210$ mJ cm^{-2}, slightly above the threshold fluence $F_{\mathrm{th}} = 200$ mJ cm,$^{-2}$ was evaluated. The pulse overlap was evaluated between 69 % and 99 %. The bulges are below 200 nm with selective ablation and negligible damage to the glass substrate below for a pulse overlap between 69% and 85%. Figure 10.5a shows the laser-written line with a pulse overlap of 75%. The silver was completely removed and the bulge height is under 200 nm. The laser-written line width is < 10 µm (Figure 10.5b). The ablation was also evaluated at $F = 330$ mJ cm^{-2} with similar results, bulges under 150 nm for a pulse overlap between 69% and 88% and complete removal of the silver layer. The laser-written line width is < 10 µm.

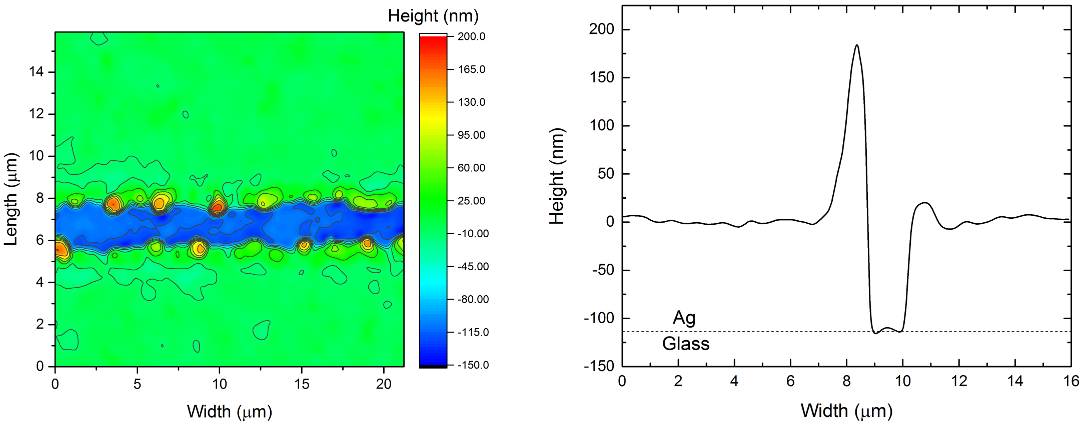

(a)

(b)

Figure 10.5: (a) 3D confocal image and (b) confocal profile of the laser-written lines into silver at $\lambda = 600$ nm, $F = 210$ mJ cm^{-2} and pulse overlap of 75%. The laser-written line shows bulges below 200 nm and a width below 10 µm. The silver layer is completely removed.

10.3.2PBTZT-stat-BDTT-8:techPCBM layer structuring (P2)

The silver electrode was structured at $\lambda = 600\,\text{nm}$, therefore, the structuring process of PBTZT-stat-BDTT-8:techPCBM layer (P2) was optimized at the same wavelength. Figure 10.6a shows the 3D confocal image for the laser-written line at $\lambda = 600\,\text{nm}$, $F = 60\,\text{mJ cm}^{-2}$ and pulse overlap of 82%. The used fluence was chosen well above the threshold fluence $F_{\text{th}} = 20\,\text{mJ cm}^{-2}$ to completely remove the ZnO and guarantee good contact between the top and bottom electrode. The laser-written line shows no visible damage to the silver layer below. The PBTZT-stat-BDTT-8:techPCBM and ZnO layers are completely removed. The laser-written line width is < 10µm as shown in Figure 10.6b. The laser-written line shows a bulge height above 1000 nm. However, the bulges in the photoactive layer do not hamper the performance of the devices. If the pulse overlap is increased to 95%, the PBTZT-stat-BDTT-8:techPCBM and ZnO layers are completely removed, but the silver layer shows some damage in the shape of bubbles (Figures 10.6c and 10.6d). The bubbles are caused by the melt of the silver originated from the increase in the pulse overlap.

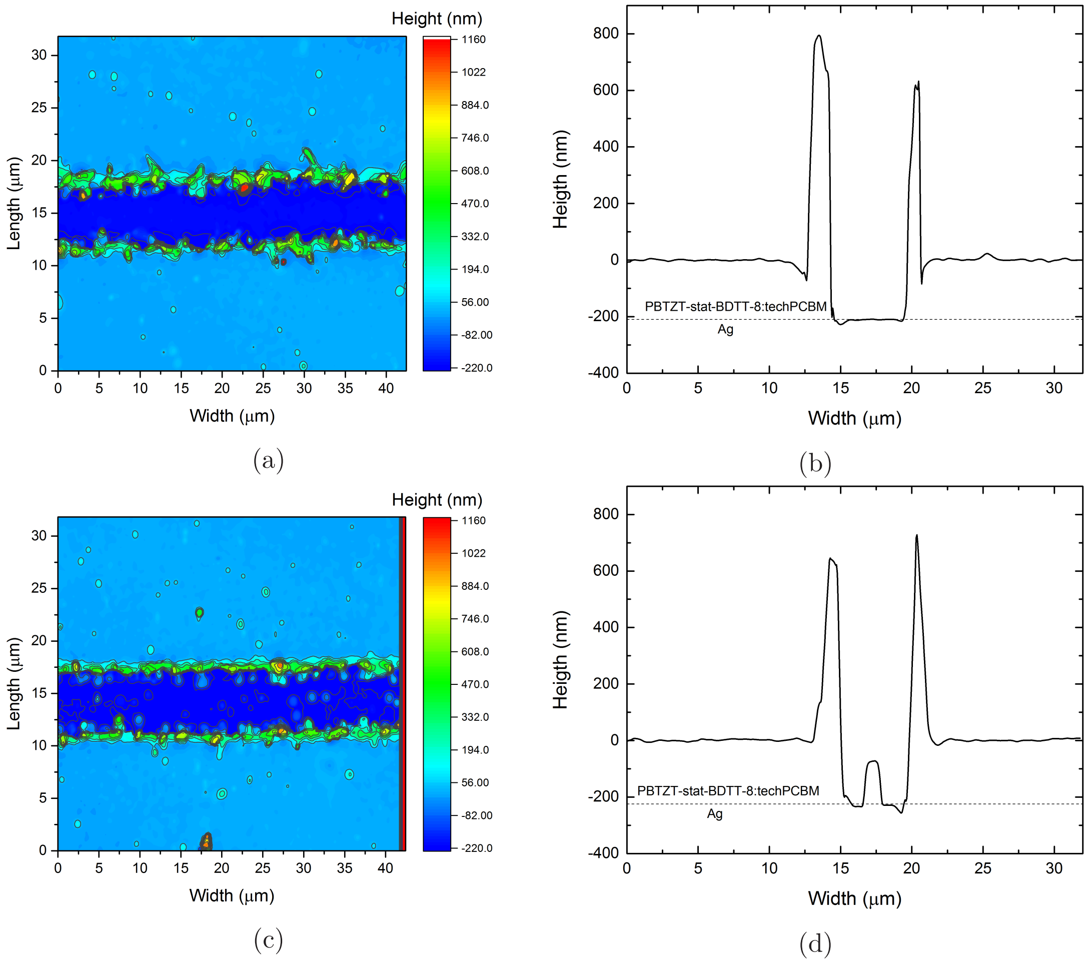

(a)

(b)

(c)

(d)

Figure 10.6: (a) and (b) Confocal 3D and profile images for laser-written lines into PBTZT-stat-BDTT-8:techPCBM (P2) at $\lambda = 600\,\text{nm}$, $F = 60\,\text{mJ cm}^{-2}$ and a pulse overlap of 82%. The silver electrode shows no visible damage. The bulges of the laser-written line are above 1000 nm, however, they do not play a role on the performance of the devices. The laser-written line width is ≤ 10 µm. (c) and (d) Confocal 3D and profile images for laser-written lines at $\lambda = 600\,\text{nm}$, $F = 60\,\text{mJ cm}^{-2}$ and pulse overlap of 95 %. The increase in pulse overlap leads to melting of the silver electrode.

10.3.3HYE (P3) structuring

The structuring process of HYE (P3) was optimized at $\lambda = 600\,\mathrm{nm}$. Figure 10.7 shows the laser-written line at $\lambda = 600\,\mathrm{nm}$, with $F = 80\,\mathrm{mJ\,cm^{-2}}$ and pulse overlap of 89 %. The used fluence is well above the threshold fluence $F_{\mathrm{th}} = 50\,\mathrm{mJ\,cm^{-2}}$. The high fluence combined with the high pulse overlap, guarantee the complete ablation of the HYE layer preventing any short on the top electrode. The ablation depth shows the complete removal of the PBTZT-stat-BDTT-8:techPCBM layer together with the HYE (Figure 10.7a). However, this does not hamper the performance of the devices. Importantly, the silver layer underneath shows no damage after the ablation. The laser-written line width is $< 10\,\mu\mathrm{m}$ (Figure 10.7b). An increase of the pulse overlap to 97% was also studied. The line shows complete removal of the HYE and PBTZT-stat-BDTT-8:techPCBM layers. The laser-written line width is $< 10\,\mu\mathrm{m}$. Similar to the case of PBTZT-stat-BDTT-8:techPCBM (P2) structuring, the silver layer is damaged forming bubbles (Figures 10.7c and 10.7d).

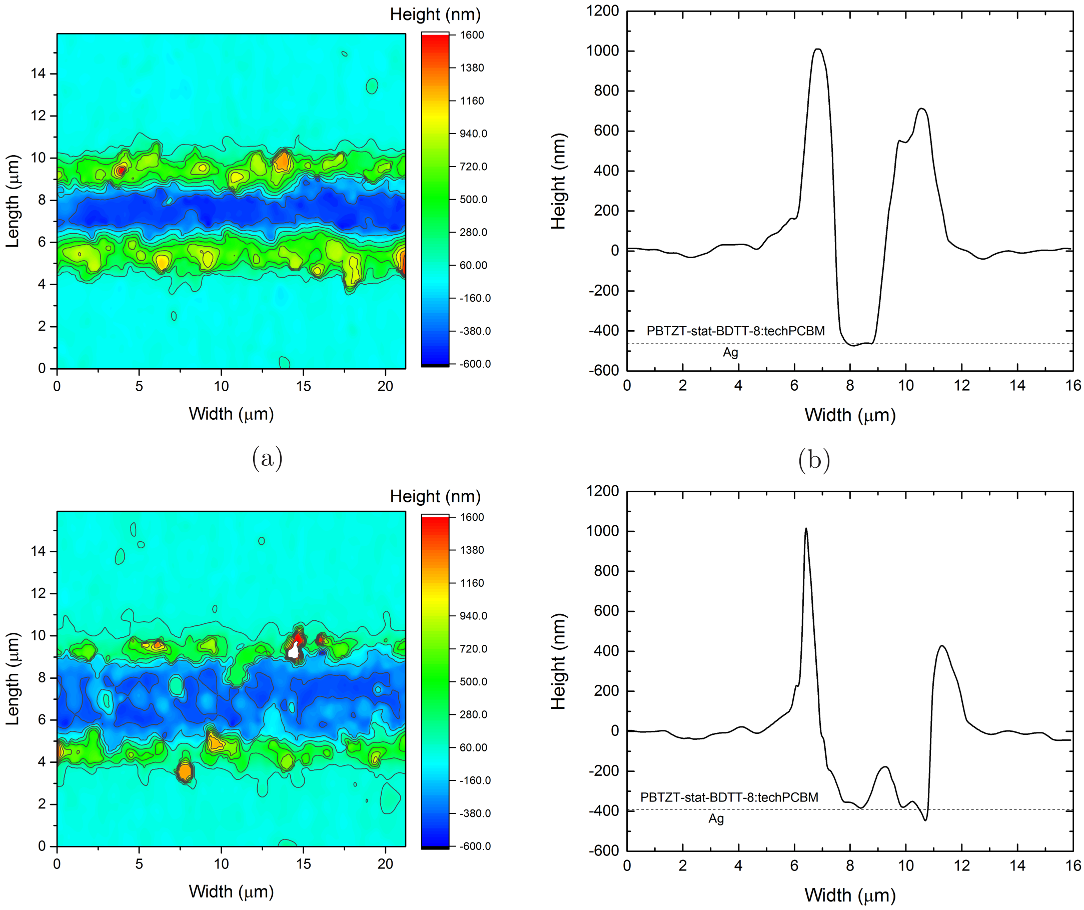

(a) (b)

(c) (d)

Figure 10.7: (a) and (b) confocal 3D image and profile for laser-written lines into HYE at $\lambda = 600\,\mathrm{nm}$, $F = 80\,\mathrm{mJ\,cm^{-2}}$ and pulse overlap of 89 %. The PBTZT-stat-BDTT-8:techPCBM layer is removed together with the HYE layer. The silver electrode shows no visible damage. The laser-written line width is $< 10\,\mu\mathrm{m}$. (c) and (d) confocal 3D image and profile for laser-written lines at $\lambda = 600\,\mathrm{nm}$, $F = 80\,\mathrm{mJ\,cm^{-2}}$ and pulse overlap of 97 %. The silver bottom electrode shows damage in the form of melt.

Table 10.1: Key performance parameters for the all-solution opaque solar modules.

Device	PCE (%)	FF (%)	J_{sc} (mA cm^{-2})	V_{oc} (V)	GFF (%)
Solar module A	3.7	46	6.0	1.34	95
Solar module B	2.6	42	4.9	1.30	99

10.4 Solar module characterization

First, solar modules were built using lithography to structure P1 and the laser to structure P2 and P3 (Solar module A). Solar module A exhibits a $V_{oc} = 1.34\,\mathrm{V}$ demonstrating a working monolithic connection. It has a total PCE = 3.7% and a $FF = 46\%$ considering just the photoactive area. Koppitz et al. reported $FF = 57\%$.[117] The FF reduction may stem from the laser structuring outside of the cleanroom environment. Solar modules using the laser to structure P1, P2 and P3 were built as well (Solar module B). Solar module B exhibits a $V_{oc} = 1.30\,\mathrm{V}$ which is slightly lower than solar module A. The device has a PCE = 2.6% and $FF = 42\%$. The lower FF is caused by the increase in shunts due to the laser structuring of P1. The short-circuit current density is lower of solar module B is lower $J_{sc} = 4.9\,\mathrm{mJ\,cm^{-2}}$ than the short-circuit current of solar module A $\mathrm{J_{sc}} = 6\,\mathrm{mJ\,cm^{-2}}$. Figure 10.8 shows the J-V curves of solar modules A and B. The key performance parameters of the devices are summarized in table 10.1. Both devices have a photoactive area of $1\,\mathrm{cm}^2$. Solar module A has an inactive area width of 1.05 mm (Figure 10.9a) and a GFF = 95%. Solar module B has an inactive area width of 100 µm (Figure 10.9b), leading to a GFF = 99%. Although the difference in GFF is just 4%, the inactive area in solar module B is 10 times smaller. The small difference in GFF originates from the design of the opaque solar module.

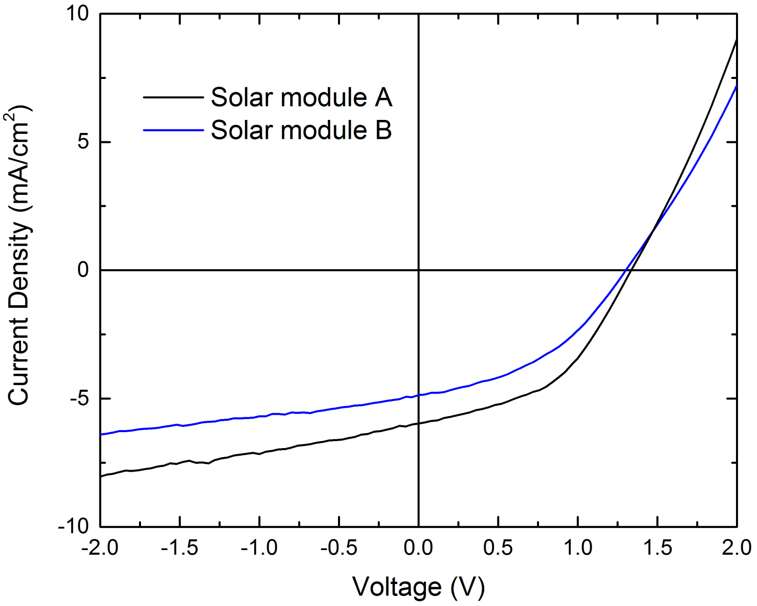

Figure 10.8: J-V curves for the laser structured opaque module. Solar module A, P1 was structured by lithography, P2, P3 were laser structured. Solar module B, P1, P2 and P3 were laser structured. The PCE of Solar Module A is higher.

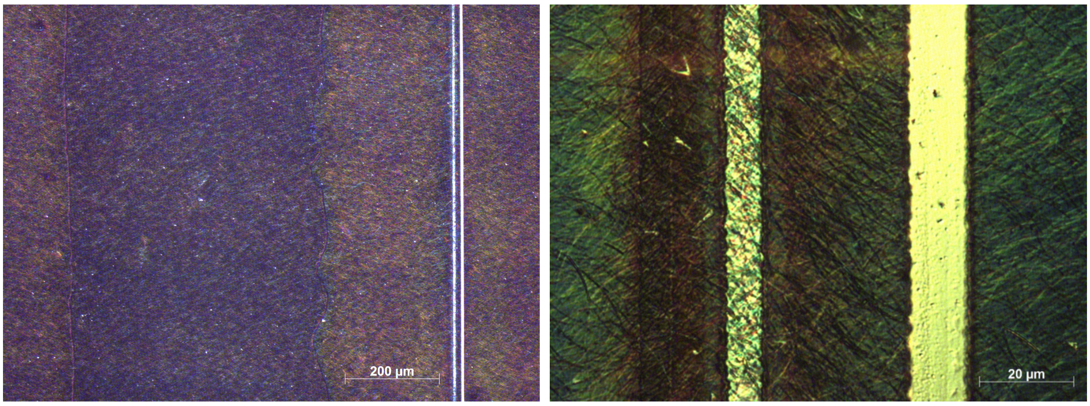

(a)

(b)

Figure 10.9: (a) Representative clipping of the inactive area width with P1 structured by lithography and P2, P3 laser structured. (b) Inactive area with P1,P2 and P3 laser structured. The laser structured inactive area is 10 times smaller.

10.5 Discussion

In this chapter the use of ultra short pulsed lasers to structure opaque all-solution organic solar modules was demonstrated. Initially the threshold fluences for wavelengths between $\lambda = 360\,\text{nm}$ and $\lambda = 750\,\text{nm}$ were determined. For the silver bottom electrode three different thicknesses 50 nm, 100 nm and 150 nm were evaluated. The threshold fluence increases with longer wavelengths for the three different silver layer thicknesses The linear increase of the threshold fluences with increasing wavelength matches what is stated in equation 5.10. It also matches the observations in chapter 7 for the evaporated silver as top electrode.

The threshold fluences do not have a clear dependence on the wavelength for PBTZT-stat-BDTT-8:techPCBM (P2) and HYE (P3). There is a clear change in the threshold fluence of the materials when compared to the values reported in section 9.2. The change may be attributed to the presence of the silver electrode that reflects the laser beam and changes the ablation conditions. The threshold fluences at different wavelengths do not follow equation 5.9 that predicts a linear increase of the threshold fluence with increasing wavelength.

On the structuring optimization for the silver (P1) it was demonstrated that, for the structuring at $\lambda = 360\,\text{nm}$ and $\lambda = 450\,\text{nm}$, the structuring led to high bulges that prevent the construction of devices as they will produce shorts. The shorts represent a big challenge to laser structure silver as bottom electrode. The structuring process at $\lambda = 360\,\text{nm}$ with high pulse overlap showed a peeling of the silver layer. The silver (P1) structuring process was optimized at $\lambda = 600\,\text{nm}$ were the confocal images show peaks below 200 nm, complete removal of the silver layer and a laser-written line width $< 10\,\mu\text{m}$. The optimum structuring of PBTZT-stat-BDTT-8:techPCBM (P2) and HYE (P3) was also optimized at $\lambda = 600\,\text{nm}$. The process produced clean ablation and no damage to the silver bottom electrode in both cases. Upon structoring of the HYE top electrodes (P3) the PBTZT-stat-BDTT-8:tech-PCBM was also removed. In both cases, a high pulse overlap damages the silver electrode forming bubbles.

Solar modules were constructed using the optimized laser structuring process at $\lambda = 600\,\mathrm{nm}$. The devices were compared structuring P1 with lithography and with the laser and P2 and P3 with the laser. The devices that were fully structured with the laser presented a slightly lower PCE due to a lower fill factor and short-circuit current densities. However, both devices presented lower fill factors when compared to the reported by Koppitz et al., possibly caused by exposition to an environment different to the cleanroom where the reported devices were manufactured. The fully laser structured solar modules exhibit a $\mathrm{GFF} = 99\,\%$ and the solar modules where P1 was structured by lithographic process exhibit a $\mathrm{GFF} = 95\,\%$. Although the difference is just $4\,\%$ the inactive area for the laser structured devices is 10 times smaller.

11 Conclusions and outlook

During this thesis the use of ultrashort pulsed lasers has been investigated for two different types of organic electronic devices, OLEDs and organic solar cells. An ultra fast parametric amplifier was used to explore ablation using different wavelengths. The structuring process is required to connect several devices in series through monolithic connections. This process limits the area of each individual device, decreasing the ohmic losses. Ultrashort pulsed lasers permit selective ablation and high resolution structures, therefore reducing the inactive area caused by the monolithic connection.

The first step was to investigate the ablation of ITO on top of PET (Chapter 6.1). ITO is one of the most common materials used as electrodes in organic electronics. The threshold fluences for both materials, ITO and PET, were investigated at different wavelengths between $\lambda = 360\,\text{nm}$ and $\lambda = 700\,\text{nm}$. A relationship between the threshold fluences and the ITO absorption was observed were higher absorption led to lower threshold fluence. It seems to be no relation between the threshold fluence and the absorption spectrum of PET, as the threshold fluence increases linearly with longer wavelengths. This follows the equations of Gamaly et al. that calculated a linear relationship between the threshold fluence and the wavelength.[71] Structuring was then explored by overlapping the pulses to write lines. Selective ablation at $\lambda = 360\,\text{nm}$ was not possible due to the close threshold fluences for both ITO and PET at this wavelength. Selective ablation was possible at $\lambda = 410\,\text{nm}$, however the bulges were higher than 250 nm. The increase in the pulse overlap led to lower bulges, however at $\lambda = 410\,\text{nm}$ this damaged the PET substrates below. At $\lambda = 550\,\text{nm}$ selective ablation with low bulges was achieved. The increase of the pulse overlap was possible due to the higher working space. At $\lambda = 650\,\text{nm}$ and $\lambda = 700\,\text{nm}$ the structured lines had even lower bulges and were selectively ablated. The laser-written lines with high resolution and low bulges enables the fabrication of mechanically flexible devices.

The monolithic connection of OLEDs was then explored (Chapter 7). The threshold fluences were investigated for the different materials, ITO, SuperYellow and silver, at five different wavelengths between $\lambda = 550\,\text{nm}$ and $\lambda = 750\,\text{nm}$. The calculated threshold fluences for ITO and SuperYellow remained almost constant through the investigated wavelengths, following their respective absorption. The silver threshold fluences increase with longer wavelengths. The absorption of silver may partially explain this, as it decreases with longer wavelengths. However the threshold fluence increases linearly with the wavelength was predicted by Gamaly et al.[71] The structuring parameters for P1, P2 and P3 were then found at $\lambda = 550\,\text{nm}$ and $\lambda = 750\,\text{nm}$. In both cases, the laser-written lines fulfill the fabrication requirements and allowed the construction of operational OLED modules. The OLED modules exhibit twice the onset voltage of the reference devices, showing a working monolithic connection. They have higher current and power efficiencies demonstrating the advantages of connecting them in series. Furthermore, the inactive area width was reduced to 45 µm, achieving a GFF = 99.6 %. The small inactive area facilitates the concealment of the monolithic connection.

The connection of solar cells in series through monolithic connections was then explored. Using an inverted architecture with ZnO as ETL and MoO_3 as HTL, and ITO and silver as bottom and top electrode single junction solar modules were built with three different absorber layers (PCDTBT:PC_{71}BM, nanoparticulate P3HT:IC_{60}BA and PTB7:PC_{71}BM). The solar modules exhibit comparable performance to the solar cells and in the case of the nanoparticulate P3HT:IC_{60}BA the fill factor of the device improved probably due to the reduced ohmic losses of the solar module. Solar tandem modules were also built, the devices exhibit a lower performance than the references built under nitrogen atmosphere. The decrease in performance is caused by the water adsorption during the laser processing. Finally, ultrashort pulse lasers were used to experimentally optimize the cell width of the solar modules. The results were proven by building a 6.5 cm^2 solar module composed of 8 solar cells. As predicted the device had 87 % of the maximum PCE. All the devices have inactive area widths in the range of 100 µm, allowing for GFF above 95 %.

Ultrashort pulsed laser structuring was tested in semitransparent all-solution modules on flexible PET substrate. PEDOT:PSS in combination with a silver grid was used as bottom electrode. PBTZT-stat-BDTT-8:techPCBM was the absorber layer and HYE the top electrode. The threshold fluences were determined for the wavelengths between $\lambda = 360$ nm and $\lambda = 700$ nm. A relationship between the absorption spectrum of PEDOT:PSS and the threshold fluences can be observed as the higher absorption led to reduction in the threshold fluences. Similarly, the threshold fluences of PBTZT-stat-BDTT-8:techPCBM and HYE exhibit a relationship with the absorption spectrum. Structured lines were optimized at $\lambda = 600$ nm, PEDOT:PSS was structured with little damage to the PET substrate below. The bulge height was under 100 nm. The pulse overlap clearly influences the height of the bulges, as with higher pulse overlap the bulges were reduced. The structured lines were optimized for PBTZT-stat-BDTT-8:techPCBM achieving selective ablation with no damage to the PEDOT:PSS layer below. The structuring of the HYE layer was done with no visible damage to the PEDOT:PSS layer. Solar modules were then constructed achieving PCE = 3.0 % with a transparency of 20 %. The semitransparent devices are featureless, all-solution processed on flexible devices fulfilling most of the promises of organic solar cells.

Finally, the ultrashort pulse laser was explored in opaque all-solution modules on glass. Silver was used as bottom electrode and PBTZT-stat-BDTT-8:techPCBM was the absorber layer and HYE the top electrode. The threshold fluences were also determined for the wavelengths between $\lambda = 360$ nm and $\lambda = 700$ nm. Similar to the case were silver was used as top electrode (OLED module), a linear increase with the wavelength is observed, following the work of Gamaly et al. However, this also matches the absorption spectrum of silver. Therefore, further research is necessary to attain a conclusion. Structured lines were optimized at

$\lambda = 600\,\mathrm{nm}$. The structured lines on silver exhibit bulges lower than 150 nm with selective ablation. PBTZT-stat-BDTT-8:techPCBM and HYE were also structured at $\lambda = 600\,\mathrm{nm}$ with no damage to the silver layer below. Solar modules were built with working monolithic connections as shown by voltage doubling of the devices. However, the solar modules exhibit a lower PCE than the ones built by Koppitz et al. using the same architecture.[117] The reason might be the exposition to an environment different to the cleanroom environment that might have contaminated the samples leading to larger shunts. The decrease in fill factor might have also been caused by shuts created by peaks on the structured lines on silver that were not observed during the optimization process. The device exhibit a GFF = 98 %.

Although the ablation of P3 produced high bulges in the devices, the performance of the constructed solar modules was not hampered. However, future investigation should be done on encapsulated devices. The encapsulation layer may lead to flattening of the bulges leading to contact on the top electrode and shortened devices. Future manufacturing of OPV needs to investigate this concern.

It can be concluded that ultrashort pulse lasers clearly offer several advantages when structuring organic electronic devices. Besides enabling the structuring of devices using different architectures as shown in this thesis, ultrashort pulsed lasers are suitable to be integrated on Roll-to-Roll processes. It should be mentioned that ultrashort pulsed lasers are also a technology that is still being improved. In the near future higher repetitions rates would be available allowing the possible printing of devices with higher speeds.

The threshold fluence for all the semitransparent thin-film layers showed a dependency with the absorption. In contrast the silver layers that were investigated showed a linear dependency with increasing wavelength. The results in this work could help further theoretical work to explain the interaction of femtosecond lasers with thin films at different wavelengths. Further studies can be done in the near infrared of the spectrum where materials like PEDOT:PSS have absorption bands. This might lead to the selective ablation of PEDOT:PSS on top of the absorber/emitting material possibly reducing the number of failed devices in a future industrial production.

Organic electronics have a promising future and ultrashort pulsed lasers facilitate the connection of them for up-scaling purposes with little active area losses. However, organic electronics, specially organic solar cells, face other challenges. Crystalline silicon photovoltaic is the dominant technology and it has a clear advantage in terms of PCE and lifetime. Although organic solar cells have some advantages over crystalline silicon like semi-transparency, low light performance and mechanical flexibility. Some of these advantages are not present when organic solar cells are compared with other technologies like CIGS or amorphous silicon. A realistic benchmark is required to determine the possible future applications of organic solar cells.

OLEDs are already a developed technology for the display market where they are taking an increasing market share. The use of lasers might help the large area lighting applications as the structuring lines can be concealed by the light.

A Single pulse threshold fluences

In the following tables, a summary of the single pulse threshold fluences of the different materials used in this work is given.

Table A.1: Threshold fluences between $\lambda = 360\,\mathrm{nm}$ and $\lambda = 750\,\mathrm{nm}$ of some materials used as electrodes in this work.

λ(nm)	ITO PET ($\mathrm{mJ\,cm^{-2}}$)	ITO glass ($\mathrm{mJ\,cm^{-2}}$)	PEDOT:PSS ($\mathrm{mJ\,cm^{-2}}$)	HYE-trans. ($\mathrm{mJ\,cm^{-2}}$)	Ag ev. ($\mathrm{mJ\,cm^{-2}}$)	Ag sol. - 50 nm ($\mathrm{mJ\,cm^{-2}}$)	Ag sol. - 100 nm ($\mathrm{mJ\,cm^{-2}}$)	Ag sol. - 150 nm ($\mathrm{mJ\,cm^{-2}}$)
360	41	-	110	34	-	15	25	48
410	169	-	155	33	-	26	35	79
450	163	-	120	50	-	30	60	137
500	170	-	130	40	-	-	-	-
550	169	173	58	36	235	52	110	170
600	159	183	61	50	280	40	118	201
650	162	172	68	42	333	120	200	310
700	160	191	76	64	395	190	360	470
750	-	180	-	-	490	-	-	-

Table A.2: Threshold fluences between $\lambda = 360\,\mathrm{nm}$ and $\lambda = 750\,\mathrm{nm}$ for some emitter/absorber materials used in this work.

λ(nm)	SuperYellow ($\mathrm{mJ\,cm^{-2}}$)	PBTZT-stat-BDTT-8:techPCBM-trans. ($\mathrm{mJ\,cm^{-2}}$)	PBTZT-stat-BDTT-8:techPCBM-opaque ($\mathrm{mJ\,cm^{-2}}$)
360	-	13	14
410	-	20	26
450	-	25	21
500	-	25	-
550	40	30	15
600	41	30	20
650	45	33	13
700	40	60	14
750	45	-	-

fluences for different materials

Bibliography

[1] R. Das, K. Ghaffarzadeh, C. Guillaume, and X. He. Printed, Organic & Flexible Electronics Forecasts, Players & Opportunies 2017-2027.

[2] T. Takatoshi. *OLED Display Fundamentals and Applications.* John Wiley & Sons, 2015.

[3] Daily mail Reporter. UFOs on the M4: Audi reveals bizarre 'swarm' light that turns the back of its cars into a pulsating screen, 2013.

[4] D. Evans. The Internet of Things - How the Next Evolution of the Internet is Changing Everything. Technical Report April, CISCO, 2011.

[5] IEA. More Data, Less Energy: Making Network Standby More Efficient in Billions of Connected Devices. Technical report, IEA, 2014.

[6] D. Landerer, D. Bahro, H. Röhm, M. Koppitz, A. Mertens, F. Manger, F. Denk, M. Heidinger, T. Windmann, and A. Colsmann. Solar Glasses: A Case Study on Semitransparent Organic Solar Cells for Self-Powered, Smart, Wearable Devices. *Energy Technology*, 5(11):1936–1945, 2017.

[7] O. Dupré, R. Vaillon, and M. A. Green. *Thermal Behavior of Photovoltaic Devices.* Springer, 2017.

[8] Deutsche Gesellschaft für Sonnenenergie (DGS). *Planning & Installing Photovoltaic Systems.* Earthscan, London, second edition, 2013.

[9] N. Bristow and J. Kettle. Outdoor performance of organic photovoltaics: Diurnal analysis, dependence on temperature, irradiance, and degradation. *Journal of Renewable and Sustainable Energy*, 7(1):013111, 2015.

[10] M. Nelson. German electricity was nearly 10 times dirtier than France's in 2016, feb 2017.

[11] Coherent. RAPID FX Coherent, 2017.

[12] A. Köhler and H. Bässler. Electronic and Optical Processes of Organic Semiconductors. In *Electronic Processes in Organic Semiconductors*, pages 193–305. Wiley-VCH Verlag GmbH & Co. KGaA, 2015.

[13] C. Tang. Two-layer organic photovoltaic cell. *Applied Physics Letters*, 48(2):183–185, 1986.

[14] B. Kippelen and J. Brédas. Organic photovoltaics. *Energy & Environmental Science*, 2(3):251, 2009.

[15] M. Eck and M. Krueger. Polymer – Nanocrystal Hybrid Solar Cells. In *Organic Photovoltaics: Materials, Device Physics, and Manufacturing Technologies*. Wiley-VCH Verlag GmbH & Co. KGaA, 2014.

[16] M. C. Scharber, D. Mühlbacher, M. Koppe, P. Denk, C. Waldauf, A. J. Heeger, and C. J. Brabec. Design rules for donors in bulk-heterojunction solar cells - Towards 10 % energy-conversion efficiency. *Advanced Materials*, 18(6):789–794, 2006.

[17] J. Brédas, D. Beljonne, V. Coropceanu, and J. Cornil. Charge-transfer and energy-transfer processes in pi-conjugated oligomers and polymers: a molecular picture. *Chemical reviews*, 104(11):4971–5004, 2004.

[18] R. Steim, F. R. Kogler, and C. J. Brabec. Interface materials for organic solar cells. *Journal of Materials Chemistry*, 20(13):2499, 2010.

[19] K. M. O. Malley, H. Yip, and A. K. Jen. Metal Oxide Interlayers for Polymer Solar Cells. In Christoph Brabec, Ullrich Scherf, and Vladimir Dyakonov, editors, *Organic Photovoltaics: Materials, Device Physics, and Manufacturing Technologies*, pages 319–341. Wiley-VCH Verlag GmbH & Co. KGaA, 2014.

[20] N. Grossiord, J. M. Kroon, R. Andriessen, and P. W .M. Blom. Degradation mechanisms in organic photovoltaic devices. *Organic Electronics*, 13(3):432–456, 2012.

[21] K. Kawano, R. Pacios, D. Poplavskyy, J. Nelson, D. C. Bradley, and J. R. Durrant. Degradation of organic solar cells due to air exposure. *Solar Energy Materials and Solar Cells*, 90(20):3520–3530, 2006.

[22] M. P. de Jong, L. J. van IJzendoorn, and M. J. A. de Voigt. Stability of the interface between indium-tin-oxide and poly(3,4-ethylenedioxythiophene)/poly(styrenesulfonate) in polymer light-emitting diodes. *Applied Physics Letters*, 77(14):2255–2257, 2000.

[23] K. Glaser, A. Pütz, J. Mescher, D. Bahro, and A. Colsmann. Organic Tandem Solar Cells. In *Organic Photovoltaics: Materials, Device Physics, and Manufacturing Technologies*, pages 445–464. Wiley-VCH Verlag GmbH & Co. KGaA, 2014.

[24] D. Bahro, M. Koppitz, A. Mertens, K. Glaser, J. Mescher, and A. Colsmann. Understanding the External Quantum Efficiency of Organic Homo-Tandem Solar Cells Utilizing a Three-Terminal Device Architecture. *Advanced Energy Materials*, 5(22):1–8, 2015.

[25] A. Hennhöfer. *Herstellung effizienter organischer Tandem-Solarmodule*. Bachelor thesis, Karlsruhe Institute of Technology, 2017.

[26] Y. Gao, V. M. Le Corre, A. Gaïtis, M. Neophytou, M. A. Hamid, K. Takanabe, and P. M. Beaujuge. Homo-Tandem Polymer Solar Cells with VOC >1.8 V for Efficient PV-Driven Water Splitting. *Advanced Materials*, 28(17):3366–3373, 2016.

[27] G. Dennler, M. C. Scharber, T. Ameri, P. Denk, K. Forberich, C. Waldauf, and C. J. Brabec. Design rules for donors in bulk-heterojunction tandem solar cells-towards 15 % energy-conversion efficiency. *Advanced Materials*, 20(3):579–583, 2008.

[28] Press release: Heliatek sets new Organic Photovoltaic world record efficiency of 13.2%, 2016.

[29] J. Nelson. *The Physics of Solar Cells*. Imperial College Press, London, England, 2003.

[30] F. C. Krebs. Polymer solar cell modules prepared using roll-to-roll methods: Knife-over-edge coating, slot-die coating and screen printing. *Solar Energy Materials and Solar Cells*, 93(4):465–475, 2009.

[31] F. C. Krebs, T. Tromholt, and M. Jørgensen. Upscaling of polymer solar cell fabrication using full roll-to-roll processing. *Nanoscale*, 2(6):873, 2010.

[32] M. Powalla, M. Cemernjak, J. Eberhardt, F. Kessler, R. Kniese, H. D. Mohring, and B. Dimmler. Large-area CIGS modules: Pilot line production and new developments. *Solar Energy Materials and Solar Cells*, 90(18-19):3158–3164, 2006.

[33] P. O. Westin, U. Zimmermann, M. Ruth, and M. Edoff. Next generation interconnective laser patterning of CIGS thin film modules. *Solar Energy Materials and Solar Cells*, 95(4):1062–1068, 2011.

[34] R. R. Arya and D. E. Carlson. Amorphous silicon PV module manufacturing at BP solar. *Progress in Photovoltaics: Research and Applications*, 10(2):69–76, 2002.

[35] G. D. Spyropoulos, P. Kubis, N. Li, D. Baran, L. Lucera, M. Salvador, T. Ameri, M. M. Voigt, F. C. Krebs, and C. J. Brabec. Flexible organic tandem solar modules with 6% efficiency: combining roll-to-roll compatible processing with high geometric fill factors. *Energy Environ. Sci.*, 7(10):3284–3290, 2014.

[36] S. Röttinger, B. Schwarz, S. Schäfer, R. Gauch, B. Zimmermann, and U. Würfel. Laser patterning of vacuum processed small molecular weight organic photovoltaics. *Solar Energy Materials and Solar Cells*, 154:35–41, 2016.

[37] P. Kubis, L. Lucera, F. Machui, G. Spyropoulos, J. Cordero, A. Frey, J. Kaschta, M. M. Voigt, G. J. Matt, E. Zeira, and C. J. Brabec. High precision processing of flexible P3HT/PCBM modules with geometric fill factor over 95%. *Organic Electronics: physics, materials, applications*, 15(10):2256–2263, 2014.

[38] Anna Köhler and H Bässler. Index. *Electronic Processes in Organic Semiconductors, An Introduction*, page 424, 2015.

[39] M. A. Baldo, M. E. Thompson, and S. R. Forrest. Phosphorescent materials for application to organic light emitting devices. *Pure and Applied Chemistry*, 71(11):2095–2106, 1999.

[40] E. F. Schubert. *Light-Emitting Diodes.* Cambridge University Press, Cambridge, United Kingdom, 2 edition edition, 2006.

[41] Unit of luminous intensity (candela).

[42] K. Neyts, M. Marescaux, A. U. Nieto, A. Elschner, W. Lövenich, K. Fehse, Qi. Huang, K. Walzer, and K. Leo. Inhomogeneous luminance in organic light emitting diodes related to electrode resistivity. *Journal of Applied Physics*, 100(11), 2006.

[43] M. G. Kang and L Jay Guo. Nanoimprinted Semitransparent Metal Electrodes and Their Application in Organic Light-Emitting Diodes. *Advanced Materials*, 19(10):1391–1396, 2007.

[44] M. Slawinski, M. Weingarten, M. Heuken, a. Vescan, and H. Kalisch. Investigation of large-area OLED devices with various grid geometries. *Organic Electronics: physics, materials, applications*, 14(10):2387–2391, 2013.

[45] J. Park, J. Lee, D. Shin, and S. Park. Luminance uniformity of large-area OLEDs with an auxiliary metal electrode. *IEEE/OSA Journal of Display Technology*, 5(8):306–311, 2009.

[46] C. Chang, J. Chen, S. Hwang, and C. H. Chen. Highly efficient white organic electroluminescent devices based on tandem architecture. *Applied Physics Letters*, 87(25):253501, 2005.

[47] C. W. Chen, Y. J. Lu, C. C. Wu, E. H. E. Wu, C. W. Chu, and Y. Yang. Effective connecting architecture for tandem organic light-emitting devices. *Applied Physics Letters*, 87(24):1–3, 2005.

[48] T. Lee, T. Noh, B. Choi, M. Kim, D. W. Shin, and J. Kido. High-efficiency stacked white organic light-emitting diodes. *Applied Physics Letters*, 92(4):043301, 2008.

[49] H. Sasabe and J. Kido. Development of high performance OLEDs for general lighting. *Journal of Materials Chemistry C*, 1:1699, 2013.

[50] S. Höfle, A. Schienle, C. Bernhard, M. Bruns, U. Lemmer, and A. Colsmann. Solution processed, white emitting tandem organic light-emitting diodes with inverted device architecture. *Advanced Materials*, 26(30):5155–5159, 2014.

[51] K. S. Yook, S. O. Jeon, S. Y. Min, J. Y. Lee, H. J. Yang, T. Noh, S. K. Kang, and T. W. Lee. Highly efficient p-i-n and tandem organic light-emitting devices using an air-stable and low-temperature-evaporable metal azide as an n-dopant. *Advanced Functional Materials*, 20(11):1797–1802, 2010.

[52] A. R. Duggal, D. F. Foust, W. F. Nealon, and C. M. Heller. Fault-tolerant, scalable organic light-emitting device architecture. *Applied Physics Letters*, 82(16):2580–2582, 2003.

[53] F. C. Krebs. Fabrication and processing of polymer solar cells: A review of printing and coating techniques. *Solar Energy Materials and Solar Cells*, 93(4):394–412, 2009.

[54] F. Völz. *Herstellung und Charakterisierung organischer Mini-Solarmodule*. Bachelor thesis, Karlsruhe Institute of Technology, 2014.

[55] L. D. Landau and V. G. Levich. Dragging of a liquid by a moving plate. *Acta Physicochimica U.R.S.S.*, 17:42–54, 1942.

[56] Rolf Theodor Borlinghaus. Confocal Microscopy. In *The White Confocal*, pages 47–66. Springer, 2017.

[57] M. Hochberg. *Optoelectronic and surface properties of BODIPY solar cells (MSc Thesis)*. PhD thesis, Karlsruhe Institute of Technology, 2014.

[58] T. Leonhard. *Charakterisierung von Blei-Perowskitschichten mittels Rasterkraftmikroskopie*. Master thesis, Karlsruhe Institute of Technology, 2016.

[59] Operator's manual Libra Ultrafast Amplifier Laser System.

[60] F. Träger. *Springer Handbook of lasers and optics*. Springer, Kassel, Germany, 2007.

[61] M. Eichhorn. *Laser Physics*. Springer, Cambridge, United Kingdom, 2014.

[62] K. F. Renk. *Basics of Laser Physics, Graduate Texts in Physics*. Springer, second edition, 2012.

[63] W. Koechner. 8. Q-Switching. In *Solid-State Laser Engineering*, chapter 8. Q-Switc, pages 488–533. Springer, Round Hill, U.S.A., sixth edit edition, 2006.

[64] K. F. Renk. *Basics of Laser Physics, Graduate Texts in Physics*. Springer, Regensburg, Germany, second edition, 2012.

[65] W. Koechner. 9 . Mode Locking. In *Solid-State Laser Engineering*, pages 534–586. Springer, Round Hill, U.S.A., 6th edition, 2006.

[66] R. W. Boyd. *Nonlinear optics*. Elsevier, third edit edition, 2010.

[67] D. Bäuerle. *Laser Processing and Chemistry.* Springer, Linz, Austria, fourth edi edition, 2011.

[68] H. Hügel and T. Graf. *Laser in der Fertigung.* Vieweg+Teubner, Stuttgart, Germany, 2nd editio edition, 2009.

[69] B. Neuenschwander, B. Jaeggi, M. Schmid, A. Dommann, A. Neels, T. Bandi, and Guido Hennig. Factors controlling the incubation in the application of ps laser pulses on copper and iron surfaces. *Laser Applications in Microelectronic and Optoelectronic Manufacturing (LAMOM) XVIII*, 8607:86070D, 2013.

[70] K. Sugioka, M. Michael, and A. Piqué. *Laser Precision Microfabrication.* Springer, Saitama, Japan, first edit edition, 2010.

[71] E. G. Gamaly, A. V. Rode, B. Luther-Davies, and V. T. Tikhonchuk. Ablation of solids by femtosecond lasers: Ablation mechanism and ablation thresholds for metals and dielectrics. *Physics of Plasmas*, 9(3):949, 2002.

[72] M. J. Liu. Simple technique for measurements of pulsed Gaussian-beam spot sizes. *Opt. Lett.*, 7(5):196–198, 1982.

[73] A. Ben-Yakar and R. L. Byer. Femtosecond laser ablation properties of borosilicate glass. *Journal of Applied Physics*, 96(9):5316–5323, 2004.

[74] T. L. Breen, P. M. Fryer, R. W. Nunes, and M. E. Rothwell. Patterning Indium Tin Oxide and Indium Zinc Oxide Using Microcontact Printing and Wet Etching. *Society*, 18(24):194–197, 2002.

[75] O. Ourida, B. M. Said, T. Thierry, and S. Martin. ITO Etched by Photolithography Used in the Fabrication of Flexible Organic Solar Cells with PET Substrates. *Journal of Energy and Power Engineering*, 8:107–111, 2014.

[76] H. W. Choi, Dave F. Farson, J. Bovatsek, A. Arai, and D. Ashkenasi. Direct-write patterning of indium-tin-oxide film by high pulse repetition frequency femtosecond laser ablation. *Applied optics*, 46(23):5792–5799, 2007.

[77] G. Raciukaitis, M. Brikas, M. Gedvilas, and T. Rakickas. Patterning of indium-tin oxide on glass with picosecond lasers. *Applied Surface Science*, 253(15):6570–6574, 2007.

[78] S. Krause, P. T. Miclea, S. Schweizer, and G. Seifert. Optimized scribing of TCO layers on glass by selective femtosecond laser ablation. *Conference Record of the IEEE Photovoltaic Specialists Conference*, 40601:2432–2435, 2013.

[79] H. Tsai, H. Yang, C. Pan, and M. Chou. Laser Patterning Indium Tin Oxide (ITO) Coated on PET Substrate. *SPIE proceedings*, 4230:156–163, 2000.

[80] C. McDonnell, D. Milne, C. Prieto, H. Chan, D. Rostohar, and G. M. O'Connor. Laser patterning of very thin indium tin oxide thin films on PET substrates. *Applied Surface Science*, 359:567–575, 2015.

[81] O. Ghandour. Excimer ablation of ITO on flexible substrates for large format display applications. *Proceedings of SPIE*, 4637:90–101, 2002.

[82] S. Xiao, S. A. Fernandes, and A. Ostendorf. Selective patterning of ITO on flexible PET Substrate by 1064nm picosecond Laser. *Physics Procedia*, 12(PART 2):125–132, 2011.

[83] K. Hirschfelder, M. Schaefer, and A. Gillner. Ultrashort-pulsed laser processing and solution based coating in roll- to-roll manufacturing of organic photovoltaics. *SPIE proceedings*, 9567:1–7, 2015.

[84] Kr. Neyts, A. Real, M. Marescaux, S. Mladenovski, and J. Beeckman. Conductor grid optimization for luminance loss reduction in organic light emitting diodes. *Journal of Applied Physics*, 103(9), 2008.

[85] S. Harkema, S. Mennema, M. Barink, H. Rooms, Joanne S. Wilson, Ton van Mol, and Dirk Bollen. Large area ITO-free flexible white OLEDs with Orgacon PEDOT:PSS and printed metal shunting lines. *Proceedings of SPIE*, 7415(0):74150T–74150T–8, 2009.

[86] J. Park, J. Lee, and Y. Y. Noh. Optical and thermal properties of large-area OLED lightings with metallic grids. *Organic Electronics: physics, materials, applications*, 13(1):184–194, 2012.

[87] J. Fragoso, S. Höfle, M. Zhang, J. Dlugosch, T. Friedrich, S. Wagner, and A. Colsmann. OLED Luminaires: Device Arrays with 99.6% Geometric Fill Factor Structured by Femtosecond Laser Ablation. *ACS Applied Materials and Interfaces*, 9(43):37898–37904, 2017.

[88] H. J. Bolink, E. Coronado, J. Orozco, and M. Sessolo. Efficient polymer light-emitting diode using air-stable metal oxides as electrodes. *Advanced Materials*, 21(1):79–82, 2009.

[89] H. J. Bolink, E. Coronado, D. Repetto, and M. Sessolo. Air stable hybrid organic-inorganic light emitting diodes using ZnO as the cathode. *Applied Physics Letters*, 91(22):2005–2008, 2007.

[90] S. Höfle, A. Schienle, M. Bruns, U. Lemmer, and A. Colsmann. Enhanced electron injection into inverted polymer light-emitting diodes by combined solution-processed zinc oxide/polyethylenimine interlayers. *Advanced Materials*, 26(17):2750–2754, 2014.

[91] Yi. Zhou, C. Fuentes-hernandez, J. Shim, J. Meyer, A. J. Giordano, H. Li, P. Winget, T. Papadopoulos, H. Cheun, J. Kim, M. Fenoll, A. Dindar, W. Haske, E. Najafabadi, T. M. Khan, H. Sojoudi, S. Barlow, S. Graham, J. Brédas, S. R. Marder, A. Kahn, and B. Kippelen. for Organic Electronics. *Science*, 873(April):327–332, 2012.

[92] M. Zhang. *Fully Solution Processed Transparent Organic Light Emitting Diodes.* Master thesis, Karlsruhe Institute of Technology, 2013.

[93] H. You, Y. Dai, Z. Zhang, and D. Ma. Improved performances of organic light-emitting diodes with metal oxide as anode buffer. *Journal of Applied Physics*, 101(2):2005–2008, 2007.

[94] L. Lucera, F. Machui, P. Kubis, H. D. Schmidt, J. Adams, S. Strohm, T. Ahmad, K. Forberich, H.-J. Egelhaaf, and C. J. Brabec. Highly efficient, large area, roll coated flexible and rigid OPV modules with geometric fill factors up to 98.5% processed with commercially available materials. *Energy Environ. Sci.*, 9(1):89–94, 2016.

[95] M. Seeland and H. Hoppe. Comparison of distributed vs. lumped series resistance modeling of thin-film solar cells and modules: Influence on the geometry-dependent efficiency. *Phys. Status Solidi A*, 212(9):1991–2000, 2015.

[96] N. Blouin, A. Michaud, and M. Leclerc. A low-bandgap poly(2,7-carbazole) derivative for use in high-performance solar cells. *Advanced Materials*, 19(17):2295–2300, 2007.

[97] S. Beaupré and M. Leclerc. PCDTBT: en route for low cost plastic solar cells. *Journal of Materials Chemistry A*, 1:11097–11105, 2013.

[98] C. H. Peters, I. T. Sachs-Q., J. P. Kastrop, S. Beaupré, M. Leclerc, and M. D. McGehee. High efficiency polymer solar cells with long operating lifetimes. *Advanced Energy Materials*, 1(4):491–494, 2011.

[99] A. T. Kleinschmidt, S.E. Root, and D. J. Lipomi. Poly(3-hexylthiophene) (P3HT): fruit fly or outlier in organic solar cell research? *J. Mater. Chem. A*, 10(c):93–116, 2017.

[100] G. J. Zhao, Y. J. He, and Y. Li. 6.5% efficiency of polymer solar cells based on poly(3-hexylthiophene) and indene-C60 bisadduct by device optimization. *Advanced Materials*, 22(39):4355–4358, 2010.

[101] Ji. Hou, H. H. Chen, S. Zhang, R. I. Chen, Y. Yang, Y. Wu, and G. Li. Synthesis of a low band gap polymer and its application in highly efficient polymer solar cells. *Journal of the American Chemical Society*, 131(43):15586–15587, 2009.

[102] Z. He, C. Zhong, S. Su, M. Xu, H. Wu, and Y. Cao. Enhanced Power-Conversion Efficiency in Polymer Solar Cells Using an Inverted Device Structure Enhanced power-conversion efficiency in polymer solar cells using an inverted device structure. *Nature Photonics*, 6(9):591–595, 2012.

[103] M. M. Wienk, J. M. Kroon, W. J. H. Verhees, J. Knol, J. C. Hummelen, P. A. van Hal, and R. A. J. Janssen. Efficient Methano[70]fullerene/MDMO-PPV Bulk Heterojunction Photovoltaic Cells. *Angewandte Chemie International Edition*, 42(29):3371–3375, 2003.

[104] H. Youjun, C. Hsiang-Yu, H. Jianhui, and L. Yongfang. 2010_Indene−C60 Bisadduct - A New Acceptor for High-Performance Polymer Solar Cells_KW.pdf. *Journal of the American Chemical Society*, 132(4):1377–1382, 2010.

[105] K. Mazzio and C. K. Luscombe. The future of organic photovoltaics. *Chem. Soc. Rev.*, 44(1):78–90, 2014.

[106] A. Elschner, S. Kirchmeyer, W. Lovenich, W. Merker, and R. Knud. *PEDOT: Principles and Applications of an Intrinsically Conductive Polymer.* CRC Press, 2010.

[107] A. M. Nardes, M. Kemerink, M. M. de Kok, E. Vinken, K. Maturova, and R. A J Janssen. Conductivity, work function, and environmental stability of PEDOT:PSS thin films treated with sorbitol. *Organic Electronics: physics, materials, applications*, 9(5):727–734, 2008.

[108] S. Gärtner, M. Christmann, S. Sankaran, H. Röhm, E. M. Prinz, F. Penth, A. Pütz, A. E. Türeli, B. Penth, B. Baumstümmler, and A. Colsmann. Eco-friendly fabrication of 4% efficient organic solar cells from surfactant-free P3HT:ICBA nanoparticle dispersions. *Advanced Materials*, pages 6653–6657, 2014.

[109] S. Sankaran, K. Glaser, S. Gärtner, T. Rödlmeier, K. Sudau, G. Hernandez-Sosa, and A. Colsmann. Fabrication of polymer solar cells from organic nanoparticle dispersions by doctor blading or ink-jet printing. *Organic Electronics: physics, materials, applications*, 28:118–122, 2016.

[110] J. Chung, S. Han, D. Lee, S. Ahn, C. P. Grigoropoulos, J. Moon, and S. H. Ko. Nanosecond laser ablation of silver nanoparticle film. *Optical Engineering*, 52(2):021010–1, 2013.

[111] D. Huang, Y. Li, Z. Xu, S. Zhao, L. Zhao, and J. Zhao. Enhanced performance and morphological evolution of PTB7:PC71BM polymer solar cells by using solvent mixtures with different additives. *Physical chemistry chemical physics : PCCP*, 17(12):8053–60, 2015.

[112] K. Kawano, R. Pacios, D. Poplavskyy, J. Nelson, D. C Bradley, and J. R. Durrant. Degradation of organic solar cells due to air exposure. *Solar Energy Materials and Solar Cells*, 90(20):3520–3530, 2006.

[113] K. Glaser. *Hochskalierung und Defektcharakterisierung von organische Solarzellen.* Phd thesis, Karlsruhe Institute of Technology, 2017.

[114] F. Guo, N. Li, V. V. Radmilović, V. R. Radmilović, M. Turbiez, Er. Spiecker, K. Forberich, and C. J. Brabec. Fully printed organic tandem solar cells using solution-processed silver nanowires and opaque silver as charge collecting electrodes. *Energy Environ. Sci.*, 8(6):1690–1697, 2015.

[115] J. Krantz, K. Forberich, P. Kubis, F. Machui, J. Min, T. Stubhan, and C. J. Brabec. Printing high performance reflective electrodes for organic solar cells. *Organic Electronics*, 17:334–339, 2015.

[116] F. Nickel, T. Haas, E. Wegner, D. Bahro, S. Salehin, O. Kraft, P. A. Gruber, and A. Colsmann. Mechanically robust, ITO-free, 4.8% efficient, all-solution processed organic solar cells on flexible PET foil. *Solar Energy Materials and Solar Cells*, 130:317–321, 2014.

[117] M. Koppitz, N. Hesse, D. Landerer, L. GrafvonReventlow, E. Wegner, J. Czolk, and A. Colsmann. Organic Solar Modules: Fully Doctor Bladed on Glass in Air. *Energy Technology*, pages 1105–1111, 2017.

[118] C. Chen, L. Dou, J. Gao, W. Chang, G. Li, and Y. Yang. High-performance semi-transparent polymer solar cells possessing tandem structures. *Energy & Environmental Science*, 6(9):2714–2720, 2013.

[119] M. Song, D. S. You, K. Lim, S. Park, S. Jung, C. S. Kim, D. H. Kim, D. G. Kim, Jo. K. Kim, J. Park, Y. C. Kang, J. Heo, S. H. Jin, J. H. Park, and J. W. Kang. Highly efficient and bendable organic solar cells with solution-processed silver nanowire electrodes. *Advanced Functional Materials*, 23(34):4177–4184, 2013.

[120] F. Guo, Xi. Zhu, K. Forberich, J. Krantz, T. Stubhan, M. Salinas, M. Halik, S. Spallek, B. Butz, E. Spiecker, T. Ameri, N. Li, P. Kubis, D. M. Guldi, G. J. Matt, and C. J. Brabec. ITO-free and fully solution-processed semitransparent organic solar cells with high fill factors. *Advanced Energy Materials*, 3(8):1062–1067, 2013.

[121] J. H. Yim, S. Y. Joe, C. Pang, K. M. Lee, H. Jeong, J.Y. Park, Y. H. Ahn, J. C. De Mello, and S. Lee. Fully solution-processed semitransparent organic solar cells with a silver nanowire cathode and a conducting polymer anode. *ACS Nano*, 8(3):2857–2863, 2014.

[122] F. Guo, P. Kubis, T. Stubhan, N. Li, D. Baran, T. Przybilla, E. Spiecker, K. Forberich, and C. J. Brabec. Fully solution-processing route toward highly transparent polymer solar cells. *ACS Applied Materials and Interfaces*, 6(20):18251–18257, 2014.

[123] Y. Xia, K. Sun, and J. Ouyang. Solution-processed metallic conducting polymer films as transparent electrode of optoelectronic devices. *Advanced Materials*, 24(18):2436–2440, 2012.

[124] M. Zhang, S. Höfle, J. Czolk, A. Mertens, and A. Colsmann. All-solution processed transparent organic light emitting diodes. *Nanoscale*, 7:20009–20014, 2015.

[125] M. Song, H. Kim, C. S. Kim, J. Jeong, C. Cho, J. Lee, S. Jin, D. Choi, and D. Kim. ITO-free highly bendable and efficient organic solar cells with Ag nanomesh/ZnO hybrid electrodes. *J. Mater. Chem. A*, 3(1):65–70, 2014.

[126] M. Reinhard, R. Eckstein, A. Slobodskyy, U. Lemmer, and A. Colsmann. Solution-processed polymer – silver nanowire top electrodes for inverted semi-transparent solar cells. *Organic Electronics*, 14(1):273–277, 2013.

[127] M. Helgesen, J. E. Carlé, and F. C. Krebs. Slot-die coating of a high performance copolymer in a readily scalable roll process for polymer solar cells. *Advanced Energy Materials*, 3(12):1664–1669, 2013.

[128] M. Hösel, R. R. Søndergaard, M. Jørgensen, and F. C. Krebs. Fast Inline Roll-to-Roll Printing for Indium-Tin-Oxide-Free Polymer Solar Cells Using Automatic Registration. *Energy Technology*, 1(1):102–107, 2013.

[129] B. Muhsin, R. Roesch, G. Gobsch, and H. Hoppe. Flexible ITO-free polymer solar cells based on highly conductive PEDOT:PSS and a printed silver grid. *Solar Energy Materials and Solar Cells*, 130:551–554, 2014.

[130] I. Burgués-Ceballos, N. Kehagias, C. M. Sotomayor-Torres, M. Campoy-Quiles, and P. D. Lacharmoise. Embedded inkjet printed silver grids for ITO-free organic solar cells with high fill factor. *Solar Energy Materials and Solar Cells*, 127:50–57, 2014.

[131] T. M. Eggenhuisen, Y. Galagan, a. F. K. V. Biezemans, T. M. W. L. Slaats, W. P. Voorthuijzen, S. Kommeren, S. Shanmugam, J. P. Teunissen, A. Hadipour, W. J. H. Verhees, S. C. Veenstra, M. J. J. Coenen, J. Gilot, R. Andriessen, and W. a. Groen. High efficiency, fully inkjet printed organic solar cells with freedom of design. *J. Mater. Chem. A*, 3(14):7255–7262, 2015.

[132] J. Czolk, D. Landerer, M. Koppitz, D. Nass, and A. Colsmann. Highly Efficient, Mechanically Flexible, Semi-Transparent Organic Solar Cells Doctor Bladed from Non-Halogenated Solvents. *Advanced Materials Technologies*, 1(9):1600184, 2016.

[133] S. Berny, N. Blouin, A. Distler, H. J. Egelhaaf, M. Krompiec, A. Lohr, O. R. Lozman, G. E. Morse, L. Nanson, A. Pron, T. Sauermann, N. Seidler, S. Tierney, P. Tiwana, M. Wagner, and H. Wilson. Solar trees: First large-scale demonstration of fully solution coated, semitransparent, flexible organic photovoltaic modules. *Advanced Science*, 3(5):1–7, 2015.

[134] B. Knight, J. Hummelen, F. LePeq, and F. Wudl. Preparation and Characterization of Fulleroid and Methanofullerene Derivatives. *J. Org. Chem*, 60(21):532–538, 1995.

[135] N. G. Semaltianos, C. Koidis, C. Pitsalidis, P. Karagiannidis, S. Logothetidis, W. Perrie, D. Liu, S. P. Edwardson, E. Fearon, R. J. Potter, G. Dearden, and K. G. Watkins. Picosecond laser patterning of PEDOT:PSS thin films. *Synthetic Metals*, 161(5-6):431–439, 2011.

[136] A. Schoonderbeek. Laser Processing of Thin Films for Photovoltaic Applications. *Journal of Laser Micro/Nanoengineering*, 5(3):248–255, 2010.

[137] F. Guo, P. Kubis, T. Przybilla, Er. Spiecker, A. Hollmann, S. Langner, K. Forberich, and C. J. Brabec. Nanowire Interconnects for Printed Large-Area Semitransparent Organic Photovoltaic Modules. *Advanced Energy Materials*, 5(12):1401779, 2015.

[138] N. Bellini, R. Geremia, and D. Karnakis. Increasing laser pulse overlap restricts picosecond laser ablation of thin metal films near ablation threshold. *Applied Physics A: Materials Science and Processing*, 123(5):1–6, 2017.

List of Figures

List of Tables

Abbreviations

A	absorption
AFM	atomic force microscopy
AMOLED	active-matrix-driven OLED
BB	beam block
BHJ	bulk heterojunction
BS	beam splitter
CIGS	copper indium gallium selenide
η	power efficiency
η_c	current efficiency
$\mathrm{C_p}$	specific heat coefficient
CW	continous wave
E	energy level
EEL	electron extraction layer
$\mathrm{E_{HOMO,donor}}$	HOMO level of the donor
$\mathrm{E_{LUMO,acceptor}}$	LUMO level of the acceptor
$\mathrm{E_{pulse}}$	pulse energy
ETL	electron transport layer
Φ	luminous flux
F	fluence
$\mathrm{F_{th}}$	threshold fluence
FF	fill factor
FHI	fourth harmonic idler
FHS	fourth harmonic signal
G	total gain
GAD	gaseous analytical detector
GFF	geometric fill factor
HAZ	heat affected zone
HEL	hole extraction layer
HIL	hole injection layer
HOMO	highest occupied molecular orbital
HTL	hole transport layer
I	current
$\mathrm{IC_{60}BA}$	indene-$\mathrm{C_{60}}$ bisadduct

$\mathrm{I_{mpp}}$	current maximum power point
$\mathrm{I_{sc}}$	short circuit current
IM	idler mirror
ITO	indium doped tin oxide
$\mathrm{I_v}$	luminous intensity
J	current density
$\mathrm{J_{dark}}$	current density in the dark
J_{sc}	short-circuit current
L	luminance
laser	light amplification by stimulated emission of radiation
LTI	Light Technology Institute
LUMO	lowest unoccupied orbital
LVD	low vacuum detector
MASER	microwave amplification by stimulated emission of radiation
MPP	maximum power point
MZE	Material Research Center for Energy Systems
N	number of pulses
$\mathrm{N_1}$	number of entities level 1
NA	numerical aperture
NC	non linear crystal
OCS	OLED characterization system
OLED	organic light emitting diode
OPV	organic photovoltaic devices
$\mathrm{P_{in}}$	power incident light
P1	structuring step bottom electrode
P2	structuring step active layer
P3	structuring step top electrode
P3HT	poly-3-hexylthiophene
PC	pockels cell
$\mathrm{PC_{71}BM}$	[6,6]-phenyl $\mathrm{C_{71}}$-butyric acid methyl ester
$\mathrm{PC_{60}BM}$	[6,6] phenyl-$\mathrm{C_{61}}$ butyric acid methyl ester
PCDTBT	poly[*N*-9'-heptadecanyl-2,7-carbazole-alt-5,5-(4',7'-di-2-thienyl-2',1',3'-benzothiadiazole)]
PCE	power conversion efficiency
PEDOT:PSS	poly(3,4-ethylenedioxythiophene):polystyrene sulfonate
PEI	polyethylenimine
PET	Polyethylene terephthalate
PTB7	poly[[4,8-di(5-ethylhexyloxy)benzo[1,2-b;4,5-b]dithiophene][3-fluoro-2[(2-ethylhexyl)carbonyl]thieno[3,4-b]thiophenediyl]]
QWP	quarter wave plate

R	Reflection
R_P	parallel resistance
R_S	serial resistance
SAM	self assembled monolayer
SCL	space charge limited current
SDG	synchronization and delay generator
SEM	scanning electron microscope
SFI	sum frequency idler
SFS	sum frequency signal
SHI	second harmonic idler
SHS	second harmonic signal
SMU	source measurement unit
T	transmission
$\mathrm{T_e}$	temperature electron
$\mathrm{T_l}$	temperature lattice
$\mathrm{t_p}$	pulse duration
TSC	tandem solar cell
V	voltage
$\mathrm{V_{mp}}$	maximum power point voltage
$\mathrm{V_{oc}}$	open-circuit voltage
$\mathrm{V_{on}}$	onset voltage
Ω	frequency
W	population change rate
WLG	white-light continuum generator

Acknowledgements

The time during my PhD was a fulfilling one where I learn many different things. Here I had the opportunity to work with many people who all help me a little to get here.
Zuerst möchte ich mich bei meinem Betreuer Priv.-Doz. Dr. Alexander Colsmann bedanken. Vielen Dank für deine Geduld und deine Zeit. Mein erster richtiger Kontakt mit der Wissenschaft war meine Masterarbeit. Danach hast du mir die Gelegenheit gegeben, meine Promotion zu machen. I would also like to thank my co - referent Prof. Thomas Heiser. Thanks again for taking the time of going through my work. Ich möchte mich auch bei den Leuten vom LTI bedanken. Bei Prof. Uli Lemmer für die netten Diskussionen und den Spaß beim Joggen. Bei Frau Henne und Frau Holeisen, ihr habt immer Geduld mit meinem Deutsch gehabt und habt mir immer geholfen. Bei Herrn Geiselhöringer, für die Hilfe mit der elektrischen Anlage und bei Herrn Sütsch, für seine Hilfe beim Ausbau des Laserlabors. Bei Christian Kayser möchte ich mich für alle Einweisungen bedanken. Vielen Dank an die OPV Gruppe, ohne euch konnte ich diese Arbeit nicht machen. Es ist/war eine Ehre mit euch zu arbeiten.

- Dr. Glaser, vielen Dank für all die langen Stunden und dein Vertrauen. Wir haben viele Experimente zusammen gemacht.
- Min Zhang, danke für die Unterstützung und deine Hilfe mit dem OLED Thema.
- Dr. Schneider, ich möchte mich auch für deine Unterstützung bedanken.
- Dr. Höfle, danke für den Rat und die Hilfe bei dem OLED Thema.
- Christian Sprau, danke für die Geduld mit dem Projektbericht und deinen wissenschaftlichen Rat.
- Dr. Gartner, danke für die Nanopartikel und die Hilfe bei verschiedenen Themen.
- Dominik Landerer, vielen Dank für dein positive Art und die Hilfe mit den semitransparenten Experimenten.
- Manuel Koppitz, danke für deine Geduld, der Laser war manchmal kaputt. Ich möchte mich bei dir auch für die opaken Experimente bedanken.
- Martin Hochberg, danke für die AFM Einweisung.
- Dr. Bahro, danke für deine Hilfe mit dem Laser.

- Dr. Mertens, du machst Dinge lustig.
- Dr. Nickel, danke für meine erste Einweisung mit dem Laser.
- Tobias Leonhard, danke für deine Hilfe mit dem AFM.

Allen anderen, Lorenz Graf von Reventlow, Felix Manger, Philip Meier, danke für die nette Arbeitsatmosphäre.
Natürlich möchte ich mich auch bei meinen Studenten bedanken. Julian Dlugosch, Pascal Bohler, Torsten Friederich, Tim Wünnemann, Florian Haberstroh und Malte Martens. Vielen Dank für eure Geduld, ich habe viel von euch gelernt.
Ich möchte auch Dr. Susanne Wagner für ihre Hilfe mit dem SEM danken.
Danke den Leuten von Coherent, Stefan Arnold, Marcus Freese und Thomas Harms. Ich habe viel über unseren Laser von euch gelernt. Den Leuten von Newport, Bill Clench, Dr. Zimmer und John Carter, vielen Dank für die Hilfe mit der Workstation.
Ich möchte mich auch bei den Leuten vom Boxing bedanken. Ertunc, Malik und Ayte Dankeschön, man soll immer 100% geben :D.
I also want to thank the people that helped correcting my thesis. Julian Dlugosch, Min Zhang, Konstantin Glaser, Dominik Landerer, Manuel Koppitz, Mahsa Bagheri, Ricardo Lascurain and Omar Alvarez, sorry for bothering you with this and thanks for your help.

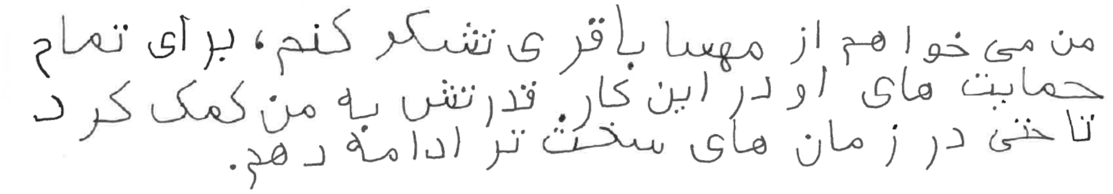

من می خواهم از مهسا باقری تشکر کنم، برای تمام
حمایت های او در این کار. قدرتش به من کمک کرد
تا حتی در زمان های سخت تر ادامه دهم.

Chciałbym serdecznie podziękować Joannie Kot. Joanna zawsze mnie wspierała i pomagała mi pozostać przy zmysłach gdy praca mnie przygniatała.
También quiero agradecer a mis amigos en México, que nunca dejaron de apoyarme y siempre estuvieron al pendiente de cómo iba todo acá en Alemania, gracias Oldpaleros.
Finalmente, gracias a mi familia, gracias a mis papas, quienes han hecho muchisimo por mi. A mis primos, Jose Luis, Beatriz y Amairani por acompañarme a la distancia y hacerme reir muchas veces mientras estaba aca en Alemania. Gracias tambien a mis tias y especialmente a mi abuela.
A todos ustedes gracias totales. To all of you thank you.